

# Nucleon Polarizabilities: from Compton Scattering to Hydrogen Atom

Franziska Hagelstein<sup>a</sup>, Rory Miskimen<sup>b</sup>, Vladimir Pascalutsa<sup>a</sup>

<sup>a</sup> *Institut für Kernphysik and PRISMA Excellence Cluster, Johannes Gutenberg-Universität Mainz, D-55128 Mainz, Germany*

<sup>b</sup> *Department of Physics, University of Massachusetts, Amherst, 01003 MA, USA*

---

## Abstract

We review the current state of knowledge of the nucleon polarizabilities and of their role in nucleon Compton scattering and in hydrogen spectrum. We discuss the basic concepts, the recent lattice QCD calculations and advances in chiral effective-field theory. On the experimental side, we review the ongoing programs aimed to measure the nucleon (scalar and spin) polarizabilities via the Compton scattering processes, with real and virtual photons. A great part of the review is devoted to the general constraints based on unitarity, causality, discrete and continuous symmetries, which result in model-independent relations involving nucleon polarizabilities. We (re-)derive a variety of such relations and discuss their empirical value. The proton polarizability effects are presently the major sources of uncertainty in the assessment of the muonic hydrogen Lamb shift and hyperfine structure. Recent calculations of these effects are reviewed here in the context of the “proton-radius puzzle”. We conclude with summary plots of the recent results and prospects for the near-future work.

**Keywords:** Proton, Neutron, Dispersion, Compton scattering, Structure functions, Muonic hydrogen, Chiral EFT, Lattice QCD

---

## Contents

<b>1</b>	<b>Introduction</b>	<b>3</b>
1.1	Notations and Conventions	3
<b>2</b>	<b>Basic Concepts and Ab Initio Calculations</b>	<b>6</b>
2.1	Naïve Picture	6
2.2	Defining Hamiltonian	7
2.3	Lattice QCD	7
2.4	Chiral EFT	9
<b>3</b>	<b>Polarizabilities in Compton Scattering</b>	<b>12</b>
3.1	Compton Processes	12
3.2	Helicity Amplitudes	13
3.3	Multipole Expansion	14
3.4	Tensor Decompositions	16
3.5	Unitarity Relations	17
3.5.1	Optical Theorem	17
3.5.2	Watson’s Theorem Extended	17
3.6	Expansion in Static vs. Dynamic Polarizabilities	19
3.7	Polarized Observables	19
<b>4</b>	<b>Compton Scattering Experiments</b>	<b>21</b>
4.1	Low-Energy Expansion of CS Observables	21
4.2	Determination of Scalar Polarizabilities	23
4.2.1	Proton	23
4.2.2	Neutron	24
4.3	Determination of Proton Spin Polarizabilities	25

4.3.1	Linearly Polarized Photons . . . . .	27
4.3.2	Circularly Polarized Photons and Transversely Polarized Target . . . . .	28
4.3.3	Circularly Polarized Photons and Longitudinally Polarized Target . . . . .	31
4.4	Virtual Compton Scattering . . . . .	31
4.4.1	Response Functions and Generalized Polarizabilities . . . . .	32
4.4.2	Radial Distribution of the Electric Dipole Polarizability . . . . .	34
4.5	Timelike Compton Scattering . . . . .	35
<b>5</b>	<b>Sum Rules</b>	<b>36</b>
5.1	Forward Doubly-Virtual Compton Scattering Amplitude . . . . .	36
5.2	Unitarity and Relation to Structure Functions . . . . .	37
5.3	Analyticity and Dispersion Relations . . . . .	38
5.4	Sum Rules for Real Photons . . . . .	40
5.5	Relations at Finite $Q$ . . . . .	41
5.5.1	Spin-Independent Relations . . . . .	41
5.5.2	Spin-Dependent Relations . . . . .	43
5.6	Empirical Evaluations of Sum Rules . . . . .	44
<b>6</b>	<b>Proton Structure in (Muonic) Hydrogen</b>	<b>48</b>
6.1	Charge and Zemach Radii from Muonic Hydrogen . . . . .	49
6.2	Finite-Size Effects by Dispersive Technique . . . . .	50
6.2.1	Lamb Shift . . . . .	51
6.2.2	Consistency of the Charge Radius Extraction . . . . .	52
6.2.3	Hyperfine Splitting . . . . .	53
6.3	Structure Effects through Two-Photon Exchange . . . . .	54
6.4	Empirical Evaluations . . . . .	55
6.4.1	Lamb Shift . . . . .	55
6.4.2	Hyperfine Splitting . . . . .	56
6.5	Chiral EFT Evaluations . . . . .	58
6.5.1	Lamb Shift . . . . .	58
6.5.2	Hyperfine Splitting . . . . .	59
<b>7</b>	<b>Summary Plots and Conclusions</b>	<b>62</b>
7.1	Scalar Polarizabilities . . . . .	62
7.2	Spin Polarizabilities . . . . .	64
7.3	Status of the Proton-Radius Puzzle . . . . .	66
7.4	Proton Structure in Muonic Hydrogen . . . . .	66
	<b>Acknowledgements</b>	<b>68</b>
<b>Appendix A</b>	<b>Born Contribution in RCS and VVCS amplitudes</b>	<b>69</b>
<b>Appendix B</b>	<b>Derivation of a Dispersion Relation</b>	<b>69</b>
<b>Appendix C</b>	<b>Collection/Index of Formulae</b>	<b>71</b>

## 1. Introduction

The concept of *polarizabilities*, common in optics and classical electrodynamics, was extended to the nucleon in the 1950s [1, 2], together with the first observations of Compton scattering (CS) on the proton [3–8]. Since then, the CS process, with real (RCS) or virtual (VCS) photons, became the main experimental tool in studying the nucleon polarizabilities, with dedicated experiments completed at: Lebedev Institute (Moscow) [8, 9], MUSL (Illinois) [10], SAL (Saskatoon) [11, 12], LEGS (Brookhaven) [13], Bates (MIT) [14], MaxLab (Lund) [15], MAMI (Mainz) [16–22], and Jefferson Laboratory (Virginia) [23].

In recent years, the nucleon polarizabilities have advanced to the avantgarde of hadron physics. They are a major source of uncertainty in the muonic-hydrogen determination of the proton charge radius [24] and Zemach radius [25], and hence are a prominent part of the “proton-radius puzzle” [26]. They play an important role in the controversy of the electromagnetic (e.m.) contribution to the proton-neutron mass difference [27–29]. Several issues involving the nucleon polarizabilities have emerged from the ongoing ‘spin physics program’ at the Jefferson Laboratory (JLab), which is mapping out the spin structure functions of the nucleon [30–32]. The various moments of these structure functions are related to the forward *spin polarizabilities*, with one of them,  $\delta_{LT}$ , being notoriously difficult to understand within the chiral effective-field theory ( $\chi$ EFT) [33, 34]. The currently operating photon beam facility MAMI has established a dedicated experimental program to disentangle the nucleon polarizabilities through the low-energy RCS with polarized beams [35, 36] and targets [37, 38]; a complementary program, at even lower energy, is planned at HI $\gamma$ S (Duke) [39, 40]. A new experimental program is being developed for the upcoming high-intensity electron beam facility MESA (Mainz). The recent theory advances include: (partially) unquenched lattice QCD calculations [41–47]; novel  $\chi$ EFT calculations of CS [48–54] and of the polarizability effects in hydrogenic atoms [55, 56]; development and evaluation of model-independent relations involving the nucleon polarizabilities [57–60]. These are the topics of this review.<sup>1</sup>

The paper is organized as follows. Sect. 2 outlines the basic concepts as well as discusses the current efforts to calculate the nucleon polarizabilities from first principles: lattice QCD (Sect. 2.3) and  $\chi$ EFT (Sect. 2.4). Sect. 3 describes the way polarizabilities appear in the CS processes, while Sect. 4 discusses the way they are extracted from the CS experiments. Sect. 5 is devoted to dispersive sum rules, i.e., a variety of model-independent relations derived from general properties of the forward doubly-virtual CS amplitude. They involve the wealth of inelastic electron-scattering data into the polarizability studies, and their data-driven evaluations are discussed in Sect. 5.6. In Sect. 6 we present an overview of nucleon structure contributions to the hydrogen Lamb shift and hyperfine structure. The reviewed results for nucleon polarizabilities and their effect in muonic hydrogen are collected in the summary plots in Sect. 7. The reader interested in only a brief survey of the field may skip to that section. Finally, the Appendices contain the expressions for the Born contribution to CS amplitudes (Appendix A), a derivation of generic dispersion relations (Appendix B), and a collection of the most important formulae (Appendix C).

The remainder of this section contains the notations and conventions used throughout the paper.

### 1.1. Notations and Conventions

- We use the natural units,  $\hbar = c = 1$ , and the following notation for the well-established parameters, along with their Particle Data Group (PDG) values [71]:

$\alpha$  the fine-structure constant,  $\alpha = 1/137.035999074(44)$ .

$\hbar c$  conversion constant,  $\hbar c = 197.3269718(44)$  MeV fm.

$m$  lepton mass,  $(m_e, m_\mu) \simeq (0.5109990, 105.65837)$  MeV.

$m_\pi$  pion mass,  $(m_{\pi^0}, m_{\pi^\pm}) \simeq (134.977, 139.570)$  MeV.

---

<sup>1</sup>For other recent reviews (more focused on a subset) of these topics see: Drechsel et al. [61] (sum rules and fixed- $t$  dispersion relations for CS), Schumacher [62] (RCS experiments), Kuhn et al. [63] (spin structure functions and sum rules), Phillips [64] (few-nucleon  $\chi$ EFT, nucleon polarizabilities), Griesshammer et al. [65] ( $\chi$ EFT and RCS experiments), Guichon and Vanderhaeghen [66] (VCS and generalized polarizabilities), Holstein and Scherer [67] (pion, kaon, nucleon polarizabilities), Pohl et al. [68], Carlson [69], Karshenboim et al. [70] (proton-radius puzzle).

$M$  nucleon mass,  $(M_p, M_n) \simeq (938.272, 939.565)$  MeV.

$\kappa$  nucleon anomalous magnetic moment,  $(\kappa_p, \kappa_n) \simeq (1.7929, -1.9130)$ .

$f_\pi$  pion decay constant,  $f_\pi = 92.21(14)$  MeV.

$g_A$  nucleon axial charge,  $g_A = 1.2723(23)$ .

• Other frequently used notation:

$s, t, u$  Mandelstam variables.

$\nu, \omega_B, \omega$  photon energy in the lab, Breit, and center-of-mass reference frames.

$\vartheta, \theta_B, \theta$  scattering angle in the lab, Breit, and center-of-mass reference frames.

$d\Omega_L, d\Omega_{cm}$  element of the solid angle in the lab and center-of-mass reference frames.

$Q^2 = -q^2$  momentum transfer, photon virtuality.

$\tau = Q^2/4M^2$  dimensionless momentum-transfer variable.

$x = Q^2/2M\nu$  Bjorken variable.

$F_1(Q^2), F_2(Q^2)$  Dirac and Pauli form factors.

$G_E(Q^2), G_M(Q^2)$  electric and magnetic Sachs form factors.  $G_E = F_1 - \tau F_2, G_M = F_1 + F_2$ .

$f_{1,2}(x, Q^2)$  unpolarized structure functions.

$g_{1,2}(x, Q^2)$  polarized (or spin) structure functions.

$\lambda_\gamma, \lambda'_\gamma$  helicities of the incident and scattered photon.

$\lambda_N, \lambda'_N$  helicities of the incident and scattered nucleon.

$\sigma(\nu), d\sigma/d\Omega$  unpolarized total and differential cross sections.

$\sigma_T, \sigma_L$  unpolarized absorption cross section of the transverse ( $T$ ) or longitudinal ( $L$ ) photon.

$\sigma_{TT}, \sigma_{LT}$  doubly-polarized photoabsorption cross sections [see below Eq. (5.6)].

$Ze, \kappa$  charge and anomalous magnetic moment of the nucleon ( $Z = 1$  for proton,  $Z = 0$  for neutron).

$Ze, \kappa$  charge and anomalous magnetic moment of the nucleus (for hydrogen:  $Z = 1, \kappa = \kappa_p$ ).

$\mu$  magnetic moment of the nucleon or nucleus,  $\mu = Z + \kappa = Z(1 + \kappa)$ , in units of nuclear magneton.

$a, m_r$  Bohr radius and reduced mass,  $a^{-1} = Z\alpha m_r, m_r = mM/(m + M)$ .

• Salient conventions:

□ Metric:  $g_{\mu\nu} = \text{diag}(+1, -1, -1, -1)$ . Levi-Civita symbol:  $\epsilon_{0123} = +1 = -\epsilon^{0123}$ .

□ Scalar products:  $\mathbf{p} \cdot \mathbf{q} = p_i q_i, p \cdot q = p_0 q_0 - \mathbf{p} \cdot \mathbf{q}, p \cdot T \cdot q = p_\mu T^{\mu\nu} q_\nu, \not{p} = p \cdot \gamma$ .

□ Pauli and Dirac matrices:

$$1_2 = \begin{pmatrix} 1 & 0 \\ 0 & 1 \end{pmatrix}, \sigma^1 = \begin{pmatrix} 0 & 1 \\ 1 & 0 \end{pmatrix}, \sigma^2 = \begin{pmatrix} 0 & -i \\ i & 0 \end{pmatrix}, \sigma^3 = \begin{pmatrix} 1 & 0 \\ 0 & -1 \end{pmatrix},$$

$$\gamma^0 = \begin{pmatrix} 1_2 & 0 \\ 0 & -1_2 \end{pmatrix}, \gamma^i = \begin{pmatrix} 0 & \sigma^i \\ -\sigma^i & 0 \end{pmatrix}, \gamma^5 = i\gamma^0\gamma^1\gamma^2\gamma^3 = \begin{pmatrix} 0 & 1_2 \\ 1_2 & 0 \end{pmatrix}, \quad (1.1)$$

$$\gamma_{\mu\nu} = \frac{1}{2} [\gamma_\mu, \gamma_\nu] = -i/2 \epsilon_{\mu\nu\alpha\beta} \gamma^\alpha \gamma^\beta \gamma^5, \gamma_{\mu\nu\alpha} = \frac{1}{2} (\gamma_\mu \gamma_\nu \gamma_\alpha - \gamma_\alpha \gamma_\nu \gamma_\mu) = -i \epsilon_{\mu\nu\alpha\beta} \gamma^\beta \gamma^5,$$

$$\gamma_{\mu\nu\alpha\beta} = \frac{1}{2} [\gamma_{\mu\nu\alpha}, \gamma_\beta] = i \epsilon_{\mu\nu\alpha\beta} \gamma^5, \quad (1.2)$$

satisfying:  $\frac{1}{2} [\sigma_i, \sigma_j] = i \epsilon_{ijk} \sigma_k, \{\gamma_\mu, \gamma_\nu\} = 2g_{\mu\nu}, \{\gamma_\mu, \gamma^5\} = 0$ .

□ Helicity spinors:

$$u_\lambda(\mathbf{p}) = \begin{pmatrix} \sqrt{E_p + M} \\ 2\lambda\sqrt{E_p - M} \end{pmatrix} \otimes \chi_\lambda(\theta, \varphi), \quad (1.3)$$

with  $E_p = \sqrt{M^2 + \mathbf{p}^2}$ ;  $\lambda = \pm 1/2$  the helicity (i.e., the spin projection onto  $\mathbf{p}$ );  $\theta, \varphi$  the spherical coordinates of  $\mathbf{p}$ ; and the two-component Pauli spinors:

$$\chi_{1/2}(\theta, \varphi) = \begin{pmatrix} \cos(\theta/2) \\ e^{i\varphi} \sin(\theta/2) \end{pmatrix}, \quad \chi_{-1/2}(\theta, \varphi) = \begin{pmatrix} -e^{-i\varphi} \sin(\theta/2) \\ \cos(\theta/2) \end{pmatrix}. \quad (1.4)$$

The helicity spinors satisfy the following relations, for  $p = (E_p, \mathbf{p})$ :

$$\bar{u}_{\lambda'}(\mathbf{p}) u_\lambda(\mathbf{p}) = 2M\delta_{\lambda'\lambda}, \quad \sum_\lambda u_\lambda(\mathbf{p}) \bar{u}_\lambda(\mathbf{p}) = \not{p} + M, \quad (\not{p} - M)u_\lambda(\mathbf{p}) = 0. \quad (1.5)$$

□ Photon polarization vector,  $\varepsilon_{\lambda_\gamma}(q)$ , for a photon with four-momentum  $q$  and helicity  $\lambda_\gamma = -1, 0, 1$ .

a) for real photon moving along the  $z$ -axis,  $q = (\nu, 0, 0, \nu)$ , there are only transverse polarizations,

$$\text{i) circularly polarized photons: } \varepsilon_{\pm 1}^\mu = \frac{1}{\sqrt{2}}(0, \mp 1, -i, 0), \quad (1.6a)$$

$$\text{ii) linearly polarized photons: } \varepsilon^\mu(\phi) = (0, \cos \phi, \sin \phi, 0), \quad (1.6b)$$

b) for virtual photon moving along the  $z$ -axis,  $q = (\nu, 0, 0, |\mathbf{q}|)$ , there is, in addition, the longitudinal polarization:

$$\varepsilon_0^\mu = \frac{1}{\sqrt{q^2}}(|\mathbf{q}|, 0, 0, \nu), \quad \text{with } |\mathbf{q}| = \sqrt{\nu^2 - q^2}. \quad (1.7)$$

The transversality, orthonormality and completeness conditions are:

$$q \cdot \varepsilon_{\lambda_\gamma}(q) = 0, \quad \varepsilon_{\lambda'_\gamma}^*(q) \cdot \varepsilon_{\lambda_\gamma}(q) = -\delta_{\lambda'_\gamma \lambda_\gamma}, \quad \sum_{\lambda_\gamma = \pm 1, 0} \varepsilon_{\lambda_\gamma}^{*\mu} \varepsilon_{\lambda_\gamma}^\nu = -g^{\mu\nu} + \frac{q^\mu q^\nu}{q^2}. \quad (1.8)$$

Note that for a spacelike photon ( $q^2 = -Q^2 < 0$ ), the longitudinal polarization vector is antihermitian,  $\varepsilon_0^* = -\varepsilon_0$ , and as the result the above orthonormality and completeness conditions are not satisfied. This is why one often defines the longitudinal polarization vector for a spacelike photon as  $\varepsilon'_0 \equiv i\varepsilon_0 = 1/Q(|\mathbf{q}|, 0, 0, \nu)$ .

## 2. Basic Concepts and Ab Initio Calculations

### 2.1. Naïve Picture

A polarizability, by definition, quantifies the response of a system to an external electromagnetic (e.m.) field, or more precisely, the e.m. moments induced in response to a moderate e.m. field. An evident picture is provided by an atom immersed in a homogeneous electric field. The atomic nucleus and the electron cloud displace in opposite directions, thus creating an electric dipole moment proportional to the field strength, with the proportionality coefficient  $\alpha_{E1}$ , the electric dipole polarizability. The polarizability mechanism in the nucleon is less obvious, but, very roughly, one can replace the electron cloud by the “pion cloud” and the nucleus by a “quark core” to have a similar picture, see Fig. 2.1. An analogous representation of the magnetic polarizability,  $\beta_{M1}$ , is displayed in Fig. 2.2.

This naïve interpretation is realized, in a way, in  $\chi$ EFT where the (renormalized) pion loops can be thought of as the effect of the pion cloud, while the  $\Delta(1232)$ -resonance excitation and the low-energy constants (LECs) are the effect of the quark core. In the case of the magnetic dipole polarizability  $\beta_{M1}$ , the *diamagnetic* contribution of the pion cloud is competing against the *paramagnetic* contribution of the quark-core excitation, see Fig. 2.2. The two contributions are largely canceling each other, leaving the nucleon with a relatively small magnetic polarizability, cf. Sect. 2.4 for details.

Other intuitive pictures of the nucleon polarizabilities emerge in quark models [72–76], the Skyrme model [77–82], and the Nambu-Jona-Lasinio model [83]. All of them point out the large paramagnetic contribution due to the nucleon-to- $\Delta(1232)$   $M1$  transition.

While for the atoms the polarizabilities are of order of the atomic volume, the nucleon being much tighter bound (nearly 99% of its mass coming from the binding force) has polarizabilities which are about three orders of magnitude smaller than its volume. It is customary to use the units of  $10^{-4} \text{ fm}^3$  for the dipole polarizabilities of the nucleon.

The critical electric field strength needed to induce any appreciable polarizability of the nucleon can be estimated as the ratio of the average energy level spacing in the nucleon to the size of the nucleon, i.e.,  $E_{\text{crit.}} \approx 100 \text{ MeV}/(e \text{ fm}) = 10^{23} \text{ Volt/m}$ . Static electric field strengths of this intensity are not available in a laboratory, and will never be available. However, a classical estimate of the electric field strength of a 100 MeV photon Compton scattering from the nucleon is approximately  $10^{23} \text{ Volt/m}$ . Given the absence of static e.m. fields of the required immensity, the CS process is currently the best available tool for accessing the nucleon polarizabilities experimentally, cf. Sect. 4.

In the rest of this section we introduce the nucleon polarizabilities and discuss their calculation from first principles. We shall focus on describing the efforts to compute the nucleon polarizabilities in lattice QCD and chiral EFT. In the latter case, calculations of the CS observables will be discussed too.

It is worthwhile noting that is a number of sophisticated theoretical approaches, other than lattice QCD and chiral EFT, applied to the nucleon polarizabilities and low-energy CS. They include: the fixed- $t$  dispersion

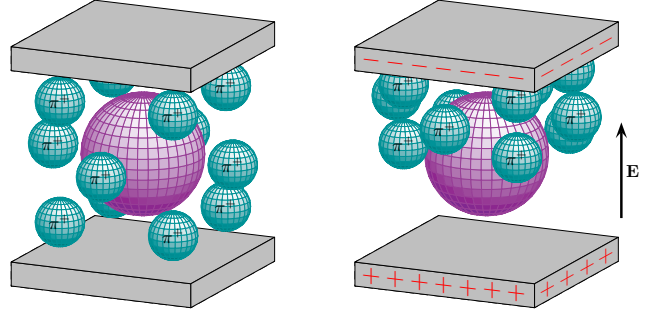


Figure 2.1: Naive view of the proton, consisting of a pion cloud and a quark core, placed between the plates of a parallel plate capacitor. The left (right) figure shows the capacitor discharged (charged). Plot courtesy of Phil Martel.

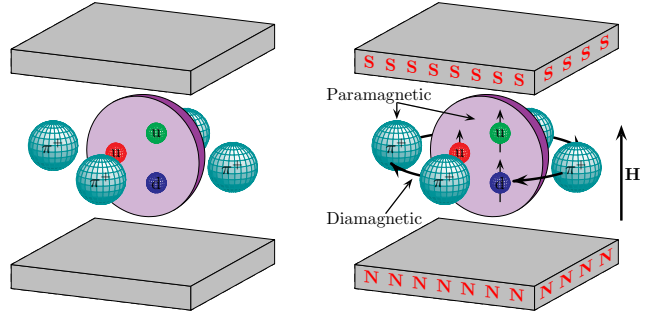


Figure 2.2: Naive view of the proton, consisting of a pion cloud and a quark core, placed between the poles of a magnet. The left (right) figure shows the external magnetic field turned off (on). Plot courtesy of Phil Martel.

relations [84–87], effective-Lagrangian models with [88–91] and without [92–94] causality constraints, the Dyson–Schwinger equation approach to QCD [95]. The first one in this list is very popular in the extractions of polarizabilities from CS data, and will be mentioned frequently in other chapters of this review.

## 2.2. Defining Hamiltonian

The response in the energy of the system due to polarizability effects is described by an effective Hamiltonian, which usually is ordered according to the number of spacetime derivatives of the e.m. field  $A_\mu(x)$  [96, 97],

$$\mathcal{H}_{\text{eff}}^{(2)} = -4\pi \left( \frac{1}{2} \alpha_{E1} \mathbf{E}^2 + \frac{1}{2} \beta_{M1} \mathbf{H}^2 \right), \quad (2.1a)$$

$$\mathcal{H}_{\text{eff}}^{(3)} = -4\pi \left( \frac{1}{2} \gamma_{E1E1} \boldsymbol{\sigma} \cdot (\mathbf{E} \times \dot{\mathbf{E}}) + \frac{1}{2} \gamma_{M1M1} \boldsymbol{\sigma} \cdot (\mathbf{H} \times \dot{\mathbf{H}}) - \gamma_{M1E2} E_{ij} \sigma_i H_j + \gamma_{E1M2} H_{ij} \sigma_i E_j \right), \quad (2.1b)$$

$$\mathcal{H}_{\text{eff}}^{(4)} = -4\pi \left( \frac{1}{2} \alpha_{E1\nu} \dot{\mathbf{E}}^2 + \frac{1}{2} \beta_{M1\nu} \dot{\mathbf{H}}^2 \right) - 4\pi \left( \frac{1}{12} \alpha_{E2} E_{ij}^2 + \frac{1}{12} \beta_{M2} H_{ij}^2 \right), \quad (2.1c)$$

where the electric ( $\mathbf{E}$ ) and magnetic ( $\mathbf{H}$ ) fields are expressed in terms of the e.m. field tensor,  $F_{\mu\nu} = \partial_\mu A_\nu - \partial_\nu A_\mu$ , as:  $E_i = F_{0i}$ ,  $H_i = \epsilon_{ijk} F_{jk}$ . Furthermore, the following shorthand notation is used:

$$E_{ij} = \frac{1}{2}(\nabla_i E_j + \nabla_j E_i), \quad H_{ij} = \frac{1}{2}(\nabla_i H_j + \nabla_j H_i). \quad (2.2)$$

The 3<sup>rd</sup>-order term is dependent on the nucleon spin  $\boldsymbol{\sigma}$ , and the corresponding polarizabilities are called the *spin polarizabilities* [98]. They have no analog in classical electrodynamics, but evidently they describe the coupling of the induced e.m. moments with the nucleon spin. Unlike the scalar polarizabilities, they are not invoked by static e.m. fields.

The above Hamiltonian is quadratic in the e.m. field. This means that the polarizabilities can directly be probed in the CS process. The expansion in derivatives of the e.m. field translates then into the low-energy expansion. The polarizabilities thus appear as coefficients in the low-energy expansion of the CS amplitudes, cf. Sect. 3.

As noted above, the scalar dipole polarizabilities are measured in units of  $10^{-4} \text{ fm}^3$ . In general, the nucleon polarizabilities are measured in units  $10^{-4} \text{ fm}^{n+1}$ , where  $n$  is the order at which they appear.

## 2.3. Lattice QCD

Presently all of the lattice QCD calculations of nucleon polarizabilities use the background-field method [99, 100], which amounts to measuring the shift in the mass spectrum upon applying a classical background field. On a given configuration, one multiplies the SU(3) gauge fields by a U(1) gauge field. The U(1) links are given by

$$U_\mu(x) = \exp [ie_q a A_\mu(x)], \quad (2.3)$$

where  $e_q$  is the quark charge and  $a$  is the lattice spacing.

The case of a constant magnetic field is the simplest to illustrate. For the field with a magnitude  $H$  pointing in the  $+z$ -direction, the usual choice is  $A_\mu(x, y, z, t) = a H x \delta_{\mu y}$ . The problem with this choice is that due to the condition that the gauge links  $U_\mu$  must be periodic, the field is continuous only if  $e_q a^2 H = 2\pi n/L$ , with integer  $n$ . The minimal value of  $H$  is thus severely limited by the size of the lattice, although an improvement to  $H \sim 1/L^2$  behavior is easily achieved (see, e.g., Ref. [101]).

One can calculate a baryon two-point function which behaves for large time in the usual manner

$$C(t) \sim e^{-M(H)t} + \dots, \quad (2.4)$$

but with the exponential damping governed by a field-dependent mass [102]

$$M(H) = M_0 - \mu_z H - \frac{1}{2} \beta_{M1} H^2 + O(H^3), \quad (2.5)$$

where  $M_0$  is the mass with no field and  $\mu_z$  is the projection of the magnetic moment. One may cancel the odd terms by considering  $M(H) + M(-H)$  and fit the remaining  $H$ -dependence by adjusting the value of the magnetic polarizability.



Implementation of the electric field is somewhat more tricky and has led to an overall sign mistake in the value of the electric polarizability (which affects, e.g., Ref. [41] as well as many of the earlier calculations). In the proton case, one in addition needs to take care of the Landau levels, which thus far has only been done by the NPLQCD collaboration [47]. Implementation of the varying fields needed to compute the spin polarizabilities is considered in Ref. [103].

In the background field method one obviously assumes that the Taylor expansion in the field strength is quickly convergent. The non-analyticity due to the pion production induced by the background field may however become a problem. This problem is similar to the one encountered in experiment, where to see the signal in the CS observables one needs energies approaching the pion-production threshold.

Another difficulty of this method is the inclusion of the background-field effect on the “sea”. Most of the calculations to date assume the sea quarks to be neutral. Studies of the charged sea-quark contributions have been done in, e.g., Refs. [41, 104].

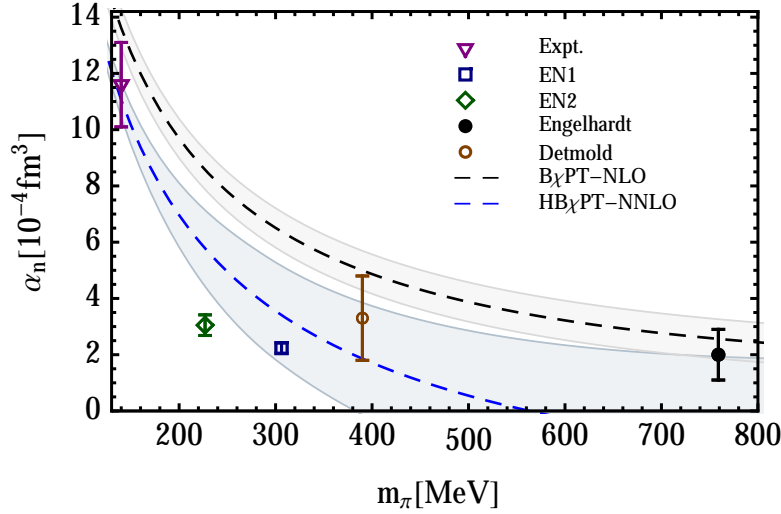


Figure 2.3: Lattice QCD results for the electric polarizability of the neutron, at unphysical values of pion mass: Engelhardt [41], Detmold et al. [42, 43], and Lujan et al. [46] on two different ensembles (‘EN1’ and ‘EN2’). The curves with error band are the predictions of the baryon and heavy-baryon  $\chi$ PT. The HB $\chi$ PT result is a fit at the physical pion mass. Plot courtesy of Andrei Alexandru.

Despite these concerns, the recent lattice results are very encouraging. Most of the results are obtained for the neutron electric polarizability, see Fig. 2.3. The lightest-pion results, indicated as EN1 and EN2 therein, are from the GWU group [46]. They have recently received substantial finite-volume corrections, moving them upwards, right onto the HB $\chi$ PT curve [105].

For the magnetic polarizability we refer to the recent work of the Adelaide CSSM group [44, 45] which used the PACS-CS 2 + 1 flavor gauge field configurations [106] and performed an extrapolation to the physical pion mass and infinite volume, see Fig. 2.4. Their extrapolated result is [45]:  $\beta_{M1}^{(n)} = 1.93(11)_{\text{stat}}(11)_{\text{sys}} \times 10^{-4} \text{ fm}^3$ , and can be directly compared with experiment and other theoretical results in Fig. 7.2. Very recently, the NPLQCD Collaboration obtained results for the electric and magnetic polarizabilities of both proton and neutron (and a

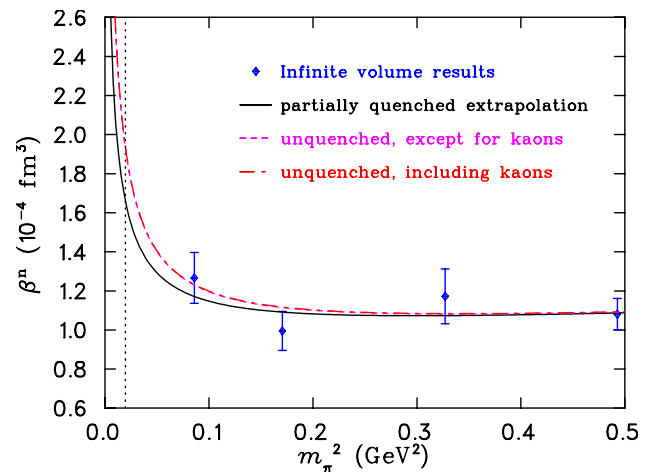


Figure 2.4: Results of Hall et al. [45] for the magnetic polarizability of the neutron. Plot courtesy of Jonathan Hall.



number of light nuclei), albeit at a relatively large pion mass of 800 MeV [47].

As an alternative to the background-field method, one may consider a four-point function calculation of the Compton tensor for spacelike photons. At present this has only been done for the light-light system (light-by-light scattering) [107]. This method would avoid the problem with the non-analytic behavior of the mass spectrum in the background field, but would require an extrapolation to the real-photon point. On the other hand, it would be a direct calculation of the polarizabilities at a finite photon virtuality  $Q^2$ , which experimentally is accessed through the dispersive sum rules (cf. Sect. 5), and is required in the atomic and two-photon-exchange calculations (cf. Sect. 6). In practice, such a direct calculation of doubly-virtual CS on the nucleon would be very challenging due to the usual problems of the noise-to-signal ratio and excited-state contamination. The CS on the pion would certainly be a better place to start.

#### 2.4. Chiral EFT

The chiral effective-field theory ( $\chi$ EFT), also referred to as the chiral perturbation theory ( $\chi$ PT) is a low-energy EFT of QCD, see Refs. [108–110] for the seminal papers. It is a quantum field theory with the Lagrangian written in terms of hadronic fields, in contrast to QCD which is written in terms of quark and gluon fields. The  $\chi$ EFT, however, holds the promise to match the QCD description of the low-energy phenomena, where by low-energy one assumes the relative energy in the hadronic system to be well below 1 GeV. In our case of CS processes, this means that the energy  $\nu$  and the momentum transfer  $Q$  with which the photon probes the nucleon are much smaller than 1 GeV. At these energies the pion interactions are suppressed. More precisely, the interaction goes with pion 4-momenta, which are relatively small for small pion energy. A perturbative expansion of scattering amplitudes in pion momenta is called the chiral expansion.

In contrast to QCD,  $\chi$ EFT is non-renormalizable in the usual sense. However, to any finite order in the EFT expansion, all the divergencies are absorbed by renormalizations of a finite number of parameters, called low-energy constants (LECs). The renormalized LECs are to be matched to QCD: in practice, either extracted from the lattice QCD results or fit to experimental data.

The number of unknown LECs grows quickly with the order (or precision) to which one wants to compute. For this reason, one might be tempted to dismiss such theory as having practically no predictive power. This indeed would be the case if the LECs are treated as entirely free parameters, i.e., allowed to take arbitrary values. They are not — their effect must be of *natural size* [111], which simply speaking means that the LECs may only have an effect consistent with the estimate based on *power counting* (i.e., in most cases the *naïve dimensional analysis*). When a certain LEC effect is unnaturally large, hence exceeds the expectation and/or requires the “promotion to a lower order”, the EFT should be revised to include the missing low-energy physics. On the other hand, when *naturalness* is implemented, the EFT is predictive and the uncertainty due to neglect of the higher-order corrections can be estimated.

The calculations with no divergencies, and/or no new constants to be fit, are genuine predictions of  $\chi$ EFT. Such examples are quite rare, however the calculation of nucleon polarizabilities presents one of them. The leading-order [ $O(p^3)$ ] contribution to nucleon polarizabilities is predictive, as there are no LECs renormalizing the polarizabilities [until  $O(p^4)$ ]. This case therefore presents a great testing ground of the  $\chi$ EFT framework.

To begin with, one can clearly see here that rather different predictions are obtained depending on whether the so-called *heavy-baryon (HB) expansion* [112] is employed [113, 114] or not [115, 116]. For example, for the proton dipole polarizabilities  $\{\alpha_{E1}, \beta_{M1}\}$  one obtains  $\{12.2, 1.2\}$  in HB $\chi$ PT, versus  $\{6.8, -1.8\}$  in  $\chi$ PT. The uncertainty on such a leading order prediction can be quite large and hence this discrepancy might not look as bad at first. The discrepancy deepens at the next order, i.e., with the inclusion of the  $\Delta(1232)$  as an explicit degree of freedom. The  $\Delta$  contributions to the nucleon polarizabilities come out to be large in HB $\chi$ PT [117] and ought to be canceled eventually by the LECs which are “promoted” from higher orders, cf. Griesshammer et al. [65], Hildebrandt et al. [118]. This problem is discussed at length in Refs. [49, 119]. For a more general overview of the  $\chi$ PT in the single-baryon sector (B $\chi$ PT) and the current status of the theory, see Geng [120].

The  $\Delta(1232)$ -resonance plays a prominent role in the modern formulation of  $\chi$ PT in the baryon sector. Its excitation energy,

$$\Delta = M_\Delta - M_N \simeq 293 \text{ MeV}, \quad (2.6)$$

is relatively low, and the  $\Delta$  must be included explicitly in the  $\chi$ PT Lagrangian. The construction of HB $\chi$ PT (semi-relativistic) Lagrangians with  $\Delta$ ’s, and decuplet fields in general, was considered in Refs. [112, 113]. The

manifestly Lorentz-invariant  $B\chi$ EFT Lagrangians with the spin-3/2  $\Delta$  fields were reviewed in [121, Sect. 4].

Concerning the power counting of the  $\Delta$  contributions, Hemmert et al. [122] coined the term “ $\epsilon$ -expansion”, whereas a different counting (“ $\delta$ -expansion”) was subsequently proposed by Pascalutsa and Phillips [123]. The two power-counting schemes differ in how much the excitation energy  $\Delta$  weighs in, compared with the pion mass  $m_\pi$ . In the  $\epsilon$ -expansion they are the same ( $\Delta \sim m_\pi$ ), while in the  $\delta$ -expansion  $m_\pi \ll \Delta$ . The main advantage of the latter is that it provides a systematic counting of the  $\Delta$ -pole contributions, which go as  $1/(p - \Delta)$  where  $p$  is the typical energy or momentum. Indeed, as  $p$  is of the same order as  $m_\pi$  and  $\Delta$ , the  $\epsilon$  counting implies that these contributions are always overwhelmingly important. In practice, however, the  $\epsilon$ -expansion counts these propagators as  $1/p$ . This works for the energies well below the resonance, but in the  $\Delta$ -resonance region these contributions are dominating and the power counting should reflect that. The  $\delta$  counting does just that transition. When  $p \sim m_\pi$ , the propagator  $1/(p - \Delta)$  counts as  $1/\Delta$ . When  $p \sim \Delta$  (the resonance region), the  $\Delta$ -pole contributions are summed yielding the dressed propagator  $1/(p - \Delta - \Sigma)$ , with  $\Sigma$  the self-energy of the  $\Delta$ , and the resulting dressed propagator counts as  $1/\Sigma \sim 1/p^3$ , since usually  $\Sigma \sim p^3$ .

Thus, the  $\delta$ -expansion is an EFT with a hierarchy of two low-energy scales and as such has two regimes,  $p \sim m_\pi$  (low-energy) and  $p \sim \Delta$  (resonance), where the  $\Delta$  contributions count differently. For definiteness, the following powers are assigned to the low-energy scales in the two regimes:

1. low-energy:  $m_\pi \sim p$ ,  $\Delta \sim p^{1/2}$ .
2. resonance:  $m_\pi \sim p^2$ ,  $\Delta \sim p$ .

Hence, e.g., the propagator  $1/(p - \Delta - \Sigma)$  is of  $O(p^{-1/2})$  in the first region and of  $O(p^{-3})$  in the second.

The present state-of-the-art calculations of CS observables, within  $HB\chi$ PT [51, 65] and  $B\chi$ PT [48, 49, 54], employ the  $\delta$ -expansion. Other applications of the  $\delta$ -expansion include: the forward VVCS [34, 124], pion-nucleon scattering [125], pion photo- [126] and electro-production [127, 128], radiative pion photoproduction [129, 130]. For the VVCS case, there is a significant discrepancy between two  $B\chi$ PT calculations, based on the  $\epsilon$  [33] and the  $\delta$  [34, 124] counting schemes, for some of the forward spin polarizabilities, see Fig. 7.4 and Fig. 7.6. This discrepancy is not yet completely understood.

Coming back to RCS, the  $B\chi$ PT calculation of Lensky and Pascalutsa [49] are done to next-to-next-to-leading order (NNLO), i.e. to  $O(p^{7/2})$ , in the low-energy region. To this order, these are genuine predictions of  $B\chi$ PT in the sense that all the parameters are determined from elsewhere; the LECs intrinsic to polarizabilities do not enter until  $O(p^4)$ . A very good description of the CS experimental data is nevertheless observed — a typical description of the unpolarized angular distribution is shown in Fig. 2.5.

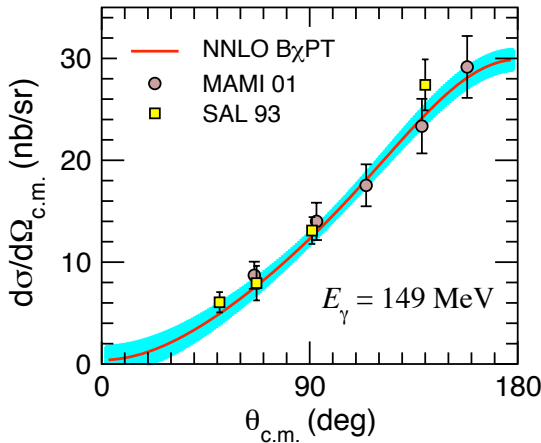


Figure 2.5: Results of the  $B\chi$ PT calculation [49] for the differential cross section of proton Compton scattering (red curve with the band), compared with the experimental data from SAL [11] and MAMI [17].

The numerical composition of the various contributions to the dipole polarizabilities of the proton is given in  $B\chi$ PT by (in units of  $10^{-4} \text{ fm}^3$ ):

$$\alpha_{E1}^{(p)} = \underbrace{6.8}_{O(p^3)} + \underbrace{(-0.1 + 4.5)}_{O(p^{7/2})} = 11.2, \quad (2.7a)$$

$$\beta_{M1}^{(p)} = \underbrace{-1.8}_{O(p^3)} + \underbrace{(7.1 - 1.4)}_{O(p^{7/2})} = 3.9, \quad (2.7b)$$

where the first number in  $O(p^{7/2})$  comes from the  $\Delta$ -resonance excitation while the second comes from the  $\pi\Delta$  loops. One sees that the  $\Delta$ -excitation is mainly affecting the magnetic polarizability and is of paramagnetic nature (i.e., positive contribution to  $\beta_{M1}$ ). This is expected from the first nucleon excitation which predominantly is of  $M1$  type. The pion loops, playing here the role of the “pion cloud”, induce the diamagnetic effects (i.e., negative  $\beta_{M1}$ ).

These  $B\chi$ PT results can be contrasted with the corresponding  $HB\chi$ PT calculation [117]:

$$\alpha_{E1}^{(p)}(\text{HB}) = 12.2 (\pi\text{N loop}) + 0 (\Delta \text{ pole}) + 8.6 (\pi\Delta \text{ loop}) = 20.8, \quad (2.8a)$$

$$\beta_{M1}^{(p)}(\text{HB}) = 1.2 (\pi\text{N loop}) + 12 (\Delta \text{ pole}) + 1.5 (\pi\Delta \text{ loop}) = 14.7. \quad (2.8b)$$

Table 2.1: Predictions for the *proton* static dipole, quadrupole, and dispersive polarisabilities, in units of  $10^{-4} \text{ fm}^3$  (dipole) and  $10^{-4} \text{ fm}^5$  (quadrupole and dispersive), compared with the  $\chi$ PT-based fits dipole polarizabilities to RCS database. The latest PDG values for dipole polarizabilities are shown too.

Source	$\alpha_{E1}$	$\beta_{M1}$	$\alpha_{E2}$	$\beta_{M2}$	$\alpha_{E1\nu}$	$\beta_{M1\nu}$
HB $\chi$ PT fit [65]	$10.65 \pm 0.50$	$3.15 \pm 0.50$	...	...	...	...
B $\chi$ PT fit [52]	$10.6 \pm 0.5$	$3.2 \pm 0.5$	...	...	...	...
B $\chi$ PT NNLO [54]	$11.2 \pm 0.7$	$3.9 \pm 0.7$	$17.3 \pm 3.9$	$-15.5 \pm 3.5$	$-1.3 \pm 1.0$	$7.1 \pm 2.5$
PDG [71]	$11.2 \pm 0.4$	$2.5 \pm 0.4$	...	...	...	...

Here the chiral loops give a much larger (than in B $\chi$ PT) effect in the electric polarizability, while in the magnetic they even have an opposite sign. As the result, both polarizabilities come out to be way above their empirical values. As noted above, this discrepancy is usually corrected by promoting the higher-order [ $O(p^4)$ ] LECs, at the expense of violating the naturalness requirement.

Recently, the B $\chi$ PT framework of Ref. [49] has been extended to the  $\Delta$ -resonance region [54], with an update on the predictions for  $\alpha_{E1}$  and  $\beta_{M1}$  (included in the above numbers for the proton). Predictions for the spin and higher-order polarizabilities have also been obtained. The results for the scalar polarizabilities of the proton are presented in Table 2.1, where they are compared with the  $\chi$ PT results obtained by fitting the experimental RCS cross sections. The fitting in Refs. [52, 65] is done using LECs from the orders beyond NNLO. The fact that the B $\chi$ PT fit [52] and prediction [54] agree, within the uncertainties, indicates that the LEC effect (which is the only difference between the two calculations) is of natural size.

A number of predictions for polarized CS observables, emphasizing the role of the chiral loops, are given in Ref. [54] as well, see e.g., Fig. 4.8 below. The corresponding results for the proton spin polarizabilities are shown in Table 4.2.

A brief summary of the  $\chi$ PT results for the nucleon polarizabilities is given in Sect. 7. The HB $\chi$ PT calculations therein have recently been reviewed by McGovern et al. [51].

### 3. Polarizabilities in Compton Scattering

#### 3.1. Compton Processes

The CS processes, represented by Fig. 3.1, can be classified according to the photon virtualities,  $q^2$  and  $q'^2$ , while the target particle (hereby the nucleon) is on the mass shell:  $p^2 = p'^2 = M^2$ . The Mandelstam variables for this two-body scattering process are:

$$s = (p + q)^2 = M^2 + 2p \cdot q + q^2 = (p' + q')^2, \quad (3.1a)$$

$$u = (p' - q)^2 = M^2 - 2p' \cdot q + q^2 = (p - q')^2, \quad (3.1b)$$

$$t = (p - p')^2 = 2M^2 - 2p \cdot p' = (q - q')^2. \quad (3.1c)$$

Their sum is as usual given by the sum of invariant masses squared:  $s + t + u = 2M^2 + q^2 + q'^2$ . Throughout the paper we use the following kinematical invariants,

$$\nu = p \cdot q / M, \quad \nu' = p \cdot q' / M, \quad (3.2)$$

which in the lab frame become the energy of, respectively, the incoming and outgoing photon.

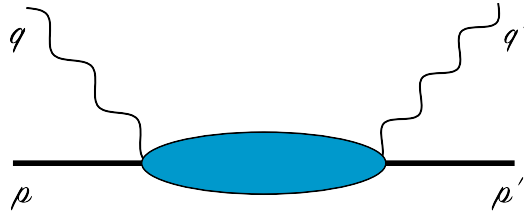


Figure 3.1: The Compton scattering off the nucleon:  $\gamma(q) + N(p) \rightarrow \gamma(q') + N(p')$ .

In the most general case, the initial and final photons are virtual, with different virtualities,  $q^2 \neq q'^2$ . In reality, this situation may occur in the dilepton electro-production,  $e^- N \rightarrow e^- N e^+ e^-$ , the  $N\bar{N}$  production in  $e^+ e^-$  collisions, or in the two-photon-exchange contribution to lepton-nucleon scattering, discussed in Sect. 6 in the context of atomic calculations.

Denoting the photon helicity by  $\lambda_\gamma = \pm 1, 0$  and the nucleon helicity by  $\lambda_N = \pm 1/2$ , there are obviously  $3 \times 3 \times 2 \times 2 = 36$  helicity amplitudes,  $T_{\lambda'_\gamma \lambda'_N \lambda_\gamma \lambda_N}(s, t)$ , describing this process. Discrete symmetries, such as parity and time reversal, reduce the number of independent helicity amplitudes by more than a half, as will be discussed in more detail below.

The Feynman amplitude  $T^{\mu\nu}$  describing this process is a rank-2 tensor-spinor which depends on the four-momenta  $q, q', p, p'$ . Due to momentum conservation, three of them are independent, e.g.:  $q, q'$ , and  $P = \frac{1}{2}(p + p')$ . The helicity amplitudes are expressed in terms of the Feynman amplitude as:

$$T_{\lambda'_\gamma \lambda'_N \lambda_\gamma \lambda_N} = \bar{u}_{\lambda'_N}(\mathbf{p}') \varepsilon_{\lambda'_\gamma}^*(q') \cdot T(q', q, P) \cdot \varepsilon_{\lambda_\gamma}(q) u_{\lambda_N}(\mathbf{p}), \quad (3.3)$$

with the nucleon spinors and photon polarization vectors defined in Sect. 1.1. A consequence of the e.m. gauge invariance is

$$q'_\mu T^{\mu\nu}(q', q, P) = 0 = q_\nu T^{\mu\nu}(q', q, P), \quad (3.4)$$

valid for on-shell nucleons and arbitrary photon virtualities. The Lorentz decomposition of the Feynman amplitude in terms of the invariant amplitudes  $\mathcal{A}_i$ ,

$$T^{\mu\nu}(q', q, P) = e^2 \sum_i \mathcal{O}_i^{\mu\nu} \mathcal{A}_i(\nu', q'^2, \nu, q^2), \quad (3.5)$$

contains 18 terms, after the constraints due to parity, time reversal and gauge invariance are taken into account [131]. For off-forward VVCS with  $q'^2 = q^2$ , this number reduces to 12; for forward VVCS, to 4. For the rest of this section we restrict ourselves to the RCS, i.e., the case where both photons are real ( $q'^2 = q^2 = 0$ ). The case where one of the photons is virtual (VCS and timelike CS) is briefly discussed in Sect. 4. The forward doubly-virtual CS appears prominently in Sect. 5 and 6.

### 3.2. Helicity Amplitudes

Consider the classic CS: the elastic scattering of a real photon, or real CS (RCS). The RCS on a spin-1/2 target is described by the helicity amplitudes,  $T_{\lambda'_\gamma \lambda'_N \lambda_\gamma \lambda_N}(s, t)$ , subject to the following parity ( $\mathcal{P}$ ) and time-reversal ( $\mathcal{T}$ ) constraints:

$$\mathcal{P} : \quad T_{-\lambda'_\gamma - \lambda'_N - \lambda_\gamma - \lambda_N}(s, t) = (-1)^{\lambda'_\gamma - \lambda'_N - \lambda_\gamma + \lambda_N} T_{\lambda'_\gamma \lambda'_N \lambda_\gamma \lambda_N}(s, t), \quad (3.6a)$$

$$\mathcal{T} : \quad T_{\lambda_\gamma \lambda_N \lambda'_\gamma \lambda'_N}(s, t) = (-1)^{\lambda_\gamma - \lambda'_N - \lambda_\gamma + \lambda_N} T_{\lambda'_\gamma \lambda'_N \lambda_\gamma \lambda_N}(s, t). \quad (3.6b)$$

These constraints reduce the number of independent amplitudes from  $2 \times 2 \times 2 \times 2 = 16$  to 6. The amplitudes in this case depend only on the combined (or total) helicities,  $H = \lambda_\gamma - \lambda_N$ ,  $H' = \lambda'_\gamma - \lambda'_N$ , which run through  $\pm 1/2$ ,  $\pm 3/2$ , and the above constraints read:

$$T_{H'H}(s, t) \stackrel{\mathcal{P}}{=} (-1)^{H'-H} T_{-H' -H}(s, t) \stackrel{\mathcal{T}}{=} (-1)^{H'-H} T_{HH'}(s, t). \quad (3.7)$$

The six independent amplitudes are usually chosen as follows [84]:

$$\begin{aligned} (8\pi s^{1/2}) \Phi_1 &\equiv T_{-1/2 -1/2} = T_{+1/2 +1/2}, \\ (8\pi s^{1/2}) \Phi_2 &\equiv T_{-1/2 +1/2} = -T_{+1/2 -1/2}, \\ (8\pi s^{1/2}) \Phi_3 &\equiv T_{-1/2 +3/2} = T_{+1/2 -3/2} = T_{+3/2 -1/2} = T_{-3/2 +1/2}, \\ (8\pi s^{1/2}) \Phi_4 &\equiv T_{-1/2 -3/2} = -T_{+1/2 +3/2} = T_{+3/2 +1/2} = -T_{-3/2 -1/2}, \\ (8\pi s^{1/2}) \Phi_5 &\equiv T_{+3/2 +3/2} = T_{-3/2 -3/2}, \\ (8\pi s^{1/2}) \Phi_6 &\equiv T_{-3/2 +3/2} = -T_{+3/2 -3/2}. \end{aligned} \quad (3.8)$$

Their normalization is chosen such that, given the unpolarized cross section element,

$$d\sigma^{\text{unpol.}} = \frac{dt}{16\pi(s - M^2)^2} \frac{1}{4} \sum_{HH'} |T_{H'H}|^2, \quad (3.9)$$

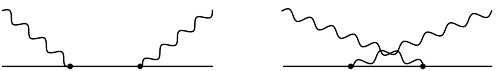
the unpolarized angular distribution in the center-of-mass frame is:

$$\frac{d\sigma^{\text{unpol.}}}{d\Omega_{cm}} = \frac{1}{64\pi^2 s} \frac{1}{4} \sum_{HH'} |T_{H'H}|^2 = \frac{1}{2} |\Phi_1|^2 + \frac{1}{2} |\Phi_2|^2 + |\Phi_3|^2 + |\Phi_4|^2 + \frac{1}{2} |\Phi_5|^2 + \frac{1}{2} |\Phi_6|^2. \quad (3.10)$$

Incidentally, the conversion to the lab frame goes as:

$$\frac{d\sigma}{d\Omega_L} = \frac{d\Omega_{cm}}{d\Omega_L} \frac{d\sigma}{d\Omega_{cm}} = \left(\frac{\nu'}{\nu}\right)^2 \frac{s}{M^2} \frac{d\sigma}{d\Omega_{cm}}. \quad (3.11)$$

As a simple illustration consider the RCS in tree-level QED, described by the following Feynman amplitude:



$$T^{(1)\mu\nu} = -e^2 \left( \gamma^\mu \frac{\not{p} + \not{q} + M}{s - M^2} \gamma^\nu + \gamma^\nu \frac{\not{p}' - \not{q} + M}{u - M^2} \gamma^\mu \right). \quad (3.12)$$

Figure 3.2: Tree-level CS graphs.

Using Eq. (3.3) and definitions from Sect. 1.1, one easily obtains the

following expressions for the helicity amplitudes:<sup>2</sup>

$$\begin{aligned}
8\pi s^{1/2} \Phi_1^{(1)} &\equiv T_{+1+1/2+1+1/2}^{(1)} = -\pi\alpha \frac{(M\eta - 2t\nu)\eta^{1/2}}{M\nu^2\nu'}, \\
8\pi s^{1/2} \Phi_2^{(1)} &\equiv T_{-1-1/2+1+1/2}^{(1)} = \pi\alpha \frac{(-t)^{3/2}}{\nu^2\nu'}, \\
8\pi s^{1/2} \Phi_3^{(1)} &\equiv T_{-1+1/2+1+1/2}^{(1)} = \pi\alpha \frac{t\eta^{1/2}}{\nu^2\nu'}, \\
8\pi s^{1/2} \Phi_4^{(1)} &\equiv T_{+1-1/2+1+1/2}^{(1)} = \pi\alpha \frac{(-t)^{1/2}\eta}{\nu^2\nu'}, \\
8\pi s^{1/2} \Phi_5^{(1)} &\equiv T_{-1+1/2-1+1/2}^{(1)} = -\pi\alpha \frac{\eta^{3/2}}{\nu^2\nu'}, \\
8\pi s^{1/2} \Phi_6^{(1)} &\equiv T_{-1+1/2+1-1/2}^{(1)} = -\pi\alpha \frac{(-t)^{3/2}s}{M^2\nu^2\nu'},
\end{aligned} \tag{3.13}$$

where the superscript on the amplitudes indicates that they are of first order in  $\alpha$ , and the kinematical invariants are:

$$\eta = \frac{M^4 - su}{M^2}, \quad \nu = \frac{s - M^2}{2M}, \quad \nu' = \frac{M^2 - u}{2M}. \tag{3.14}$$

Substituting these expressions in Eq. (3.10), one obtains the Klein-Nishina cross section [133]:

$$\frac{d\sigma^{\text{KN}}}{d\Omega_L} = \frac{\alpha^2}{2M^2} \left(\frac{\nu'}{\nu}\right)^2 \left(\frac{\nu'}{\nu} + \frac{\nu}{\nu'} - \sin^2 \vartheta\right), \tag{3.15}$$

where  $\sin^2 \vartheta = 1 - (1 + t/2\nu\nu')^2 = -t\eta/(2\nu\nu')^2$ .

The same steps can be done for polarized observables. For instance, for the linearly polarized photon beam we have:

$$\frac{d\sigma}{d\Omega_{cm}} \Sigma_3 \equiv \frac{1}{2} \left( \frac{d\sigma_{||}}{d\Omega_{cm}} - \frac{d\sigma_{\perp}}{d\Omega_{cm}} \right) = -\text{Re} [(\Phi_1 + \Phi_5)\Phi_3^* + (\Phi_2 - \Phi_6)\Phi_4^*], \tag{3.16}$$

where  $\Sigma_3$  is the beam asymmetry. The tree-level QED result is given by:

$$\frac{d\sigma_{||}}{d\Omega_L} - \frac{d\sigma_{\perp}}{d\Omega_L} = -\frac{\alpha^2}{M^2} \left(\frac{\nu'}{\nu}\right)^2 \sin^2 \vartheta. \tag{3.17}$$

This result holds (in tree-level QED) for RCS on a particle with spin 0, 1/2, 1. It would be interesting to establish it for higher spins as well.

### 3.3. Multipole Expansion

A better use of the rotational and discrete symmetries is made by the partial-wave expansion in the center-of-mass system:

$$T_{H'H}(\omega, \theta) = \sum_{J=1/2}^{\infty} (2J+1) T_{H'H}^J(\omega) d_{HH'}^J(\theta), \tag{3.18a}$$

$$T_{H'H}^J(\omega) = \frac{1}{2} \int_{-1}^1 d(\cos \theta) T_{H'H}(\omega, \theta) d_{HH'}^J(\theta), \tag{3.18b}$$

where  $J$  is total angular momentum and  $d^J(\theta)$  are the Wigner  $d$ -functions.<sup>3</sup> The partial wave-amplitudes  $T^J$  and the  $d$ -functions satisfy the symmetry relations (3.7) separately.

<sup>2</sup>This, up to a phase convention which flips the sign of  $\Phi_{2,4,6}$ , agrees with Tsai et al. [132, Eq. (5)].

<sup>3</sup>For the  $d$ -functions we use the conventions of Edmonds (also used by Davydov, or Varshalovich). In the other popular convention (Rose, Wigner or Landau and Lifshitz) the sign of  $\theta$  is the opposite and hence, due to the property  $d_{HH'}^J(-\theta) = d_{H'H}^J(\theta)$ , the helicities appearing on the  $d$ -functions would be interchanged.

Assuming the parity to be a good quantum number, it is convenient to form the partial-wave amplitudes with definite  $J^P$ :

$$\mathcal{A}_p^J = \Phi_1^J + p\Phi_2^J = \frac{1}{8\pi s^{1/2}} \left( T_{+1/2+1/2}^J - p T_{+1/2-1/2}^J \right), \quad (3.19a)$$

$$\mathcal{B}_p^J = -p\Phi_3^J - \Phi_4^J = \frac{1}{8\pi s^{1/2}} \left( T_{+1/2+3/2}^J - p T_{+1/2-3/2}^J \right), \quad (3.19b)$$

$$\mathcal{C}_p^J = \Phi_5^J + p\Phi_6^J = \frac{1}{8\pi s^{1/2}} \left( T_{+3/2+3/2}^J - p T_{+3/2-3/2}^J \right), \quad (3.19c)$$

where  $p = \pm$  is the parity eigenvalue. Note that in the above partial-wave expansion neither  $H$  nor  $H'$  exceed  $J$ , hence the amplitudes  $\mathcal{B}$  and  $\mathcal{C}$  are only defined for  $J \geq 3/2$ .

The conventional multipole amplitudes (*multipoles* for short) are denoted as [134, 135]

$$f_{\rho'\rho}^{\ell\mp}(\omega), \text{ with } \ell = J \pm 1/2, \text{ and } \rho', \rho = E, M. \quad (3.20)$$

The combination of  $\rho$  and  $\ell$  reflects the photon multipolarity (e.g.,  $E1$  the electric dipole). The multipoles are expressed in terms of the partial-wave amplitudes as follows.

For  $J = 1/2$ :

$$f_{MM}^{1-} = \frac{1}{2} \mathcal{A}_{\pm}^{J=1/2}, f_{\rho'\rho}^{0+} = 0. \quad (3.21a)$$

For  $J \geq 3/2$ :

$$f_{MM}^{(J+1/2)-} = \frac{2}{(2J+1)^2} \left( \mathcal{A}_{\pm}^J - 2\sqrt{\frac{J-1/2}{J+3/2}} \mathcal{B}_{\pm}^J + \frac{J-1/2}{J+3/2} \mathcal{C}_{\pm}^J \right), \quad (3.21b)$$

$$f_{MM}^{(J-1/2)+} = \frac{2}{(2J+1)^2} \left( \mathcal{A}_{\mp}^J + 2\sqrt{\frac{J+3/2}{J-1/2}} \mathcal{B}_{\mp}^J + \frac{J+3/2}{J-1/2} \mathcal{C}_{\mp}^J \right), \quad (3.21c)$$

$$f_{ME}^{(J-1/2)+} = \frac{2}{(2J+1)^2} \left( -\mathcal{A}_{\mp}^J - \frac{2}{\sqrt{(J+3/2)(J-1/2)}} \mathcal{B}_{\mp}^J + \mathcal{C}_{\mp}^J \right). \quad (3.21d)$$

The inverse relation can be written as (in shorthand notation,  $f_{EE\pm MM} = f_{EE} \pm f_{MM}$ ):

$$\Phi_1^J = \frac{1}{4} \{ (J+3/2)^2 f_{EE\pm MM}^{(J+1/2)-} \pm (J-1/2)^2 f_{EE\pm MM}^{(J-1/2)+} \mp 2(J+3/2)(J-1/2) f_{EM\pm ME}^{(J-1/2)+} \}, \quad (3.22a)$$

$$\Phi_3^J = \frac{1}{4} \sqrt{(J+3/2)(J-1/2)} \{ (J+3/2) f_{EE\mp MM}^{(J+1/2)-} \pm (J-1/2) f_{EE\mp MM}^{(J-1/2)+} \mp 2 f_{EM\mp ME}^{(J-1/2)+} \}, \quad (3.22b)$$

$$\Phi_5^J = \frac{1}{4} (J+3/2)(J-1/2) \{ f_{EE\pm MM}^{(J+1/2)-} \pm f_{EE\pm MM}^{(J-1/2)+} \pm 2 f_{EM\pm ME}^{(J-1/2)+} \}. \quad (3.22c)$$

As an illustration we once again consider the tree-level QED, and for greater simplicity take the zero-energy limit,  $\omega = 0$ . According to the low-energy theorem (LET) [136–138], the tree-level result in this limit is exact and we may omit the label indicating the order of  $\alpha$ . The zero-energy helicity amplitudes is thus given by:

$$\Phi_1(0, \theta) = \mp \frac{\alpha}{M} \left( \frac{1}{2} \pm \frac{1}{2} \cos \theta \right)^{3/2}, \Phi_3(0, \theta) = \frac{\alpha}{M} \left( \frac{1}{2} \mp \frac{1}{2} \cos \theta \right) \left( \frac{1}{2} \pm \frac{1}{2} \cos \theta \right)^{1/2}, \Phi_5(0, \theta) = \pm \Phi_1(0, \theta), \quad (3.23)$$

while the non-vanishing partial-wave amplitudes are:

$$\Phi_1^{J=1/2}(0) = \mp \frac{\alpha}{2M} \int_{-1}^1 d(\cos \theta) \left( \frac{1 \pm \cos \theta}{2} \right)^{3/2} d_{+1/2\pm 1/2}^{1/2}(\theta) = -\frac{\alpha}{3M}, \quad \Phi_1^{J=3/2}(0) = \mp \frac{\alpha}{12M}, \quad (3.24a)$$

$$\Phi_3^{J=3/2}(0) = \mp \frac{\alpha}{2M} \int_{-1}^1 d(\cos \theta) \frac{1 \mp \cos \theta}{2} \left( \frac{1 \pm \cos \theta}{2} \right)^{1/2} d_{+1/2\mp 3/2}^{3/2}(\theta) = \mp \frac{\alpha}{4\sqrt{3}M}, \quad (3.24b)$$

$$\Phi_5^{J=3/2}(0) = -\frac{\alpha}{2M} \int_{-1}^1 d(\cos \theta) \left( \frac{1 \pm \cos \theta}{2} \right)^{3/2} d_{+3/2\pm 3/2}^{3/2}(\theta) = \mp \frac{\alpha}{4M}. \quad (3.24c)$$



The parity-conserving amplitudes assume the following values:

$$\mathcal{A}_{\pm}^{J=1/2} = \frac{\alpha}{M} \begin{pmatrix} -\frac{2}{3} \\ 0 \end{pmatrix}, \mathcal{A}_{\pm}^{J=3/2} = \frac{\alpha}{M} \begin{pmatrix} 0 \\ -\frac{1}{6} \end{pmatrix}, \mathcal{B}_{\pm}^{J=3/2} = \frac{\alpha}{M} \begin{pmatrix} 0 \\ -\frac{1}{2\sqrt{3}} \end{pmatrix}, \mathcal{C}_{\pm}^{J=3/2} = \frac{\alpha}{M} \begin{pmatrix} 0 \\ -\frac{1}{2} \end{pmatrix}, \quad (3.25)$$

and as the result, there are only two non-vanishing multipoles which happen to be equal (at  $\omega = 0$ ):

$$f_{EE}^{1-}(0) = f_{EE}^{1+}(0) = -\frac{\alpha}{3M}. \quad (3.26)$$

### 3.4. Tensor Decompositions

For various microscopic calculations, as well as for the general low-energy expansion (LEX), it is convenient to isolate the Lorentz structure of the amplitude by decomposing it into a set of tensors. There are several neat decompositions described in the literature, we only consider two of them here. The first — perhaps the earliest one — is the following decomposition into a non-covariant set of 6 (minimal number) tensors:

$$\bar{u}'(\varepsilon' \cdot T \cdot \varepsilon)u = 2Me^2 \hat{A}^T(s, t) \chi' \varepsilon'_i \hat{O}_{ij} \varepsilon_j \chi, \quad (3.27a)$$

with  $\hat{A}$  and  $\hat{O}$  being respectively the arrays of the scalar complex amplitudes and tensors:

$$\hat{A}(s, t) = \{A_1, \dots, A_6\}(s, t), \quad (3.27b)$$

$$\hat{O}_{ij} = \{\delta_{ij}, n_i n'_j, i\epsilon_{ijk} \sigma_k, \delta_{ij} i\epsilon_{klm} \sigma_k n'_l n_m, i\epsilon_{klm} \sigma_k (\delta_{il} n_m n'_j - \delta_{jl} n_i n'_m), i\epsilon_{klm} \sigma_k (\delta_{il} n'_m n'_j - \delta_{jl} n_i n_m)\}, \quad (3.27c)$$

where  $\mathbf{n}$  and  $\mathbf{n}'$  are the directions of the incoming and outgoing photons.

The second decomposition considered here is a covariant, overcomplete set of 8 tensors [? ]:

$$\bar{u}'(\varepsilon' \cdot T \cdot \varepsilon)u = e^2 \hat{\mathcal{A}}^T(s, t) \bar{u}' \hat{\mathcal{O}}^{\mu\nu} u \mathcal{E}'_{\mu} \mathcal{E}_{\nu}, \quad (3.28a)$$

with<sup>4</sup>

$$\hat{\mathcal{A}}(s, t) = \{\mathcal{A}_1, \dots, \mathcal{A}_8\}(s, t), \quad (3.28b)$$

$$\hat{\mathcal{O}}^{\mu\nu} = \{-g^{\mu\nu}, q^{\mu} q'^{\nu}, -\gamma^{\mu\nu}, g^{\mu\nu}(q' \cdot \gamma \cdot q), q^{\mu} q'_{\alpha} \gamma^{\alpha\nu} - \gamma^{\alpha\mu} q_{\alpha} q'^{\nu}, q^{\mu} q_{\alpha} \gamma^{\alpha\nu} - \gamma^{\alpha\mu} q'_{\alpha} q'^{\nu}, q^{\mu} q'^{\nu}(q' \cdot \gamma \cdot q), -i\gamma_5 \epsilon^{\mu\nu\alpha\beta} q'_{\alpha} q_{\beta}\}, \quad (3.28c)$$

$$\mathcal{E}_{\mu} = \varepsilon_{\mu} - \frac{P \cdot \varepsilon}{P \cdot q} q_{\mu}, \quad \mathcal{E}'_{\mu} = \varepsilon'_{\mu} - \frac{P \cdot \varepsilon'}{P \cdot q} q'_{\mu}, \quad P_{\mu} = \frac{1}{2}(p + p')_{\mu}, \quad P \cdot q = P \cdot q' = M\xi. \quad (3.28d)$$

This decomposition is manifestly gauge-invariant, because the vectors  $\mathcal{E}$  are. It can be reduced [54] to any of the covariant sets with the minimum number of tensors, such as that of Hearn and Leader [84] or L'vov [96]. Nevertheless, the overcomplete set is better suited for practical calculations of Feynman diagrams using computer algebra, since simple Gordon-like identities are sufficient for the decomposition. Another advantage is that it readily applies to the forward VVCS case, see Sect. 5.1.

The correct relation between the amplitudes  $A_{1,\dots,6}$  and  $\mathcal{A}_{1,\dots,8}$  was given by McGovern et al. [51]:

$$\begin{aligned} A_1 &= \frac{\epsilon_B}{M} \mathcal{A}_1 + \frac{\omega_B t}{2M} \mathcal{A}_4, \\ A_2 &= \frac{\epsilon_B \omega_B^2}{M} \mathcal{A}_2 + \frac{\omega_B^3}{M} (\mathcal{A}_5 + \mathcal{A}_6 - \frac{1}{2} t \mathcal{A}_7), \\ A_3 &= \frac{\epsilon_B}{M} \mathcal{A}_3 - \frac{M^2 \eta t}{4M^2 - t} \left( \frac{\mathcal{A}_5 + \mathcal{A}_6}{2M(\epsilon_B + M)} - \mathcal{A}_7 \right) - \frac{\omega_B t}{2M} \mathcal{A}_8, \\ A_4 &= \omega_B^2 \mathcal{A}_4, \\ A_5 &= \omega_B^2 \mathcal{A}_5 + \frac{\omega_B^2}{2M(\epsilon_B + M)} \left[ \frac{1}{2} \mathcal{A}_3 + \frac{M^2 \eta}{4M^2 - t} (\mathcal{A}_5 + \mathcal{A}_6) \right] - \omega_B^2 (\omega_B^2 + \frac{1}{2} t) \mathcal{A}_7 + \frac{\omega_B^3}{2M} \mathcal{A}_8, \\ A_6 &= \omega_B^2 \mathcal{A}_6 - \frac{\omega_B^2}{2M(\epsilon_B + M)} \left[ \frac{1}{2} \mathcal{A}_3 + \frac{M^2 \eta}{4M^2 - t} (\mathcal{A}_5 + \mathcal{A}_6) \right] + \omega_B^4 \mathcal{A}_7 - \frac{\omega_B^3}{2M} \mathcal{A}_8, \end{aligned} \quad (3.29)$$

<sup>4</sup>Here we correct the typos of Refs. [51? ] made in the expressions for  $\mathcal{O}_6$  and  $\mathcal{O}_8$ , respectively.

where  $\epsilon_B$  and  $\omega_B$  are the nucleon and photon energies in the Breit frame (defined by  $\mathbf{p}' = -\mathbf{p}$ ). These kinematical variables, along with  $\eta$ , can be expressed in terms of Mandelstam invariants, cf. [Appendix C](#). Thus, although obtained in the Breit frame, this relation is Lorentz invariant.

Both sets of amplitudes have a definite parity under the photon crossing (i.e.,  $\varepsilon \leftrightarrow \varepsilon'$ ,  $q \leftrightarrow q'$ , hence  $s \leftrightarrow u$ , etc.). Writing the amplitudes as functions of  $\xi$  and  $t$ , the crossing symmetry implies:

$$A_{1,2}(-\xi, t) = A_{1,2}(\xi, t), \quad A_{3,\dots,6}(-\xi, t) = -A_{3,\dots,6}(\xi, t), \quad (3.30a)$$

$$\mathcal{A}_{1,2,8}(-\xi, t) = \mathcal{A}_{1,2,8}(\xi, t), \quad \mathcal{A}_{3,\dots,7}(-\xi, t) = -\mathcal{A}_{3,\dots,7}(\xi, t). \quad (3.30b)$$

### 3.5. Unitarity Relations

#### 3.5.1. Optical Theorem

Derived from unitarity, the optical theorem establishes the relation between the imaginary part of the forward CS amplitude and the total photoabsorption cross section, and in our case of the nucleon target reads:

$$\text{Im } T_{H'H}(\nu, 0) = \nu \sigma_H(\nu) \delta_{HH'}, \quad (3.31)$$

where  $\delta_{HH'}$  is the Kronecker symbol. The cross section  $\sigma_H$  corresponds with the absorption of a circularly polarized photon on a longitudinally polarized target, with their combined helicity given by  $H$ . In terms of the invariant amplitudes we have:

$$\text{Im } A_1(\nu, 0) = \text{Im } \mathcal{A}_1(\nu, 0) = \frac{\nu}{4\pi\alpha} \sigma_T(\nu), \quad (3.32a)$$

$$\text{Im } A_3(\nu, 0) = \text{Im } \mathcal{A}_3(\nu, 0) = \frac{\nu}{4\pi\alpha} \sigma_{TT}(\nu), \quad (3.32b)$$

where  $\sigma_T = (\sigma_{1/2} + \sigma_{3/2})/2$  is the unpolarized cross section and  $\sigma_{TT} = (\sigma_{1/2} - \sigma_{3/2})/2$ . The remaining amplitudes do not contribute in the forward scattering, and as such are not constrained by the optical theorem.

#### 3.5.2. Watson's Theorem Extended

At low energies there are further unitarity constraints for the nucleon CS. They are less strict, since they hold in a limited energy range and to leading order in  $\alpha$ . At the same time, they are more stringent, since they apply to all the multipole and partial-wave amplitudes, and hence are not limited to the forward kinematics.

Below the two-pion threshold, one is limited to the channel space spanned by the  $\pi N$  and  $\gamma N$  states, and hence the following four processes:

$$\begin{aligned} \pi N &\rightarrow \pi N, & \pi N &\rightarrow \gamma N, \\ \gamma N &\rightarrow \pi N, & \gamma N &\rightarrow \gamma N. \end{aligned} \quad (3.33)$$

To have exact unitarity, in this channel space, we set up a linear coupled-channel integral equation:

$$\begin{pmatrix} T_{\pi\pi} & T_{\pi\gamma} \\ T_{\gamma\pi} & T_{\gamma\gamma} \end{pmatrix} = \begin{pmatrix} V_{\pi\pi} & V_{\pi\gamma} \\ V_{\gamma\pi} & V_{\gamma\gamma} \end{pmatrix} + \begin{pmatrix} V_{\pi\pi} & V_{\pi\gamma} \\ V_{\gamma\pi} & V_{\gamma\gamma} \end{pmatrix} \begin{pmatrix} G_\pi & 0 \\ 0 & G_\gamma \end{pmatrix} \begin{pmatrix} T_{\pi\pi} & T_{\pi\gamma} \\ T_{\gamma\pi} & T_{\gamma\gamma} \end{pmatrix}, \quad (3.34)$$

where  $T$  and  $V$  are suitably normalized amplitudes and potentials of pion-nucleon scattering ( $\pi\pi$ ), pion photoproduction ( $\pi\gamma$ ), absorption ( $\gamma\pi$ ), and nucleon CS ( $\gamma\gamma$ ). The propagators  $G_\pi$  and  $G_\gamma$  are, respectively, the pion-nucleon and photon-nucleon two-particle propagators. With the assumption of hermiticity of the potential and time-reversal symmetry, which relates the  $\gamma\pi$  and  $\pi\gamma$  amplitudes, the above equation leads to the unitary  $S$ -matrix,  $S_{fi} = \delta_{fi} + 2iT_{fi}$ .

Neglecting the iterations of the potential involving photons (which amount to small radiative corrections), the coupled-channel equation reduces to:

$$T_{\pi\pi} = V_{\pi\pi} + V_{\pi\pi} G_\pi T_{\pi\pi}, \quad (3.35a)$$

$$T_{\pi\gamma} = V_{\pi\gamma} + T_{\pi\pi} G_\pi V_{\pi\gamma}, \quad (3.35b)$$

$$T_{\gamma\pi} = V_{\gamma\pi} + V_{\gamma\pi} G_\pi T_{\pi\pi}, \quad (3.35c)$$

$$T_{\gamma\gamma} = V_{\gamma\gamma} + V_{\gamma\pi} G_\pi T_{\pi\gamma}. \quad (3.35d)$$

Only the first of these is an integral equation, the rest are obtained by a one-loop calculation.

After the partial-wave expansion, the solution for the  $\pi N$  amplitude can be written as:

$$T_{\pi\pi}^{IJp} = \frac{K^{IJp}}{1 - ikK^{IJp}} = \frac{1}{k} e^{i\delta_{\ell p}^I} \sin \delta_{\ell p}^I, \quad (3.36)$$

where  $K^{IJp}$  is the ‘ $K$ -matrix’ with definite isospin  $I$ , total angular momentum  $J$ , and parity  $p$ ; the corresponding  $\pi N$  phase-shift is  $\delta_{\ell p}^I = \arctan(kK^{IJp})$ , which is a function of the  $\pi N$  relative momentum  $k$ . The latter is given by

$$k = \frac{1}{2s^{1/2}} [(s - (M + m_\pi)^2) ((s - (M - m_\pi)^2)]^{1/2}. \quad (3.37)$$

Note that we have neither specified  $V_{\pi\pi}$ , nor solved Eq. (3.35a); we have merely written it in the manifestly unitary form.

Continuing to the pion photoproduction channel, we obtain the statement of the celebrated Watson’s theorem [139]:

$$T_{\gamma\pi}^{IJp} = |T_{\gamma\pi}^{IJp}| e^{i\delta_{\ell p}^I}, \quad (3.38)$$

with  $\ell = J - p/2$ . The phase of the photoproduction amplitudes is thus identical to the  $\pi N$  phase-shift, for each set of good quantum numbers.

Extending these arguments to the Compton channel, we obtain

$$T_{\gamma\gamma}^{Jp} = V_{\gamma\gamma}^{Jp} + \sum_{I=1/2}^{3/2} |T_{\gamma\pi}^{IJp}|^2 (-\tan \delta_{\ell p}^I + i). \quad (3.39)$$

There are two interesting results here. The first is that the imaginary part of the partial-wave RCS amplitude is given by the isospin sum of the photoproduction amplitudes squared. In this case the sum over the isospin is equivalent to the sum over the charged states, hence, e.g., for the proton

$$\text{Im } T_{\gamma p \rightarrow \gamma p}^{Jp} = \sum_{I=1/2}^{3/2} |T_{\gamma\pi}^{IJp}|^2 = |T_{\gamma p \rightarrow \pi^0 p}^{Jp}|^2 + |T_{\gamma p \rightarrow \pi^+ n}^{Jp}|^2. \quad (3.40)$$

The second result concerns the  $\Delta(1232)$  resonance, which is the only resonance occurring between the one- and two-pion production thresholds. Recall that, in the  $\pi N$  scattering, this resonance occurs in the  $P_{33}$  partial wave (i.e.,  $I = 3/2 = J$ ,  $\ell = 1$ ,  $p = +$ ). The position,  $M_\Delta$ , of such an elastic resonance is identified with the phase-shift crossing  $90^\circ$ . This means the tangent terms in Eq. (3.39) blow up and can only be canceled by a singularity in  $V_{\gamma\gamma}$ . Near the resonance position the  $K$ -matrix takes the form

$$K^{P_{33}} \approx \frac{M_\Delta \Gamma_\Delta}{k(s - M_\Delta^2)}, \quad (3.41)$$

where  $\Gamma_\Delta$  is the resonance width, and hence the cancellation is achieved when

$$\lim_{s \rightarrow M_\Delta^2} [(s - M_\Delta)V_{\gamma\gamma}^{3/2+}] = M_\Delta \Gamma_\Delta \lim_{s \rightarrow M_\Delta^2} |T_{\gamma\pi}^{P_{33}}|^2. \quad (3.42)$$

Thus, unitarity provides a stringent relation among the  $\Delta(1232)$ -resonance parameters occurring in the different processes. As a consequence, the  $\Delta(1232)$ -resonance contribution to polarizabilities is constrained too.

These results apply as well to the multipole amplitudes. In particular, the imaginary parts of the Compton multipoles, between the one- and two-pion production thresholds, are given by the pion photoproduction multipoles:

$$\text{Im } f_{EE}^{\ell\pm} = k \sum_c |E_{(\ell\pm 1)\mp}^{(c)}|^2, \quad \text{Im } f_{MM}^{\ell\pm} = k \sum_c |M_{\ell\pm}^{(c)}|^2, \quad (3.43a)$$

$$\text{Im } f_{EM}^{(\ell\pm 1)\mp} = \text{Im } f_{ME}^{\ell\pm} = \mp k \sum_c \text{Re} (E_{\ell\pm}^{(c)} M_{\ell\pm}^{(c)*}), \quad (3.43b)$$

where the sum is over the charged  $\pi N$  states, i.e:  $c = \pi^0 p$ ,  $\pi^+ n$  and  $c = \pi^0 n$ ,  $\pi^- p$  for the proton and neutron RCS, respectively. As mentioned above, an equivalent result is obtained by summing over the isospin states.

### 3.6. Expansion in Static vs. Dynamic Polarizabilities

The celebrated LET for RCS [136–138] can be extended to include higher-order terms, parametrized in terms of polarizabilities [1]. It is customary to separate out the Born contribution by writing

$$T = T^{\text{Born}} + \bar{T}, \quad (3.44)$$

such that  $T^{\text{Born}}$  is the Born contribution specified in Appendix A. In the low-energy limit, it yields the classic LET. The rest (non-Born),  $\bar{T}$ , is expanded in powers of energy with coefficients given by *static* polarizabilities. For example, the LEX of the non-Born part of the 6 invariant amplitudes of the decomposition (3.27) goes as (in the Breit frame):

$$\begin{aligned} \alpha \bar{A}_1(\omega_B, t) &= \omega_B^2 [\alpha_{E1} + \beta_{M1} + \omega_B^2 (\alpha_{E1\nu} + \beta_{M1\nu})] + \frac{1}{2}t(\beta_{M1} + \omega_B^2 \beta_{M1\nu}) \\ &\quad + \omega_B^4 \frac{1}{12}(\alpha_{E2} + \beta_{M2}) + \frac{1}{2}t(4\omega_B^2 + t) \frac{1}{12}\beta_{M2} + O(\omega_B^6), \\ \alpha \bar{A}_2(\omega_B, t) &= -\omega_B^2 (\beta_{M1} + \omega_B^2 \beta_{M1\nu}) + \omega_B^4 \frac{1}{12}(\alpha_{E2} - \beta_{M2}) - t\omega_B^2 \frac{1}{12}\beta_{M2} + O(\omega_B^6), \\ \alpha \bar{A}_3(\omega_B, t) &= -\omega_B^3 [\gamma_{E1E1} + \gamma_{E1M2} + z(\gamma_{M1E2} + \gamma_{M1M1})] + O(\omega_B^5), \\ \alpha \bar{A}_4(\omega_B, t) &= \omega_B^3 (\gamma_{M1E2} - \gamma_{M1M1}) + O(\omega_B^5), \\ \alpha \bar{A}_5(\omega_B, t) &= \omega_B^3 \gamma_{M1M1} + O(\omega_B^5), \\ \alpha \bar{A}_6(\omega_B, t) &= \omega_B^3 \gamma_{E1M2} + O(\omega_B^5). \end{aligned} \quad (3.45)$$

Certainly, the convergence radius of such a Taylor expansion is limited by the first singularity, which in the nucleon case is set by the pion-production branch cut (neglecting the small effects from radiative corrections). An expansion which extends beyond the pion-production threshold is the multipole expansion. The relation between the two expansions (i.e., polarizability vs. multipole) is as follows.

One can divide out the Born contribution in the multipole amplitudes,  $f = f^{\text{Born}} + \bar{f}$ . The non-Born part of the multipoles is then used to define the *dynamic* polarizabilities as [140]:

$$\begin{pmatrix} \alpha_{E\ell}(\omega) \\ \beta_{M\ell}(\omega) \end{pmatrix} = \frac{[\ell(2\ell-1)!!]^2}{\omega^{2\ell}} \left[ (\ell+1) \bar{f}_{EE}^{\ell+}(\omega) + \ell \bar{f}_{EE}^{\ell-}(\omega) \right], \quad (3.46a)$$

$$\gamma_{M\ell M\ell}^{EE\ell}(\omega) = \frac{2\ell-1}{\omega^{2\ell+1}} \left[ \bar{f}_{EE}^{\ell+}(\omega) - \bar{f}_{EE}^{\ell-}(\omega) \right], \quad (3.46b)$$

$$\gamma_{M\ell E(\ell+1)}^{E\ell M(\ell+1)}(\omega) = \frac{2^{2-\ell}(2\ell+1)!!}{\omega^{2\ell+1}} \bar{f}_{EM}^{\ell+}(\omega). \quad (3.46c)$$

Given that the low-energy behavior of the non-Born part of multipoles goes as

$$f_{EE}^{\ell\pm} \sim \omega^{2\ell}, \quad f_{EM}^{\ell+} \sim \omega^{2\ell+1}, \quad (3.47)$$

the low-energy limit of (3.46a) and (3.46c) is straightforward and corresponds with the static polarizabilities. The limit of (3.46b) needs more care, but the matching to the static polarizabilities is possible as well [54]. As an illustration, Fig. 3.3 shows the plots of the scalar dynamical polarizabilities of the proton from Ref. [54].

### 3.7. Polarized Observables

Besides the unpolarized differential cross section, given by Eq. (3.9), and the linearly-polarized photon beam asymmetry  $\Sigma_3$ , Eq. (3.16), there is a number of observables that depend on polarization of the (nucleon) target. Here we only consider the case when the polarizations of the final particles (scattered photon and recoiled nucleon) are not observed.

We consider the photon, along the  $z$ -axis, with a linear polarization and  $P_T^\gamma$  at the angle  $\phi$  with respect to the scattering plane  $xz$ , and the right-handed circular polarization  $P_R^\gamma$ . The degree of the target polarization along the  $x$ -,  $y$ -,  $z$ -direction is denoted as  $P_x$ ,  $P_y$ ,  $P_z$  respectively. In this case the polarized cross-section element is given by

$$\begin{aligned} d\sigma &= d\sigma^{\text{unpol.}} [1 + P_T^\gamma \Sigma_3 \cos 2\phi + P_x (P_R^\gamma \Sigma_{2x} + P_T^\gamma \Sigma_{1x} \sin 2\phi) \\ &\quad + P_y (\Sigma_y + P_T^\gamma \Sigma_{3y} \cos 2\phi) + P_z (P_R^\gamma \Sigma_{2z} + P_T^\gamma \Sigma_{1z} \sin 2\phi)], \end{aligned} \quad (3.48)$$

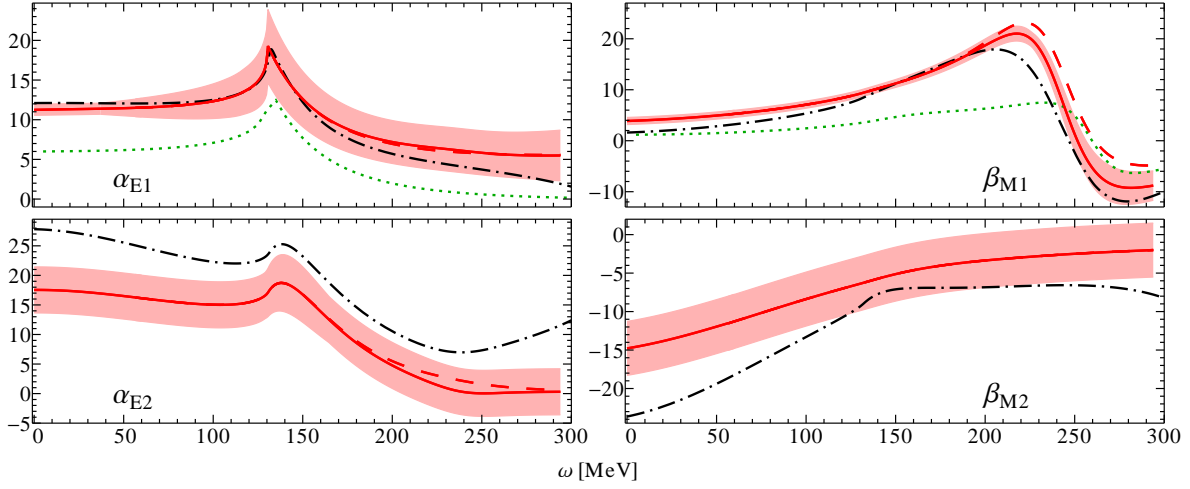


Figure 3.3: The scalar dipole and quadrupole dynamical polarisabilities of the *proton*, in units of  $10^{-4}\text{fm}^3$  and  $10^{-4}\text{fm}^5$ , respectively. The curves are the results of the  $B\chi\text{PT}$  calculation of Lensky et al. [54] (red bands), compared with the results of the DR calculation of Hildebrandt et al. [118] (black dot-dashed) and with the results of Aleksejevs and Barkanova [141, 142] (green dotted, not shown for the quadrupole polarisabilities).

where  $d\sigma^{\text{unpol.}}$  stands for the unpolarized cross section and  $\Sigma$ 's denote the various asymmetries. This notation for asymmetries is motivated by Babusci et al. [96]. The conversion to the standard notation adopted in meson photoproduction (see, e.g., Appendix A of Worden [143]) is as follows:

$$\Sigma_3 = -\Sigma, \quad \Sigma_{2x} = F, \quad \Sigma_{1x} = -H, \quad \Sigma_y = T, \quad \Sigma_{3y} = -P, \quad \Sigma_{2z} = -E, \quad \Sigma_{1z} = G. \quad (3.49)$$

Similar to Eq. (3.16) for  $\Sigma_3$ , we may express these asymmetries in terms of the specific polarized cross sections and in terms of the helicity amplitudes:<sup>5</sup>

$$\frac{d\sigma}{d\Omega_{cm}} \Sigma_{2x} \equiv \frac{1}{2} \left( \frac{d\sigma_x^R}{d\Omega_{cm}} - \frac{d\sigma_x^L}{d\Omega_{cm}} \right) = \text{Re}[\Phi_4(\Phi_1 - \Phi_5)^* - (\Phi_2 + \Phi_6)\Phi_3^*], \quad (3.50a)$$

$$\frac{d\sigma}{d\Omega_{cm}} \Sigma_{2z} \equiv \frac{1}{2} \left( \frac{d\sigma_z^R}{d\Omega_{cm}} - \frac{d\sigma_z^L}{d\Omega_{cm}} \right) = -\frac{1}{2} (|\Phi_1|^2 + |\Phi_2|^2 - |\Phi_5|^2 - |\Phi_6|^2), \quad (3.50b)$$

$$\frac{d\sigma}{d\Omega_{cm}} \Sigma_{1x} \equiv \frac{1}{2} \left( \frac{d\sigma_x^{\pi/4}}{d\Omega_{cm}} - \frac{d\sigma_x^{-\pi/4}}{d\Omega_{cm}} \right) = \text{Im}[\Phi_1^*\Phi_2 + \Phi_5^*\Phi_6], \quad (3.50c)$$

$$\frac{d\sigma}{d\Omega_{cm}} \Sigma_{1z} \equiv \frac{1}{2} \left( \frac{d\sigma_z^{\pi/4}}{d\Omega_{cm}} - \frac{d\sigma_z^{-\pi/4}}{d\Omega_{cm}} \right) = -\text{Im}[\Phi_3(\Phi_1 - \Phi_5)^* - (\Phi_2 + \Phi_6)\Phi_4^*], \quad (3.50d)$$

$$\frac{d\sigma}{d\Omega_{cm}} \Sigma_y \equiv \frac{1}{2} \left( \frac{d\sigma_y}{d\Omega_{cm}} - \frac{d\sigma_{-y}}{d\Omega_{cm}} \right) = -\text{Im}[\Phi_4(\Phi_1 + \Phi_5)^* + (\Phi_2 - \Phi_6)\Phi_3^*], \quad (3.50e)$$

$$\frac{d\sigma}{d\Omega_{cm}} \Sigma_{3y} \equiv \frac{1}{2} \left( \frac{d\sigma_y^0}{d\Omega_{cm}} - \frac{d\sigma_y^{\pi/2}}{d\Omega_{cm}} \right) = \frac{d\sigma}{d\Omega_{cm}} \Sigma_3 + \text{Im}[\Phi_1^*\Phi_2 + 2\Phi_3^*\Phi_4 - \Phi_5^*\Phi_6]. \quad (3.50f)$$

The superscript on  $\sigma$  indicates here the photon polarization: right ( $R$ ), left ( $L$ ) for the circular polarization, or the value of  $\phi$  for the linear polarization. The subscript indicates the nucleon spin polarization. The expressions in terms of the helicity amplitudes assume parity conservation. Terms proportional to the imaginary part are negligible below the pion-production threshold (because the imaginary part of the amplitudes is suppressed by an  $\alpha$ ).

Some of the polarized observables have been measured for the proton RCS, which brings us to the following section.

<sup>5</sup>Here it is important that, in the center-of-mass frame, the nucleon travels in the  $-z$  direction. Hence, its polarization along  $z$ -axis corresponds with helicity  $-1/2$ , and so on.

## 4. Compton Scattering Experiments

### 4.1. Low-Energy Expansion of CS Observables

The CS processes remain to be the only method of accessing the nucleon polarizabilities experimentally. The nucleon probed by long-wave photons reveals its structure in the manner of a multipole expansion. At first, one distinguishes the electric charge and magnetic dipole moment, contributions which comprise the low-energy theorem for CS [137, 138]. Further terms (in multipole or energy expansion) can be described in terms of polarizabilities, of which  $\alpha_{E1}$  and  $\beta_{M1}$  play the leading role. For instance, the low-energy expansion (LEX) of the unpolarized CS cross section, truncated at  $O(\nu^2)$ , is given by:

$$\frac{d\sigma}{d\Omega_L} = \frac{d\sigma^{\text{Born}}}{d\Omega_L} - \nu\nu' \left(\frac{\nu'}{\nu}\right)^2 \frac{2\pi\alpha}{M} \left[ (\alpha_{E1} + \beta_{M1})(1+z)^2 + (\alpha_{E1} - \beta_{M1})(1-z)^2 \right], \quad (4.1)$$

where  $z = \cos \vartheta$ , and  $\nu$  ( $\nu'$ ) is the energy of the incoming (scattered) photon.

The simplicity of the formalism is appealing. However, the region of its applicability is unclear a priori. It is only clear that the convergence radius of such a LEX is limited by the nearest singularity, which in this case is at pion production threshold (neglecting the small e.m. corrections). This is illustrated by the dynamical polarizabilities in Fig. 3.3. Their LEX begins with the static value, which is the value at zero energy ( $\omega = 0$ ). Clearly, approximating the dynamic polarizabilities by a constant (the static value) only works well at energies far below the pion-production threshold ( $\omega \ll m_\pi$ ).

Further insight can be obtained by comparing the LEX of the cross section with experimental data and the results of calculations that extend beyond the pion threshold. Figure 4.1 shows a calculation of the Born and LEX cross sections for CS on the proton at fixed angle and function of beam energy [12]. There is increased sensitivity to the polarizabilities at higher incident energies. However, at higher energies there is also increased sensitivity to terms of order  $O(\nu^3)$  and higher. The importance of the higher order terms is indicated by the dashed curve, which is a dispersion model calculation valid to all orders in  $\nu$ , albeit with unclear model-dependencies. One sees that above 100 MeV, the lowest-order LEX is not adequate. The higher-order terms may extend its applicability, but will depend on the spin polarizabilities and other, higher-order polarizabilities.

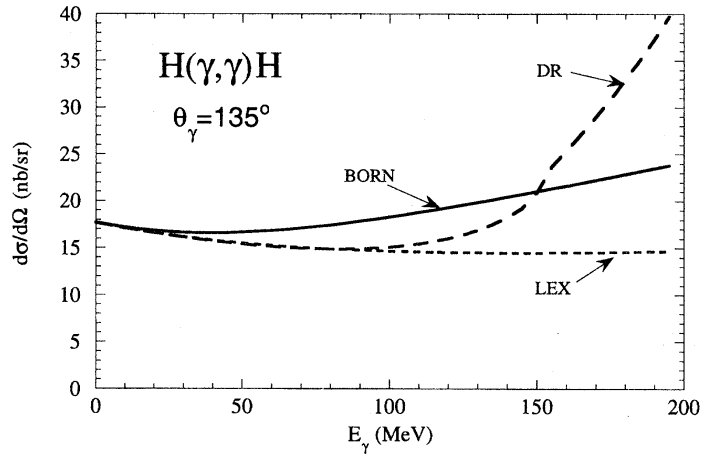


Figure 4.1: CS cross sections calculated in the Born approximation (solid), the leading-order LEX (dotted) and a dispersion model calculation (dashed).

Nonetheless, the LEX is instructive for understanding how the polarizabilities affect the observables. One can see, for example, that at forward angles the polarizability effect enters as  $\alpha_{E1} + \beta_{M1}$ , while at the backward angles as  $\alpha_{E1} - \beta_{M1}$ . Hence one can use the angular distribution to disentangle  $\alpha_{E1}$  and  $\beta_{M1}$ .

The leading LEX expressions for CS with linearly polarized photons are obtained by Maximon [144] who finds [rearranging his Eqs. (19) and (20)]:

$$\left( \frac{d\sigma_{\perp}}{d\Omega_L} - \frac{d\sigma_{\perp}^{\text{Born}}}{d\Omega_L} \right) - \left( \frac{d\sigma_{\parallel}}{d\Omega_L} - \frac{d\sigma_{\parallel}^{\text{Born}}}{d\Omega_L} \right) = -\frac{8\pi\alpha}{M} \left( \frac{\nu'}{\nu} \right)^2 \nu\nu' \alpha_{E1} \sin^2 \vartheta \quad (4.2a)$$

$$\cos^2 \vartheta \left( \frac{d\sigma_{\perp}}{d\Omega_L} - \frac{d\sigma_{\perp}^{\text{Born}}}{d\Omega_L} \right) - \left( \frac{d\sigma_{\parallel}}{d\Omega_L} - \frac{d\sigma_{\parallel}^{\text{Born}}}{d\Omega_L} \right) = \frac{8\pi\alpha}{M} \left( \frac{\nu'}{\nu} \right)^2 \nu\nu' \beta_{M1} \cos \vartheta \sin^2 \vartheta \quad (4.2b)$$

where  $d\sigma_{\perp}/d\Omega_L$  and  $d\sigma_{\parallel}/d\Omega_L$  are the differential cross sections for CS perpendicular and parallel to the plane of incident photon polarization. By taking weighted differences of  $\sigma_{\perp}$  and  $\sigma_{\parallel}$ , it is possible to measure  $\beta_{M1}$



Table 4.1: Theoretical frameworks used in the analysis of CS cross sections and asymmetries on proton and nuclear targets.

Target	Energy range	Theoretical model	Reference
Proton	$2\pi$ threshold	Fixed- $t$ dispersion calculation	Drechsel et al. [86]
Proton	$\Delta(1232)$ region	Chiral Lagrangian	Gasparyan et al. [91]
Proton	$\Delta(1232)$ region	HB $\chi$ PT with $\Delta(1232)$	McGovern et al. [51]
Proton	$\Delta(1232)$ region	B $\chi$ PT with $\Delta(1232)$	Lensky and Pascalutsa [49]
Deuteron	$\approx 130$ MeV	$\chi$ EFT	Griesshammer et al. [65]
$^3\text{He}$	$\approx 130$ MeV	$\chi$ EFT	Shukla et al. [150]

separately from  $\alpha_{E1}$ . Hence, in separating the electric and magnetic polarizabilities the beam polarization can serve as an alternative to the angular distribution.

The issue here is that the cross section differences in parentheses on the left sides of the above equations are relatively small, at the 10% level compared to the cross sections. To measure polarizabilities with a precision of  $\approx 10\%$  requires measurement of the absolute cross sections  $\sigma_{\perp}$  and  $\sigma_{\parallel}$  with uncertainties of  $\approx 1\%$ . This is a severe challenge for CS experiments, both in statistics and systematic errors.

It is much easier in this respect to measure the linear polarization asymmetry,

$$\Sigma_3 = \frac{d\sigma_{\parallel} - d\sigma_{\perp}}{d\sigma_{\parallel} + d\sigma_{\perp}}. \quad (4.3)$$

The asymmetry measurements do not critically depend on knowing the incident photon flux, target thickness, and photon and recoil proton detection efficiencies. To  $O(\nu^2)$  this asymmetry depends only on  $\beta_{M1}$  and is independent of  $\alpha_{E1}$  [36]:

$$\Sigma_3 = \Sigma_3^{\text{Born}} - \frac{4M\omega_B^2 \cos\theta_B \sin^2\theta_B}{(1 + \cos^2\theta_B)^2} \alpha^{-1} \beta_{M1} \quad (4.4)$$

where  $\omega_B$  and  $\theta_B$  are the photon energy and scattering angle in the Breit (brick-wall) frame, see Eqs. (C.1) and (C.3) for their relations to invariants. Calculations at NNLO in B $\chi$ PT indicate that the range of applicability of Eq. (4.4) is as high as 100 MeV. However, the sensitivity to  $\beta_{M1}$  in Eq. (4.4) is weak, at the order of  $\Delta\Sigma_3/\Delta\beta_{M1} \approx 0.02$ . To measure  $\beta_{M1}$  at the level of  $\pm 0.5$  (in the usual units) would require uncertainty in  $\Sigma_3$  to reach  $\pm 0.01$ . To attain this statistical precision, photon intensities at least an order of magnitude greater than those available with standard photon tagging techniques would be required.

Nevertheless, the LEX formula (4.4) paves the way for a more sophisticated analysis, awaiting the first data  $\Sigma_3$  below the pion production threshold. The LEX formula for the doubly-polarized asymmetries,  $\Sigma_{2x}$  and  $\Sigma_{2z}$  can be found in Krupina [145].

To summarize, a model-independent extraction of polarizabilities from CS observables based on LEX is nearly impossible at the existing facilities. On one hand, the sensitivity must be substantial enough for to see the signal at the given level of experimental precision, which drives the experiment to higher energy. On the other hand, at higher energies the LEX applicability is compromised. Therefore, although the LEX gives a valuable insight on the sensitivity of observables, it has thus far been impractical in quantitative extractions.

A more practical and common approach is to extract polarizabilities by fitting the CS data using a systematic theoretical framework, such as  $\chi$ PT [48–52, 65, 146, 147] or fixed- $t$  dispersion relations (DRs) [85–87, 148, 149]. Table 4.1 presents a listing of several calculations that have been or could be used for fitting cross section and asymmetry data from pion threshold up to the  $\Delta(1232)$  region. By fitting data with several theoretical models, it is possible to obtain an estimate for the model dependence of the result. This was, for example, the approach taken by Martel et al. [38] for their analysis of double-polarized CS in the  $\Delta(1232)$  region.<sup>6</sup>

<sup>6</sup>A limitation in fitting large numbers of data points with a fitting program such as MINUIT is that many recursive calls are made to the subroutine calculating the observable. If the calculation of the observable is based upon numerical integrations, such as the fixed- $t$



## 4.2. Determination of Scalar Polarizabilities

### 4.2.1. Proton

The first CS measurement of the proton polarizabilities using a tagged photon beam was by Federspiel et al. [10] at the University of Illinois MUSL-2 microtron. Experiments prior to this used bremsstrahlung beams, and were limited by systematic errors due to uncertainties in the incident photon energy. The most recent published results for CS on the proton are by the LEGS group [13], and the TAPS at MAMI setup [17], both in 2001. Their results for  $\alpha_{E1}$  and  $\beta_{M1}$  are in agreement.

After publication of the LEGS and TAPS results, activity in this area slowed. Then in 2010-2012 new  $\chi$ PT calculations of CS [49, 65] showed that  $\beta_{M1}$  is larger than the PDG average of that time,  $\beta_{M1}^{(p)} = (1.9 \pm 0.5) \times 10^{-4} \text{ fm}^3$  [151], by +1 to +3 of the standard deviations. In 2014 the CS global analysis of McGovern et al. [51] was included in the PDG average, and the current (2014) PDG values are [71]:

$$\alpha_{E1}^{(p)} = (11.2 \pm 0.4) \times 10^{-4} \text{ fm}^3, \quad \beta_{M1}^{(p)} = (2.5 \mp 0.4) \times 10^{-4} \text{ fm}^3. \quad (4.7)$$

Nevertheless, the uncertainty quoted in the PDG average should be taken with a grain of salt because data sets are not treated consistently. Results from the analysis of specific experiments are averaged with results from global analyses of CS data. The summary plots in Sect. 7 show the real state of affairs for  $\alpha_{E1}$  and  $\beta_{M1}$  of the proton, cf. Figs. 7.1 and 7.3 (left panel). It is not as certain as the PDG average portrays it. There is certainly a room for improvement.

The thrust of new proton polarizability measurements is to use linearly polarization as an analyzer to measure  $\alpha_{E1}$  and  $\beta_{M1}$  separately, and independently of the Baldin sum rule value for  $\alpha_{E1} + \beta_{M1}$ . Programs to measure the proton polarizabilities with linearly polarized photons are currently underway at MAMI-Mainz and HIGS.

Preliminary data [35] with linearly polarized incident photons have been taken by the A2 collaboration at the tagged photon facility [152] at the Mainz microtron MAMI [153]. In this experiment a diamond radiator is used to produce linearly polarized coherent bremsstrahlung [154] with a peak polarization of approximately 75%. The target is a 10 cm long liquid hydrogen target, and Compton scattered photons are detected in the Crystal Ball [155] and TAPS detectors [156], both of which are outfitted with charged particle identification systems [157]. The Crystal Ball, TAPS, and the charged particle system internal to the Crystal Ball (the PID scintillator array and MWPC), are shown in Fig. 4.2. The solid angle coverage for Compton-scattered photons is approximately 97% of  $4\pi$ . The incident photon energies for the measurement range from 80 to 140 MeV. Recoil

---

DR code of Drechsel et al. [86], then execution times can stretch into days. Martel et al. [38] handled this problem assuming a linear dependence of the observable on the polarizabilities:

$$\mathcal{O}_i(\{P\}) = \mathcal{O}_i(\{P_0\}) + \sum_{j=1}^6 \frac{\partial \mathcal{O}_i(\{P_0\})}{\partial P_j} (P_j - P_{0j}), \quad (4.5)$$

where  $\mathcal{O}_i$  is the observable,  $\{P\}$  is the set of six polarizabilities (two scalar and four spin polarizabilities), and  $\{P_0\}$  is the set of starting "guesses" for the polarizabilities. The standard expression for  $\chi^2$  is given by:

$$\chi^2 = \sum_{i=1}^{N_{\text{data}}} \left( \frac{\mathcal{O}_i^{\text{data}} - \mathcal{O}_i(\{P\})}{\sigma_i} \right)^2 + \sum_{j=1}^6 \left( \frac{P_j^{\text{data}} - P_j}{\sigma_{P_j}} \right)^2, \quad (4.6)$$

where the second term in  $\chi^2$  allows for the possibility of introducing constraints on the polarizabilities (e.g., the sum-rule constraints on  $\alpha_{E1} + \beta_{M1}$  and  $\gamma_0$ ). Substituting Eqs. (4.5) into (4.6), and setting  $\partial \chi^2 / \partial P_j = 0$  leads to a linear equation,  $C_i = D_{ij} P_j$ , with

$$C_i = \frac{P_i^{\text{data}}}{\sigma_{P_i}^2} + \sum_{j=1}^{N_{\text{data}}} \frac{1}{\sigma_j^2} \left[ \mathcal{O}_j^{\text{data}} - \mathcal{O}_j(\{P_0\}) + \sum_{k=1}^6 \frac{\partial \mathcal{O}_j(\{P_0\})}{\partial P_k} P_{0k} \right] \frac{\partial \mathcal{O}_j(\{P_0\})}{\partial P_i}, \quad i = 1, \dots, 6,$$

$$D_{ij} = \frac{\delta_{ij}}{\sigma_{P_i}^2} + \sum_{k=1}^{N_{\text{data}}} \frac{1}{\sigma_k^2} \frac{\partial \mathcal{O}_k(\{P_0\})}{\partial P_i} \frac{\partial \mathcal{O}_k(\{P_0\})}{\partial P_j}, \quad i, j = 1, \dots, 6.$$

One can solve it for  $\{P\}$ , as  $P = D^{-1}C$ . After the first iteration the substitution  $\{P\} \rightarrow \{P_0\}$  is made,  $\mathcal{O}_i(\{P_0\})$ ,  $\partial \mathcal{O}_i(\{P_0\}) / \partial P_j$  and  $\{P\}$  are reevaluated, and the fit repeated until the set  $\{P\}$  differs from  $\{P_0\}$  by less than one standard deviation. It was found that this methodology is very efficient in fitting large data sets with computationally intensive codes.

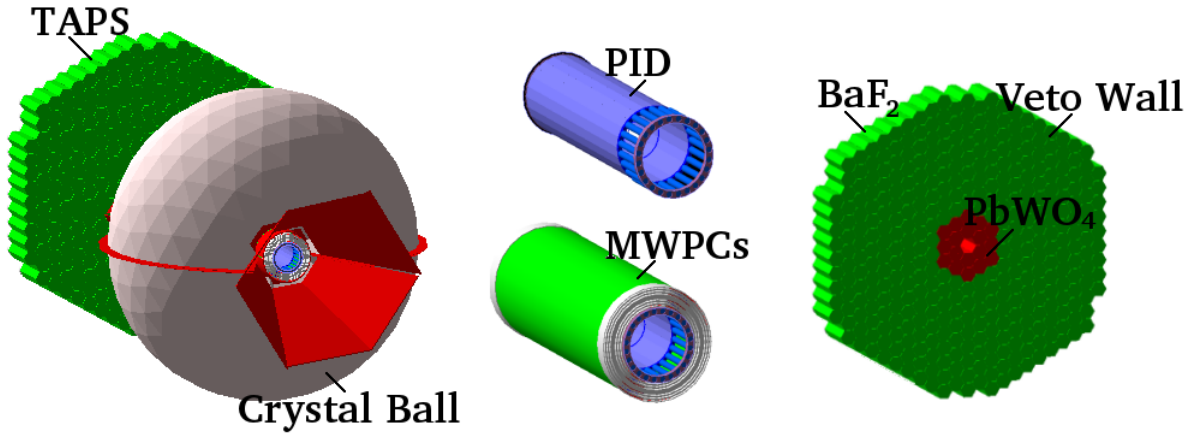


Figure 4.2: The Crystal Ball and TAPS detectors at the Mainz microtron MAMI.

proton detection is not required because the backgrounds are sufficiently low. The missing mass distribution, shown in Fig. 4.3, reveals there is relatively little background in the measurement. The goals for this experiment are to obtain precision measurements of the cross sections  $d\sigma_{\perp}$  and  $d\sigma_{\parallel}$ , the asymmetry  $\Sigma_3$ , and the unpolarized cross section by running on an amorphous photon radiator.

At HIGS [39] there are plans [40] to take CS data on the proton with linearly polarized photons in 2016. The incident photon beam at HIGS is exceptionally well suited for a LEX based CS analysis for  $\alpha_{E1}$  and  $\beta_{M1}$ ; energies up to 100 MeV are available, the beam energy is monochromatic with a spread of  $\approx 4.5\%$ , photon intensities on the target are  $\approx 10^7 \gamma/s$ , and the linear polarization is approximately 100% [158]. Figure 4.4 shows the HINDA NaI array that has been developed for CS experiments. Each module has a 25.4 cm in diameter and 30.5 cm long NaI core, surrounded by active NaI shields that are 7.5 cm thick and 30.5 cm long.

#### 4.2.2. Neutron

As a “free” neutron target does not exist, there are no truly model-independent means to determine the neutron’s polarizabilities. Obtaining neutron polarizabilities from the analysis of deuteron CS data requires accurate effective-field theory calculations. The favored approach is to use elastic scattering data, not quasi-free  $d(\gamma, \gamma'n)p$  data, because (i) the elastic process is theoretically less complicated than the quasi-free scattering, and treatable through effective-field theory calculations, and (ii) elastic scattering has a larger cross section and greater sensitivity to the polarizabilities than the quasi-free process. The latter point can be understood by noting that for CS on a free neutron there is no Thomson term in the scattering amplitude, because the neutron is neutral, and the polarizability effect goes as  $O(\nu^4)$ . For elastic scattering there is a Thomson term, because the deuteron is charged, and the polarizability effect goes as  $O(\nu^2)$ . The disadvantage of elastic scattering is that it places a premium on the utilization of large NaI detectors with sufficient energy resolution to resolve elastic and inelastic scattering. Furthermore, the elastic scattering is sensitive to the isoscalar polarizabilities, and the proton contribution must be subtracted.

Until recently there has been a paucity of CS data on the deuteron. For example, the analysis of Griebhammer et al. [65] was based on three data sets with a total of 37 data points. The focus of new studies has been to stage experiments that can obtain relatively high statistics with wide kinematic coverage, utilize large NaI detectors for optimal energy resolution, and to use targets with  $A > 2$ . In this section recent progress in this area is outlined.

New data from Lund has recently been published for elastic CS on the deuteron [15], nearly doubling the effective number of world data points and extending the energy range by 20 MeV to higher energies. The large-volume, segmented NaI(Tl) detectors, BUNI, CATS, and DIANA were used to detect Compton-scattered photons in the experiment. These detectors are composed of a NaI(Tl) core surrounded by optically isolated, annular NaI(Tl) segments. The cores of the BUNI and CATS detectors each measure 26.7 cm in diameter, while the core of the DIANA detector measures 48.0 cm. The depth of all three detectors is greater than 20 radiation lengths. The annular segments are 11 cm thick on the BUNI and CATS detectors and 4 cm thick on the DIANA detector. Figures 7.2 and 7.3 (right panel) show the present state of affairs for  $\alpha_{E1}$  and  $\beta_{M1}$  of the neutron.

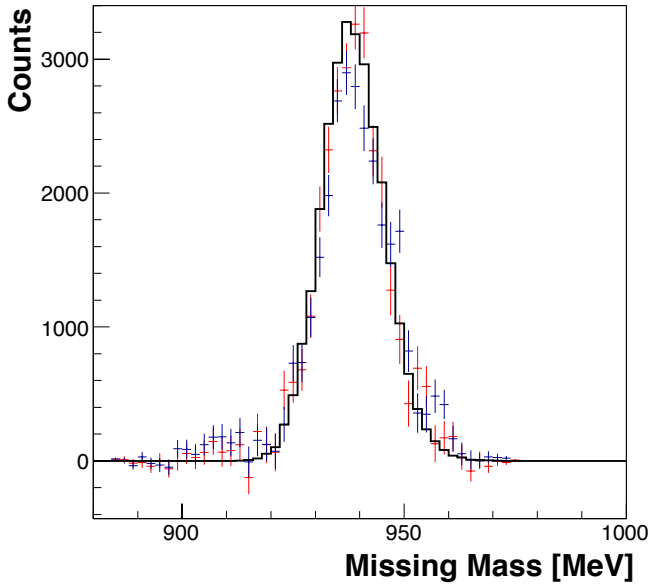


Figure 4.3: Missing mass distribution for the Mainz proton scalar polarizability measurement for incident photon energies from 120 to 140 MeV, and angular range  $60^\circ < \vartheta < 150^\circ$  [35]. Data with parallel photon polarization is blue, and perpendicular polarization is red. The black curve represents the simulated distribution. Plot courtesy of Vahe Sokhoyan.

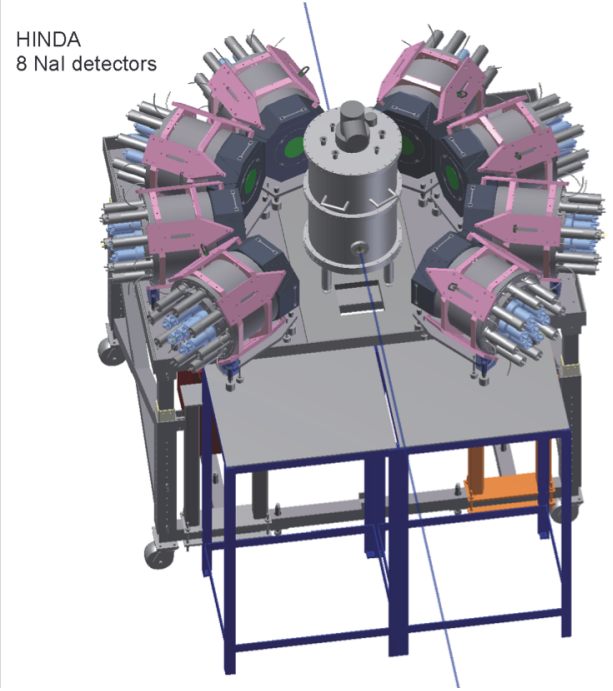


Figure 4.4: Diagram of the HINDA NaI array at HIGS.

There are compelling reasons to consider CS on  $Z > 1$  nuclei as an attractive route to the neutron polarizabilities; the Thomson cross section goes at  $Z^2$ , and there is a better ratio of elastic to incoherent scattering for  $A > 2$ . As a test of the effective interaction theories used to analyze the data, it is also important to demonstrate that polarizabilities obtained from deuterium are in agreement with results from other nuclei. Figure 4.5 shows the results of a NLO  $\chi$ EFT calculation without  $\Delta(1232)$  degrees of freedom at 60 MeV (upper panel) and 120 MeV (lower panel) for CS on  $^3\text{He}$ . The curves show appreciable sensitivity to the neutron polarizabilities, especially at the higher energy.

There are plans [159] to measure elastic CS on  $^3\text{He}$  and  $^4\text{He}$  with an active, gaseous helium target using the Crystal Ball and TAPS detectors at the Mainz microtron MAMI. The operating principle of the target is that ionizing particles produce UV scintillation light in the helium, and by the addition of small amounts of  $\text{N}_2$  as a wavelength shifter, and a photo-detector coupled to the target cell, the target can operate as a detector. Elastic scattering is separated from incoherent processes by detecting the recoil helium nucleus in coincidence with the Compton-scattered photon. Development of this target is in progress, and test runs are anticipated in 2016.

#### 4.3. Determination of Proton Spin Polarizabilities

Compared to the situation for the proton scalar polarizabilities, relatively little is known experimentally about the spin polarizabilities. Prior to the advent of single-polarized and double-polarized CS asymmetry measurements, only two linear combinations of the polarizabilities were known. One combination is the forward spin polarizability:

$$\gamma_0 = -\gamma_{E1E1} - \gamma_{E1M2} - \gamma_{M1M1} - \gamma_{M1E2}, \quad (4.8)$$

fixed by the GTT sum rule (5.24). The results of the GTT sum rule evaluation are summarized in Table 5.2. The other combination is the backward spin polarizability  $\gamma_\pi$ :

$$\gamma_\pi = -\gamma_{E1E1} - \gamma_{E1M2} + \gamma_{M1M1} + \gamma_{M1E2}. \quad (4.9)$$

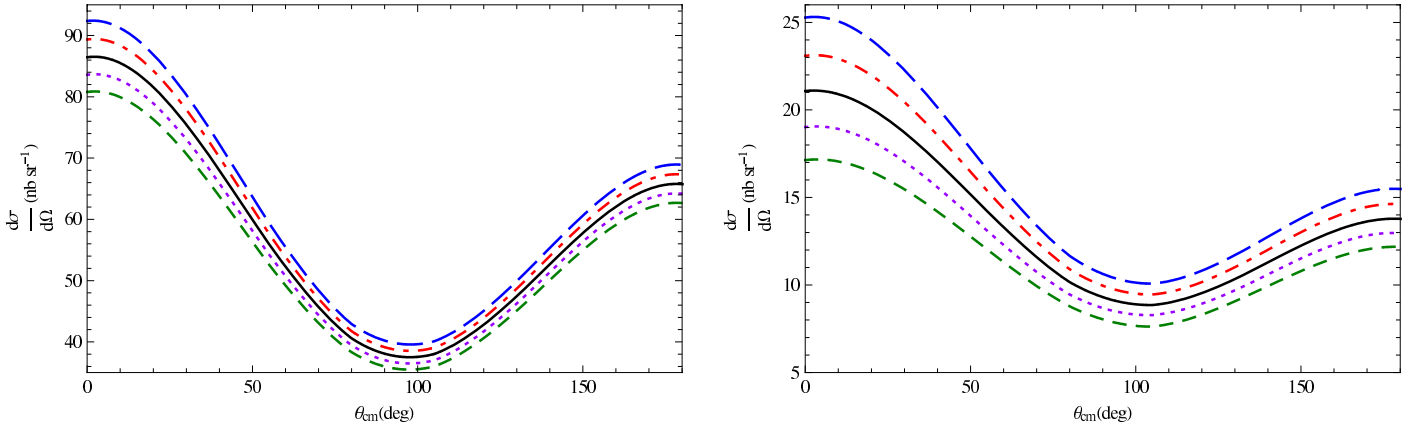


Figure 4.5: Sensitivity of the differential cross sections for CS on  $^3\text{He}$  in the c.m. frame at NLO in  $\chi\text{EFT}$  without explicit  $\Delta(1232)$  at 60 MeV (left panel) and 120 MeV (right panel). Solid (black) curve: central value  $\alpha_{E1}^n = 12.2$ ; long-dashed (blue):  $\alpha_{E1}^n - 4$ ; dot-dashed (red):  $\alpha_{E1}^n - 2$ ; dotted (magenta):  $\alpha_{E1}^n + 2$ ; dashed (green):  $\alpha_{E1}^n + 4$ ; in units of  $10^{-4} \text{ fm}^3$ .

Figure 7.5 summarizes the results for the backward spin polarizability of the proton.

The forward (backward) spin polarizability, living up to its name, appears in the spin-dependent CS amplitude at forward (backward) kinematics. More specifically, in both kinematics the CS amplitude splits into a spin-independent and spin-dependent part, i.e.:

$$\frac{1}{8\pi M} T(\nu, \vartheta = 0) = f(\nu) \boldsymbol{\varepsilon}'^* \cdot \boldsymbol{\varepsilon} + g(\nu) i \boldsymbol{\sigma} \cdot \boldsymbol{\varepsilon}'^* \times \boldsymbol{\varepsilon}, \quad (4.10a)$$

$$\frac{1}{8\pi M} T(\nu, \vartheta = \pi) = \frac{1}{\sqrt{1 + 2\nu/M}} \left[ \tilde{f}(\nu) \boldsymbol{\varepsilon}'^* \cdot \boldsymbol{\varepsilon} + \tilde{g}(\nu) i \boldsymbol{\sigma} \cdot \boldsymbol{\varepsilon}'^* \times \boldsymbol{\varepsilon} \right], \quad (4.10b)$$

and the low-energy expansion for the scalar amplitudes goes as follows [96]:

$$f(\nu) = -\frac{Z^2 \alpha}{M} + (\alpha_{E1} + \beta_{M1}) \nu^2 + O(\nu^4), \quad (4.11a)$$

$$g(\nu) = -\frac{\alpha \kappa^2}{2M^2} \nu + \gamma_0 \nu^3 + O(\nu^5), \quad (4.11b)$$

$$\tilde{f}(\nu) = \left(1 + \frac{\nu}{M}\right) \left[ -\frac{Z^2 \alpha}{M} + (\alpha_{E1} - \beta_{M1}) \frac{\nu^2}{1 + 2\nu/M} + \dots \right], \quad (4.11c)$$

$$\tilde{g}(\nu) = \left[ -\frac{1}{2} \kappa^2 + (Z + \kappa)^2 \right] \frac{\alpha \nu}{M^2} + \gamma_\pi \frac{\nu^3}{1 + 2\nu/M} + \dots \quad (4.11d)$$

Hence,  $\gamma_0$  and  $\gamma_\pi$  appear at  $O(\nu^3)$  in the LEX of the spin-flip amplitude at, respectively, the forward and backward scattering angle.

Figure 4.6 shows the sensitivity of backward angle CS cross sections in the  $\Delta(1232)$  region to  $\gamma_\pi$ . The most widely accepted value for  $\gamma_\pi$  is actually an average of three measurements at MAMI performed with different detector configurations: TAPS [17], LARA [18, 19], and SENECA [20]. All three of the measurements agree within their statistical and systematic errors, and the average value is [20]:

$$\gamma_\pi = (8.0 \pm 1.8) \times 10^{-4} \text{ fm}^4, \quad (4.12)$$

where the error includes statistical and estimated model uncertainties. Here we use the standard convention of excluding the t-channel  $\pi^0$ -pole contribution<sup>7</sup>. The latter is evaluated as (e.g., Ref. [160]):

$$\gamma_\pi^{\pi^0 \text{ pole}} = -\frac{2\alpha g_A}{(2\pi f_\pi)^2 m_{\pi^0}^2} = (-46.04 \pm 0.16) \times 10^{-4} \text{ fm}^4. \quad (4.13)$$

<sup>7</sup>In the literature the result with the  $\pi^0$ -pole excluded is sometimes referred to as  $\bar{\gamma}_\pi$  (see, e.g., Ref. [13]).

The  $\pi^0$ -pole contribution is also excluded from each of the spin polarizabilities:  $\gamma_{E1E1}$ ,  $\gamma_{M1M1}$ ,  $\gamma_{E1M2}$  and  $\gamma_{M1E2}$  [96]. However, this contribution cannot affect  $\gamma_0$  and other forward polarizabilities, because the  $\pi^0$ -pole diagram vanishes in the forward direction.

The LEGS result [13],

$$\gamma_\pi = (18.81 \pm 2.27_{\text{stat+syst}} + [^{+2.24}_{-2.10}]_{\text{model}}) \times 10^{-4} \text{ fm}^4, \quad (4.14)$$

is in disagreement with the Mainz result, despite the good agreement between LEGS and Olmos de León et al. [17] for  $\alpha_{E1}$  and  $\beta_{M1}$ . As seen in Fig. 4.6, the main cause for this disagreement is the discrepancy between measured cross sections at backward angles at energies above pion threshold.

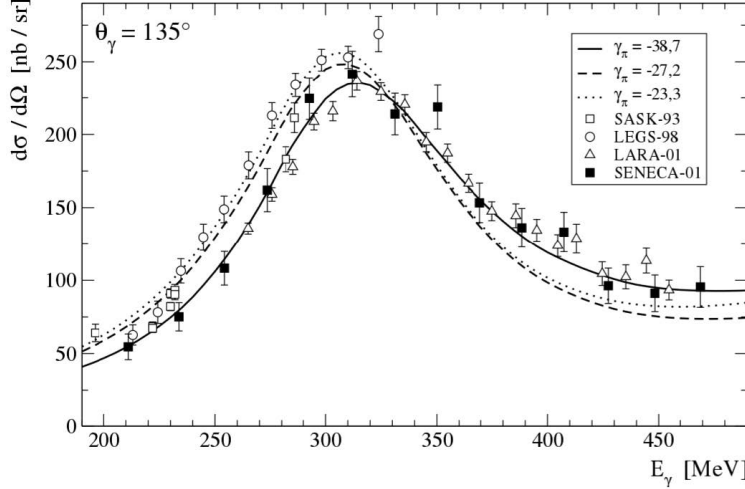


Figure 4.6: CS cross sections at  $135^\circ$  in the  $\Delta(1232)$  region. The curves correspond to different values of  $\gamma_\pi$ . Note that in this plot legend the quoted  $\gamma_\pi$  values include the t-channel  $\pi^0$ -pole contribution.

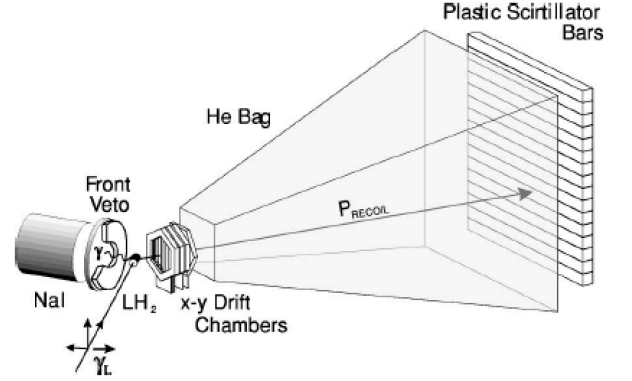


Figure 4.7: CS configuration for the LEGS detectors.

Single and double-polarized CS asymmetries in the  $\Delta(1232)$  region have sensitivity to the spin polarizabilities [87]. Measurements of this type provide essentially the only means by which the four lowest order spin polarizabilities  $\gamma_{E1E1}$ ,  $\gamma_{M1M1}$ ,  $\gamma_{E1M2}$  and  $\gamma_{M1E2}$  can be individually separated. The linear polarization asymmetry  $\Sigma_3$  in the  $\Delta(1232)$  region was measured at LEGS [13], and a new program of single and double polarized CS measurements is currently underway at MAMI [37].

#### 4.3.1. Linearly Polarized Photons

The linear polarization asymmetry,  $\Sigma_3$ , is defined in Eq. (4.3), see also Eq. (3.16). The first measurements of this asymmetry were by the LEGS collaboration [13] in the  $\Delta(1232)$  region, see Fig. 4.8. Their experimental setup, shown in Fig. 4.7, is fairly typical of CS experiments in the  $\Delta(1232)$  region, where the Compton photon is detected in a NaI detector, and the recoil proton is detected in a spectrometer arm specifically designed for recoil detection. Detecting the recoil proton is necessary to suppress background from  $\pi^0 \rightarrow \gamma\gamma$ ; the ratio of  $\pi^0$  photoproduction to CS in the  $\Delta(1232)$  region is approximately 100:1. In the LEGS measurement precision wire chambers are used to define the trajectory of the proton, and time-of-flight over 4 m and energy loss in scintillator paddles are used to establish particle type and momentum.

In the LEGS analysis two spin polarizability combinations are fit to their data:

$$\gamma_{13} = -\gamma_{E1E1} + \gamma_{E1M2} = (3.94 \pm 0.53_{\text{stat+syst}} + [^{+0.20}_{-0.18}]_{\text{model}}) \times 10^{-4} \text{ fm}^4, \quad (4.15a)$$

$$\gamma_{14} = -\gamma_{E1E1} - \gamma_{E1M2} - 2\gamma_{M1M1} = -(2.20 \pm 0.27_{\text{stat+syst}} + [^{+0.05}_{-0.09}]_{\text{model}}) \times 10^{-4} \text{ fm}^4. \quad (4.15b)$$

New data for the  $\Sigma_3$  asymmetry in the  $\Delta(1232)$  region have recently been taken by the Mainz A2 collaboration at the microtron MAMI using the Crystal Ball and TAPS detectors [161]. In this experiment  $\pi^0$  events are suppressed by making use of the hermeticity of the detector, requiring that only one neutral and one charged



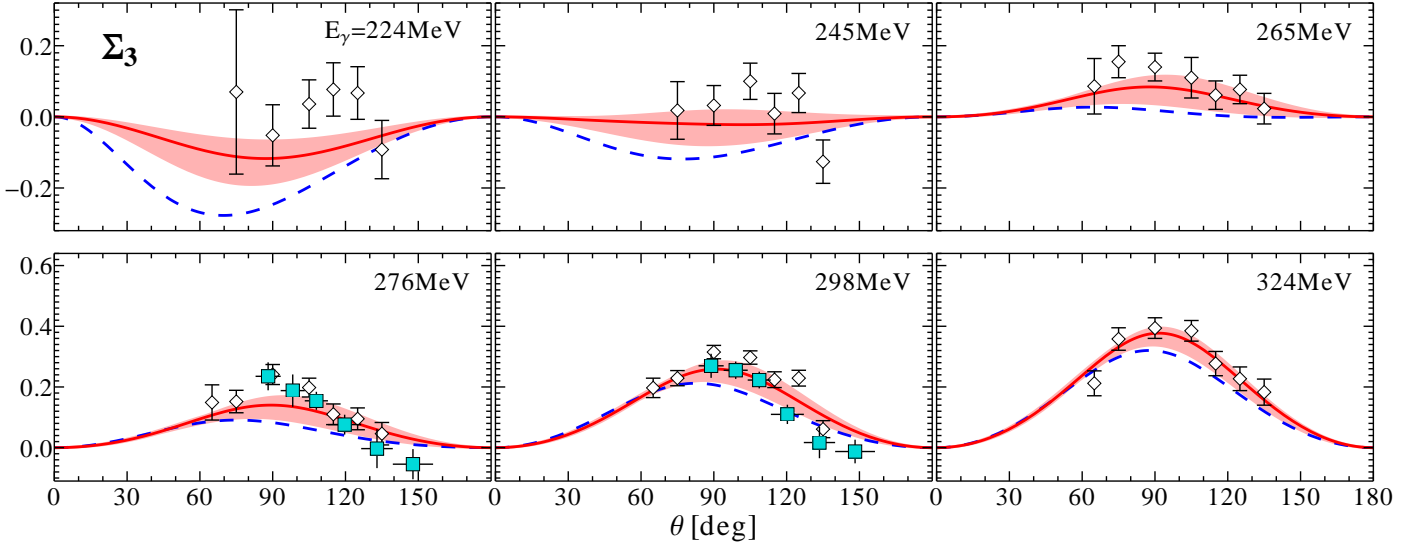


Figure 4.8: The CS beam asymmetry  $\Sigma_3$  as function of the c.m. angle at different values of the beam energy  $E_\gamma$ . The experimental data are from LEGS [13] (open diamonds) and MAMI [161] (cyan squares). The bands represent the NNLO  $B\chi$ PT result of Lensky et al. [54]. The blue dashed lines represent their calculation with only the nucleon-, pion-, and Delta-pole graphs included (chiral loops are switched off).

track are present in the event. Additional background suppression is provided by imposing a co-planarity and opening angle cut of  $15^\circ$  on the direction of the recoil proton relative to the momentum transfer direction  $\mathbf{q}$  defined by the incident and final photons. A missing mass distribution with cuts applied is shown in Fig. 4.9 for an incident photon energy of 277 MeV. In contrast to the missing mass distribution shown in Fig. 4.3, CS experiments in the  $\Delta(1232)$  region typically have prominent background due to  $\gamma p \rightarrow \pi^0 p$ . For the Mainz analysis a conservative cut is placed on the missing mass distribution to limit  $\pi^0$  background to the few percent level.

#### 4.3.2. Circularly Polarized Photons and Transversely Polarized Target

The relevant double-polarized CS asymmetry is defined as

$$\Sigma_{2x} = \frac{d\sigma_x^R - d\sigma_x^L}{d\sigma_x^R + d\sigma_x^L}, \quad (4.16)$$

where  $d\sigma_x^{R(L)}$  is the differential cross section for transverse target polarization in the  $x$ -direction, and for right (left) circularly polarized photons. Data for the  $\Sigma_{2x}$  asymmetry in the  $\Delta(1232)$  region have recently been published by the Mainz A2 collaboration [38]. Figure 4.10 shows the expected sensitivity of  $\Sigma_{2x}$  to the spin polarizabilities. The left figure shows significant sensitivity to  $\gamma_{E1E1}$ , and the right figure shows little sensitivity to  $\gamma_{M1M1}$ . Based on measurements of  $\Sigma_{2x}$  at angles  $\vartheta \approx 90^\circ$ , it is possible to uniquely identify  $\gamma_{E1E1}$  [162].

The target for this experiment was a frozen spin butanol target [163], approximately 2 cm long, where the protons in the butanol are polarized by dynamic nuclear polarization [164]. Proton polarizations were typically 90% with relaxation times on the order of 1000 hours. To remove systematic effects, the direction of polarization was reversed several times, typically once per week of experiment running time. To remove backgrounds from interactions of the photon beam with the material of the cryostat and non-hydrogen nucleons in the butanol target and He bath, separate data were taken using a carbon foam target, POCOfoam [165], with density  $0.55 \text{ g/cm}^3$  inserted into the cryostat. The density of the carbon foam was such that a cylinder of identical geometric size to the butanol target provided a close approximation to the number of non-hydrogen nucleons in the butanol target, allowing for a simple 1:1 subtraction accounting only for differences in luminosity.

Event selection is similar to that described for the Mainz  $\Sigma_3$  analysis. Even with the exclusivity selection, accidental subtraction, and opening angle requirement, backgrounds persist into the missing-mass spectrum, similar if not worse than those shown in Fig. 4.9. Typically these backgrounds are from  $\pi^0$  events, where a low-energy decay photon escaped detection by passing up or down the beam-line, or through the gap between the

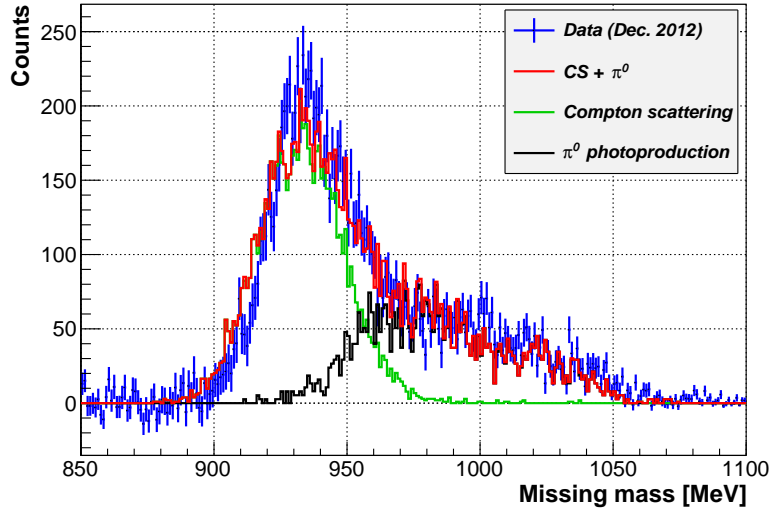


Figure 4.9: Missing mass distribution for the Mainz  $\Sigma_3$  experiment for incident photon energy  $277 \pm 10$  MeV, and  $90^\circ - 100^\circ$ . The blue histogram is data, the green curve shows the simulated response for CS, the black curve is a simulation of  $\gamma p \rightarrow \pi^0 p$  events that satisfy the exclusivity requirements for CS, and the red curve is the sum of simulated CS and  $\pi^0$  background. Plot courtesy of Cristina Collicott.

CB and TAPS. An estimate of the  $\pi^0$  background was made by measuring the rate of good  $\pi^0$  events where both decay photons are detected, but one of the photons is detected in a detector region adjacent to a region with reduced or zero acceptance. The subtraction of backgrounds is done separately for each helicity state, as the  $\pi^0$  backgrounds themselves result in non-zero asymmetries. After removing the background contributions, the final missing-mass distribution is shown in Fig. 4.11. A simulation of the CS lineshape shows good agreement between data and calculation for the Compton peak. A relatively conservative integration limit of 940 MeV was used in the analysis.

Table 4.2: Predictions for proton spin polarizabilities compared with experimental extractions (in units of  $10^{-4} \text{ fm}^4$ ).

	$O(\epsilon^3)$ [166]	$O(p^4)_a$ [167]	$O(p^4)_b$ [168]	K-matrix [89]	HDPV [97]	DR [96]	$L_\chi$ [91]	HB $\chi$ PT [51]	B $\chi$ PT [54]	Experiment
$\gamma_{E1E1}$	-1.9	-5.4	1.3	-4.8	-4.3	-5.6	-3.7	$-1.1 \pm 1.8_{\text{th}}$	$-3.3 \pm 0.8$	$-3.5 \pm 1.2$ [38]
$\gamma_{M1M1}$	0.4	1.4	3.3	3.5	2.9	3.8	2.5	$2.2 \pm 0.5 \pm 0.7_{\text{th}}$	$2.9 \pm 1.5$	$3.16 \pm 0.85$ [38]
$\gamma_{E1M2}$	0.7	1.0	0.2	-1.8	-0.02	-0.7	1.2	$-0.4 \pm 0.4_{\text{th}}$	$0.2 \pm 0.2$	$-0.7 \pm 1.2$ [38]
$\gamma_{M1E2}$	1.9	1.0	1.8	1.1	2.2	2.9	1.2	$1.9 \pm 0.4_{\text{th}}$	$1.1 \pm 0.3$	$1.99 \pm 0.29$ [38]
$\gamma_0$	-1.1	1.9	-3.9	2.0	-0.8	-0.4	-1.2	-2.6	$-0.9 \pm 1.4$	$-.90 \pm .08 \pm .11$ [169]
$\gamma_\pi$	3.5	6.8	6.1	11.2	9.4	13.0	6.1	5.6	$7.2 \pm 1.7$	$8.0 \pm 1.8$ [20]

The measured asymmetries are plotted in Fig. 4.12. The curves are from the fixed- $t$  DR model of Pasquini et al. [87] for values of  $\gamma_{E1E1}$  ranging from<sup>8</sup> -6.3 to -2.3, but with  $\gamma_{M1M1}$  fixed at 2.9 [97]. The width of each band represents the propagated errors using  $\alpha_{E1} = 12.16 \pm 0.58$  and  $\beta_{M1} = 1.66 \pm 0.69$ , as well as  $\gamma_0$  and  $\gamma_\pi$  from Table 4.2, combined in quadrature. The curves graphically demonstrate the sensitivity of the asymmetries to  $\gamma_{E1E1}$ , showing a preferred solution of  $\gamma_{E1E1} \approx -4.3 \pm 1.5$ .

Martel et al. [38] performed a global analysis of single and double-polarized CS data in the  $\Delta(1232)$  region [13, 38] using the DR model of Pasquini et al. [87], and the NNLO B $\chi$ PT calculation of Lensky and Pascalutsa [49] amended with some higher-order LECs which are then fitted to the data. Only  $\Sigma_3$  asymmetry points

<sup>8</sup>Whenever the units are omitted, it is understood that the scalar (spin) polarizabilities are measured in units of  $10^{-4} \text{ fm}^3$  ( $\text{fm}^4$ ).



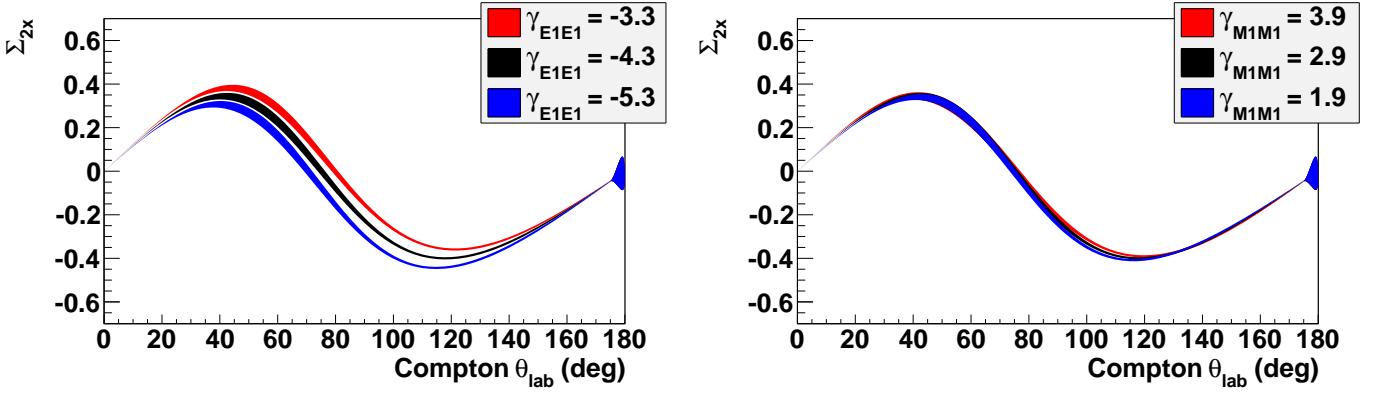


Figure 4.10: The asymmetry  $\Sigma_{2x}$  for  $E_\gamma = 290$  MeV. The curves are from a dispersion theory calculation [87] with  $\alpha_{E1}$ ,  $\beta_{M1}$ ,  $\gamma_0$ , and  $\gamma_\pi$  held fixed at their experimental values. The left plot has  $\gamma_{M1M1}$  fixed at 2.9, and the red, black, and blue bands are for  $\gamma_{E1E1}$  equal to  $-3.3$ ,  $-4.3$ , and  $-5.3$ , respectively. The width of each band represents the propagated errors from  $\alpha_{E1}$ ,  $\beta_{M1}$ ,  $\gamma_0$ , and  $\gamma_\pi$  combined in quadrature. The right plot has  $\gamma_{E1E1}$  fixed at  $-4.3$ , and the red, black, and blue bands are for  $\gamma_{M1M1}$  equal to 3.9, 2.9, and 1.9, respectively (in units of  $10^{-4}\text{fm}^4$ ). Plot courtesy of Phil Martel.

below double-pion photoproduction threshold were used in the analysis. In the fitting procedure,  $\alpha_{E1} - \beta_{M1}$ ,  $\alpha_{E1} + \beta_{M1}$ ,  $\gamma_{E1E1}$ ,  $\gamma_{M1M1}$ ,  $\gamma_0$ , and  $\gamma_\pi$  were fitted to the asymmetry data sets, and to known constraints on  $\alpha_{E1} + \beta_{M1}$ ,  $\alpha_{E1} - \beta_{M1}$ ,  $\gamma_0$ , and  $\gamma_\pi$ . The constraint  $\alpha_{E1} - \beta_{M1} = (7.6 \pm 0.9) \times 10^{-4} \text{ fm}^3$  is taken from the analysis of Ref. [65].

Table 4.3: Results from fitting  $\Sigma_{2x}$  and  $\Sigma_3$  asymmetries using either a dispersion model calculation (Disp) [87] or a B $\chi$ PT calculation [49]. Spin polarizabilities are given in units of  $10^{-4} \text{ fm}^4$ .

$\Sigma_{2x}$ [38]	$\Sigma_3$ [13]	Model	$\gamma_{E1E1}$	$\gamma_{M1M1}$
✓		Disp	$-4.6 \pm 1.6$	$-7 \pm 11$
	✓	Disp	$-1.4 \pm 1.7$	$3.20 \pm 0.85$
✓	✓	Disp	$-3.5 \pm 1.2$	$3.16 \pm 0.85$
✓	✓	B $\chi$ PT	$-2.6 \pm 0.8$	$2.7 \pm 0.5$

Table 4.3 shows results from data fitting. The first two columns give the data sets used for fitting, the third column shows the model used, and the fourth and fifth columns show the results for  $\gamma_{E1E1}$  and  $\gamma_{M1M1}$ . The first data row confirms the graphical analysis of Figures 4.10 and 4.12, that the  $\Sigma_{2x}$  data prefer a solution  $\gamma_{E1E1} \approx -4.6 \times 10^{-4} \text{ fm}^4$ , and the data by themselves have little predictive power for  $\gamma_{M1M1}$ . The second data row confirms the graphical analysis of Fig. 4.8, that the  $\Sigma_3$  data have reasonable sensitivity to  $\gamma_{M1M1}$ , and markedly less sensitivity to  $\gamma_{E1E1}$ . The third row shows the results from the combined fit of  $\Sigma_{2x}$  and  $\Sigma_3$  data using the dispersion model [87], and the fourth row shows the combined fit using the B $\chi$ PT calculation [49]. Within the uncertainties, the results for  $\gamma_{E1E1}$  and  $\gamma_{M1M1}$  from the two model fits are in agreement, indicating that the model dependence of the polarizability fitting is comparable to, or smaller than, the statistical errors.

The last column of Table 4.2 displays the results of Martel et al. [38] for all four spin polarizabilities, obtained from the combined analysis of  $\Sigma_{2x}$ ,  $\Sigma_3$  using the DR model of Pasquini et al. [87]. The empirical results for  $\gamma_0$  and  $\gamma_\pi$  shown therein have also been used in the analysis of Martel et al. [38]. There is a generally good agreement between the extracted spin polarizabilities and the  $\chi$ PT calculations [51, 52] shown in the table. The other calculations lack an uncertainty estimate, which makes them harder to judge. Nevertheless, it is rather clear from the table that the fixed- $t$  dispersive framework [87, 97] and causal K-matrix modeling [89, 91] agree rather well with the experiment as well.

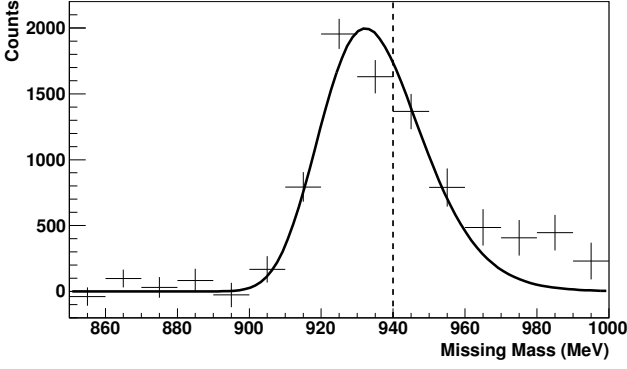


Figure 4.11: Missing-mass spectrum after removal of backgrounds for  $E_\gamma = 273 - 303$  MeV, and  $\vartheta = 100 - 120^\circ$ . The solid line is the CS lineshape determined from simulation. The dashed line indicates the upper integration limit used in the analysis. Plot courtesy of Phil Martel.

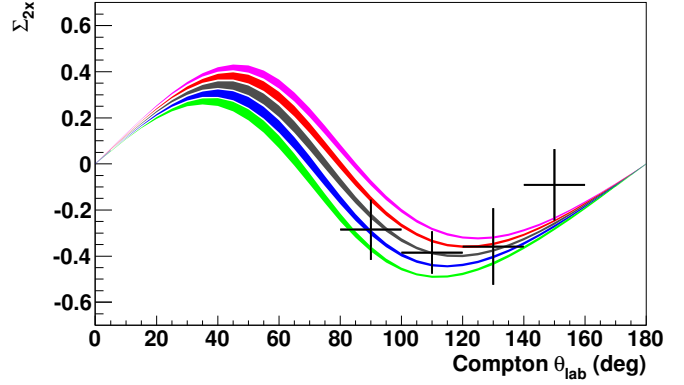


Figure 4.12:  $\Sigma_{2x}$  for  $E_\gamma = 273 - 303$  MeV. The curves are from a dispersion theory calculation [87] with  $\alpha_{E1}$ ,  $\beta_{M1}$ ,  $\gamma_0$ , and  $\gamma_\pi$  held fixed at their experimental values, and  $\gamma_{M1M1}$  fixed at 2.9 [97]. From bottom to top, the green, blue, brown, red and magenta bands are for  $\gamma_{E1E1}$  equal to  $-6.3$ ,  $-5.3$ ,  $-4.3$ ,  $-3.3$ , and  $-2.3$ , respectively. The width of each band represents the propagated errors from  $\alpha_{E1}$ ,  $\beta_{M1}$ ,  $\gamma_0$ , and  $\gamma_\pi$  combined in quadrature. Plot courtesy of Phil Martel.

#### 4.3.3. Circularly Polarized Photons and Longitudinally Polarized Target

We finally consider the following double-polarized CS asymmetry:

$$\Sigma_{2z} = \frac{d\sigma_z^R - d\sigma_z^L}{d\sigma_z^R + d\sigma_z^L}, \quad (4.17)$$

where  $d\sigma_z^{R(L)}$  is the differential cross section for right (left) circularly polarized photons to scatter from a nucleon target polarized in the incident beam direction. Note that the value of  $\Sigma_{2z}$  at the zero scattering angle is well-known from the sum rules for the forward CS amplitudes, see Sect. 5.6.

Figure 4.13 shows the sensitivity of  $\Sigma_{2z}$  to the spin polarizabilities. The definition of the curves is identical to that of Fig. 4.10. The left panel shows little sensitivity to  $\gamma_{E1E1}$ , while the right panel shows significant sensitivity to  $\gamma_{M1M1}$ . A measurement of  $\Sigma_{2z}$  will thus compliment the information obtained from the  $\Sigma_{2x}$  asymmetry. Data taking on the  $\Sigma_{2z}$  asymmetry started at MAMI in 2014, and continued in 2015.

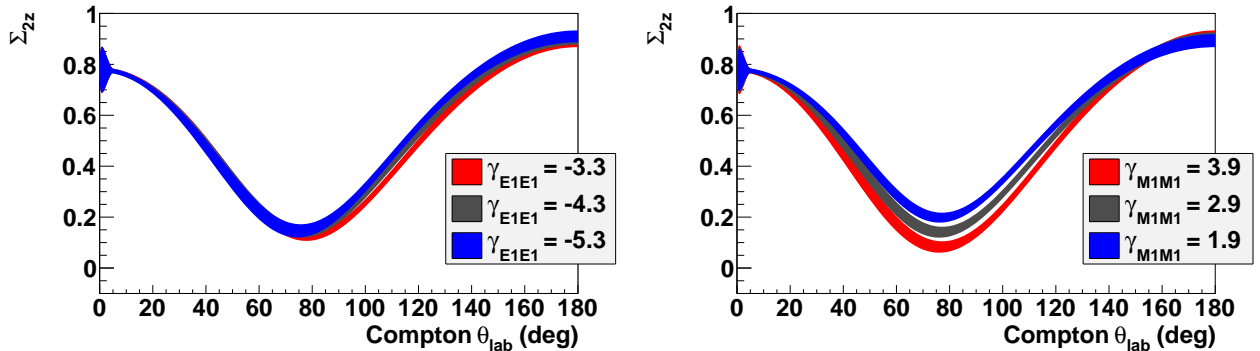


Figure 4.13: The asymmetry  $\Sigma_{2z}$  for  $E_\gamma = 290$  MeV. The curves are explained in Fig. 4.10. Plot courtesy of Phil Martel.

#### 4.4. Virtual Compton Scattering

Although the electric, magnetic and even the spin polarizabilities of the proton are now known with reasonable accuracy from CS experiments, relatively little is known about the distribution of polarizability density

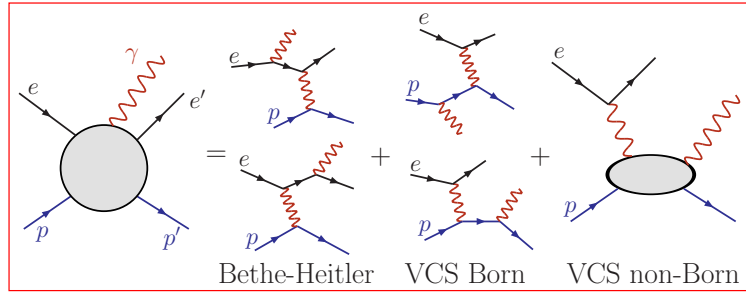


Figure 4.14: The photon electroproduction process giving access to the VCS amplitude.

inside the nucleon. To measure a polarizability density it is necessary to use the VCS reaction [170], where the incident photon is virtual. The VCS reaction is sensitive to the generalized electric and magnetic polarizabilities  $\alpha_{E1}(Q^2)$  and  $\beta_{M1}(Q^2)$ .<sup>9</sup>

#### 4.4.1. Response Functions and Generalized Polarizabilities

The relationship between VCS cross sections and the polarizabilities is most easily seen in the LEX of the unpolarized VCS cross section [170]:

$$d^5\sigma^{VCS} = d^5\sigma^{BH+Born} + |\mathbf{q}'| \Phi \Psi_0(|\mathbf{q}|, \epsilon, \theta, \phi) + O(|\mathbf{q}'|^2), \quad (4.18)$$

where  $|\mathbf{q}|(|\mathbf{q}'|)$  is the absolute value of the incident (final) photon three-momentum in the photon-nucleon c.m. frame,  $\epsilon$  is the photon polarization-transfer parameter,  $\theta(\phi)$  is the c.m. polar (azimuthal) angle for the outgoing photon, and  $\Phi$  is a phase space factor. Note that  $d^5\sigma^{BH+Born}$  is the cross section for the Bethe-Heitler + Born amplitudes only, i.e., no polarizability information is contained, and it is exactly calculable from QED and the nucleon form factors (FF). The Bethe-Heitler and Born diagrams for the VCS reaction are shown in Fig. 4.14. The polarizabilities enter the cross section expansion at order  $O(|\mathbf{q}'|)$  through the term  $\Psi_0$ , given by [66]:

$$\Psi_0(|\mathbf{q}|, \epsilon, \theta, \phi) = V_1 \left[ P_{LL}(|\mathbf{q}|) - \frac{P_{TT}(|\mathbf{q}|)}{\epsilon} \right] + V_2 \sqrt{\epsilon(1+\epsilon)} P_{LT}(|\mathbf{q}|), \quad (4.19)$$

where  $P$ 's are the response functions of unpolarized VCS, and  $V$ 's are functions of kinematical variables, the  $\epsilon$ -dependence is written out explicitly. In the limit of  $|\mathbf{q}| \rightarrow 0$ ,  $P_{LL} \propto \alpha_{E1}$ ,  $P_{TT} \propto \gamma_{E1M2}$ , and  $P_{LT} \propto \beta_{M1}$ . Therefore, response function  $P_{LL}(|\mathbf{q}|)$  is proportional to  $\alpha_{E1}(Q^2)$ ,  $P_{LT}(|\mathbf{q}|)$  is proportional to  $\beta_{M1}(Q^2)$  plus a spin polarizability term, and  $P_{TT}(|\mathbf{q}|)$  is proportional to spin polarizabilities.

There have been two analysis techniques utilized to obtain the response functions  $P_{LL}(|\mathbf{q}|) - P_{TT}(|\mathbf{q}|)/\epsilon$  and  $P_{LT}(|\mathbf{q}|)$  from VCS cross sections. The first technique is the LEX, cf. Eqs. (4.18) and (4.19). In the LEX analysis, the response functions are fitted to the  $\theta$ ,  $\phi$  and  $|\mathbf{q}'|$  dependence of VCS cross sections at fixed  $|\mathbf{q}|$  and  $\epsilon$ . To find the generalized polarizabilities  $\alpha_{E1}(Q^2)$  and  $\beta_{M1}(Q^2)$ , a theoretical calculation of  $P_{TT}$  and the spin polarizability contributions to  $P_{LT}$  must be utilized, and the predictions subtracted from the experimental results for  $P_{LL} - P_{TT}/\epsilon$  and  $P_{LT}$ . VCS experiments have generally operated in kinematic regions where the spin polarizability contributions are small, but not negligible. For example, in the kinematics of the MIT-Bates VCS experiment [14], it is estimated that the spin polarizability contribution to  $P_{LL} - P_{TT}/\epsilon$  is 8%, and the contribution to  $P_{LT}$  is 31% [173, 174].

The second technique uses the VCS dispersion model [61]. In this analysis, the VCS amplitudes obtained from the MAID  $\gamma^*p \rightarrow \pi N$  multipoles [175] are held fixed, and the two unconstrained asymptotic contributions to the VCS amplitudes are fit to experimental data at fixed  $Q^2$ . For data fitting, a dipole ansatz has traditionally

<sup>9</sup>Note that the connection between the scalar GPs (i.e., the VCS polarizabilities discussed in this section), and the VVCS polarizabilities (e.g., the generalized Baldin sum rule of (5.34)) is not known at finite  $Q^2$ . A low- $Q$  relation for some of the spin GPs exists, cf. Eq. (5.45). Alternative expansions of VVCS and VCS in generalized polarizabilities were proposed in Refs. [171] and [172].

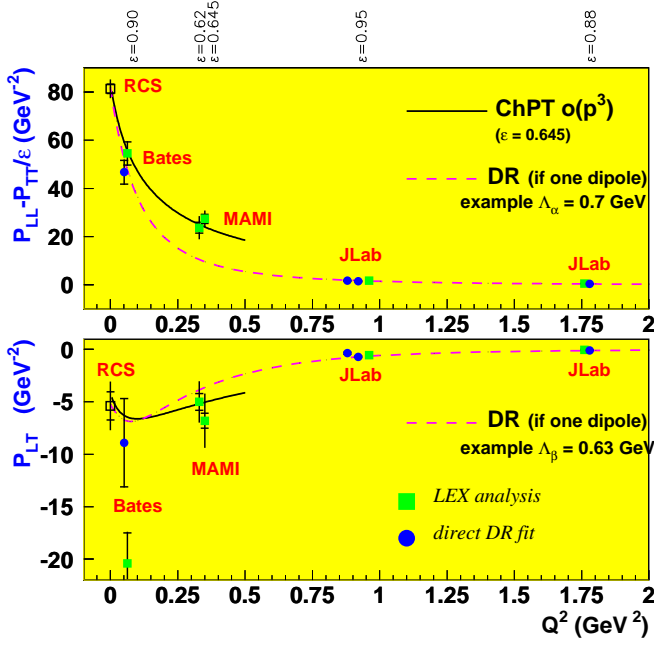


Figure 4.15: VCS response functions from: [14], Mainz 2000 [21], Mainz 2008 [22], and JLab [23]. RCS points correspond with the older values for polarizabilities [62]. The solid curves are  $O(p^3)$  HB $\chi$ PT calculation [174] with  $\epsilon = 0.9$ . The dashed curve is a dispersion-model fit [61] to the RCS and MIT-Bates data points. Plot courtesy of Helene Fonvieille.

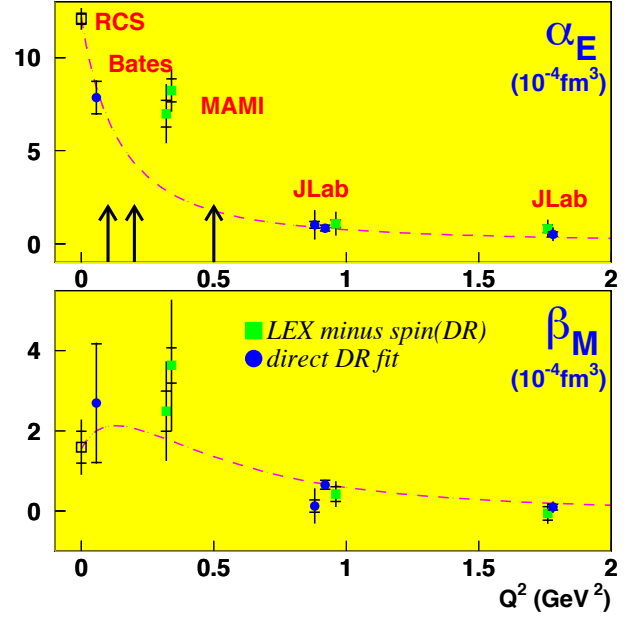


Figure 4.16: The generalized polarizabilities  $\alpha_{E1}(Q^2)$  (upper panel) and  $\beta_{M1}(Q^2)$  (lower panel). The curves and data references are the same as in Fig. 4.15. The arrows indicate  $Q^2$  of forthcoming MAMI data. Plot courtesy of Helene Fonvieille.

been used [61] to parametrize the asymptotic contributions:

$$\alpha_{E1}(Q^2) - \alpha_{E1}^{\pi N}(Q^2) = \frac{\alpha_{E1} - \alpha_{E1}^{\pi N}}{(1 + Q^2/\Lambda_\alpha^2)^2}, \quad (4.20a)$$

$$\beta_{M1}(Q^2) - \beta_{M1}^{\pi N}(Q^2) = \frac{\beta_{M1} - \beta_{M1}^{\pi N}}{(1 + Q^2/\Lambda_\beta^2)^2}. \quad (4.20b)$$

In the first equation,  $\alpha_{E1}$  is the experimental electric polarizability from RCS,  $\alpha_{E1}^{\pi N}$  is the calculated  $\pi N$  contribution to the electric polarizability at  $Q^2 = 0$ , and  $\alpha_{E1}^{\pi N}(Q^2)$  is the calculated  $\pi N$  contribution to the electric polarizability at finite  $Q^2$ . The definitions are the same for the magnetic polarizability. The only free parameters in Eq. (4.20) are  $\Lambda_\alpha$  and  $\Lambda_\beta$ . The advantage of parameterizing the generalized polarizabilities this way is that once the parameters  $\Lambda_\alpha$  and  $\Lambda_\beta$  are fixed from fitting VCS cross sections, the formalism has predictive power for the response functions and generalized polarizabilities at other  $Q^2$  values, provided of course the dipole assumption in Eq. (4.20) is valid. Once the parameters  $\Lambda_\alpha$  and  $\Lambda_\beta$  are determined, the generalized polarizabilities are calculated from Eq. (4.20), and the response functions  $P_{LL} - P_{TT}/\epsilon$  and  $P_{LT}$  are found by summing the asymptotic terms with calculated spin polarizability contributions.

The VCS response functions  $P_{LL}(|\mathbf{q}|) - P_{TT}(|\mathbf{q}|)/\epsilon$  and  $P_{LT}(|\mathbf{q}|)$  are plotted in Fig. 4.15 for the three lowest  $Q^2$  VCS experiments: MIT-Bates [14], Mainz [21] [22], and JLab [176]. The dashed curves in Fig. 4.15 are the dispersion model calculations assuming the dipole choice of Eq. (4.20), and the fitted values for  $\Lambda_\alpha$  and  $\Lambda_\beta$  that by construction make the dispersion calculations go directly through the RCS and JLab data points. As shown in Fig. 4.15, the dipole ansatz of Eq. (4.20) allows for a unified description of all low- $Q^2$  VCS response function measurements, with the exception of the Mainz  $P_{LL} - P_{TT}/\epsilon$ , and to a lesser extent  $P_{LT}$ , measurements at  $Q^2 = 0.33 \text{ GeV}^2$ .

The generalized polarizabilities  $\alpha_{E1}(Q^2)$  and  $\beta_{M1}(Q^2)$  are shown in Fig. 4.16. The dashed curves in the figures are from the dispersion model calculation using the same  $\Lambda_\alpha$  and  $\Lambda_\beta$  as shown in Fig. 4.15. Similar to

the situation shown in Fig. 4.15, the dipole assumption of Eq. (4.20) also allows for a unified description of all low- $Q^2$  polarizability measurements, with the exception of the Mainz measurements at  $Q^2 = 0.33 \text{ GeV}^2$ .

The  $\pi N$  contribution to the electric polarizability is positive at low  $Q$ , but quickly decreases and crosses 0 at  $Q^2 \approx 0.1 \text{ GeV}^2$ . Having a negative contribution to electric polarizability is not unphysical. A negative electric polarizability occurs in a class of materials known as ferroelectrics, where the internal electric field of the material is stronger than the applied external field. The  $\pi N$  contribution to the magnetic polarizability is paramagnetic (positive) in  $\text{HB}\chi\text{PT}$ , as discussed in Sect. 2.4. The asymptotic contribution is diamagnetic (negative) and mimics the effect of the LECs.

#### 4.4.2. Radial Distribution of the Electric Dipole Polarizability

The mean-square electric polarizability radius, defined as

$$\langle r^2 \rangle_{\alpha_{E1}} = -\frac{6}{\alpha_{E1}} \frac{d\alpha_{E1}(Q^2)}{dQ^2} \Big|_{Q^2=0} \quad (4.21)$$

was extracted for the proton by Bourgeois et al. [14] using the DR fit to the MIT-Bates data. Their result,

$$\langle r^2 \rangle_{\alpha_{E1}} = (2.02 + [^{+0.39}_{-0.59}]) \text{ fm}^2, \quad (4.22)$$

where the error is statistical only, is in good agreement with the  $\text{HB}\chi\text{PT}$  prediction [177] of  $1.7 \text{ fm}^2$ .

The mean-square polarizability radius is thus significantly larger than the proton mean-square charge radius (which is about  $0.77 \text{ fm}^2$ ) demonstrating the dominance of mesonic effects in the electric polarizability. The additional e.m. vertex in the polarizability diagram relative to the FF diagram increases the range of the interaction by approximately a factor of two as compared to the charge FF. Also of interest is the uncertainty principle estimate for the mean square radius of the pion cloud,  $\langle r^2 \rangle \approx (1/m_\pi)^2 = 2 \text{ fm}^2$ , which is in better agreement with  $\langle r^2 \rangle_{\alpha_{E1}}$ .

As seen in Fig. 4.16, there is poor agreement at  $Q^2 = 0.33 \text{ GeV}^2$  between the measured values of  $\alpha_{E1}(Q^2)$  and the dispersion model fit to the RCS and MIT-Bates data points. This discrepancy has been analyzed by Gorchtein et al. [178] using a light-front interpretation of the generalized polarizabilities. This formalism provides a way to calculate deformations of the quark charge densities when an external e.m. field is applied. They found that adding a Gaussian term to Eq. (4.20) to improve agreement with data at  $Q^2 = 0.33 \text{ GeV}^2$ , also gives the proton a pronounced structure in its induced polarization at large transverse distances, 0.5 to 1 fm. This is vividly shown in Fig. 4.17, where the bottom panel shows the effect of adjusting  $\alpha_{E1}(Q^2)$  to fit the Mainz data points. Clearly, additional VCS data in the low to intermediate  $Q^2$  region 0.06 to  $0.5 \text{ GeV}^2$  are needed to confirm this prediction. New

Figure 4.17: The induced polarization of the proton for a transverse electric field. White denotes positive induced polarization, and black denotes negative induced polarization. The upper panel is for the dispersion fit for  $\alpha_{E1}(Q^2)$  shown in Fig. 4.16. The lower panel is for  $\alpha_{E1}(Q^2)$  adjusted to fit the Mainz data. Plot courtesy of Marc Vanderhaeghen.

VCS data have recently been taken by the Mainz A1 collaboration at  $Q^2 \approx 0.1, 0.2$  and  $0.5 \text{ GeV}^2$ , and this data are currently under analysis [179].

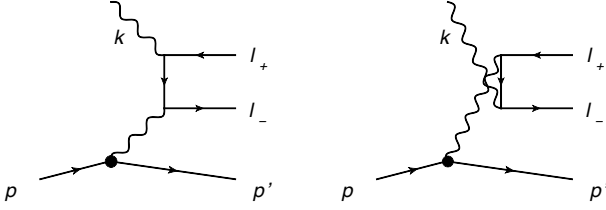


Figure 4.18: Bethe-Heitler process in dilepton photoproduction,  $\gamma p \rightarrow l^- l^+ p$ .

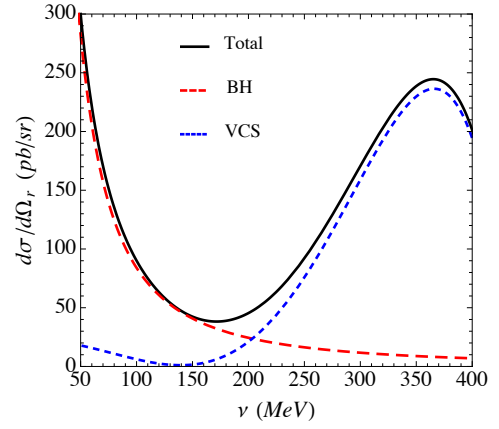


Figure 4.19: The differential cross-section of  $e^+e^-$  photoproduction off the proton as a function of the photon beam energy for forward-recoil kinematics.

#### 4.5. Timelike Compton Scattering

The process of *dilepton photoproduction* from protons by cosmic microwave background radiation,  $\gamma p \rightarrow p l^+ l^-$ , is one of the main mechanisms for depletion of cosmic-ray energy in the universe. It is dominated by the Bethe-Heitler (BH) process, Fig. 4.18, which can be accurately calculated from QED alone. In certain kinematics, however, the nuclear component—represented by timelike VCS—dominates. Until now there has been only one lab-based experiment dedicated to dilepton photoproduction off the proton [180]. Conducted in the 70s, it aimed to measure the forward CS amplitude  $f(\nu)$  at  $\nu \approx 2.2$  GeV, and to verify the Kramers-Kronig relation for the proton, cf. Sect. 5.6. Recently, Pauk and Vanderhaeghen [181] made a proposal to study the ratio between photoproduction of  $e^-e^+$  and  $\mu^-\mu^+$  pairs on a proton target in the limit of very small momentum transfer. This measurement would serve as a test of lepton universality and is of interest to the proton-radius puzzle.

Without distinguishing electrons from positrons, the cross-section element (for the  $e^+e^-$  photoproduction) can be written as an incoherent sum of BH and VCS cross-sections, the interference terms drop out because of the charge-conjugation symmetry:

$$d\sigma = d\sigma^{\text{BH}} + d\sigma^{\text{VCS}}. \quad (4.23)$$

In this case VCS can be accessed only in the regions where the BH mechanism is suppressed. In the distribution over the solid angle of the recoil proton,  $\Omega_r$ , the leading contribution to BH is given by the two diagrams shown in Fig. 4.18, which are known to cancel in the forward kinematics [182]. That is to say that  $d\sigma^{\text{BH}}/d\Omega_r$  is smallest when  $\vartheta_r = 0$ , where for pointlike proton it takes a particularly simple form:

$$\frac{d\sigma^{\text{BH}}}{d\Omega_r}(\nu, \vartheta_r = 0) = \frac{\alpha^3}{8\pi^4\nu^4} \left\{ [4m_e^2 + \nu^2] K \left( \sqrt{1 - \frac{4m_e^2}{\nu^2}} \right) - 2\nu^2 E \left( \sqrt{1 - \frac{4m_e^2}{\nu^2}} \right) \right\}, \quad (4.24)$$

with  $E$  and  $K$  being the elliptic integrals, and  $m_e$  the electron mass. On the other hand, if we neglect for a moment the momentum-transfer dependence of the VCS process, the VCS cross section factorizes into the RCS cross section and a factor responsible for the pair production:

$$\frac{d\sigma}{d\Omega_r dM_{ee}} = \frac{d\sigma^{\text{RCS}}}{d\Omega_r} \frac{\alpha}{3\pi M_{ee}^2} \sqrt{1 - \frac{4m_e^2}{M_{ee}^2}} \left( 1 + \frac{2m_e^2}{M_{ee}^2} \right) \left[ \left( 1 + \frac{M_{ee}^2}{2M\nu} \right)^2 - \frac{M_{ee}^2(M^2 + 2M\nu)}{M^2\nu^2} \right]^{3/2}, \quad (4.25)$$

where  $M_{ee}$  is the invariant mass of the lepton pair.

The resulting angular distributions for BH and VCS, as well as their sum, are shown as functions of photon energy in Fig. 4.19. The figure clearly shows that for beam energies above 200 MeV the CS off proton is the dominant mechanism. Any substantial deviation from these predictions can be interpreted as the timelike momentum-transfer dependence of the Compton process, and hence attributed to the aforementioned effects of the timelike e.m. structure of the nucleon.



## 5. Sum Rules

The fundamental relation between light absorption and scattering, encompassed for example in the celebrated Kramers–Kronig relation, is manifested in a variety of *sum rules*, which are the subjects of this section. They in particular allow one to express certain linear combinations of polarizabilities in terms of weighted energy integrals of total photoabsorption cross sections, or equivalently, in terms of the moments of structure functions [2, 61, 63, 183]. They all are derived from the analyticity, unitarity and symmetry properties of the forward CS amplitude, depicted in Fig. 5.1. In general, the photons are virtual, with spacelike virtuality  $q^2 < 0$ . The corresponding amplitude is then referred to as the forward doubly-virtual Compton scattering (VVCS) amplitude. In what follows we consider its properties, sketch the derivation of the sum rules, and discuss their empirical consequences.

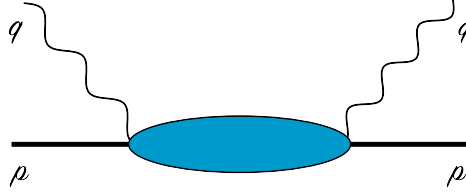


Figure 5.1: Forward Compton scattering:  $N(p) + \gamma(q) \rightarrow N(p) + \gamma(q)$ , with either real or virtual photons.

### 5.1. Forward Doubly-Virtual Compton Scattering Amplitude

In the forward kinematics ( $t = 0$ ), the Lorentz structure of the VVCS amplitude is decomposed in four independent tensor forms:

$$T^{\mu\nu}(q, p) = \left(-g^{\mu\nu} + \frac{q^\mu q^\nu}{q^2}\right) T_1(\nu, Q^2) + \frac{1}{M^2} \left(p^\mu - \frac{p \cdot q}{q^2} q^\mu\right) \left(p^\nu - \frac{p \cdot q}{q^2} q^\nu\right) T_2(\nu, Q^2) - \frac{1}{M} \gamma^{\mu\nu\alpha} q_\alpha S_1(\nu, Q^2) - \frac{1}{M^2} (\gamma^{\mu\nu} q^2 + q^\mu \gamma^{\nu\alpha} q_\alpha - q^\nu \gamma^{\mu\alpha} q_\alpha) S_2(\nu, Q^2), \quad (5.1)$$

with  $T_{1,2}$  the spin-independent and  $S_{1,2}$  the spin-dependent invariant amplitudes, functions of  $\nu = (s - u)/4M$  and  $Q^2 = -q^2$ . This decomposition is explicitly gauge invariant and splits naturally into symmetric and anti-symmetric parts,

$$T^{\mu\nu} = T_S^{\mu\nu} + T_A^{\mu\nu}, \quad (5.2)$$

which, respectively, *do not* and *do* depend on the nucleon spin. Given that the vector indices are to be contracted with either the polarization vector, satisfying  $q \cdot \varepsilon = 0$ , or with another gauge-invariant tensor, the terms containing  $q^\mu$  or  $q^\nu$  can be omitted, hence,<sup>10</sup>

$$T_S^{\mu\nu}(q, p) = -g^{\mu\nu} T_1(\nu, Q^2) + \frac{p^\mu p^\nu}{M^2} T_2(\nu, Q^2), \quad (5.3a)$$

$$T_A^{\mu\nu}(q, p) = -\frac{1}{M} \gamma^{\mu\nu\alpha} q_\alpha S_1(\nu, Q^2) + \frac{Q^2}{M^2} \gamma^{\mu\nu} S_2(\nu, Q^2). \quad (5.3b)$$

One immediate observation is that the symmetry under photon crossing translates into the following conditions, for real  $\nu$ :

$$T_1(-\nu, Q^2) = T_1(\nu, Q^2), \quad T_2(-\nu, Q^2) = T_2(\nu, Q^2), \quad (5.4a)$$

$$S_1(-\nu, Q^2) = S_1(\nu, Q^2), \quad S_2(-\nu, Q^2) = -S_2(\nu, Q^2). \quad (5.4b)$$

<sup>10</sup>It is customary to write the spin-dependent amplitude with the help of the nucleon spin four-vector  $s^\alpha$ , satisfying  $s^2 = -1$  and  $s \cdot p = 0$ :

$$T_A^{\mu\nu}(q, p) = \frac{i}{M} \epsilon^{\mu\nu\alpha\beta} q_\alpha s_\beta S_1(\nu, Q^2) + \frac{i}{M^3} \epsilon^{\mu\nu\alpha\beta} q_\alpha (p \cdot q s_\beta - s \cdot q p_\beta) S_2(\nu, Q^2).$$



Hence,  $S_2$  is odd with respect to the sign reflection of  $\nu$ , the other amplitudes are even. We will often consider the combination  $\nu S_2$ , such that it has the same crossing properties as the other amplitudes.

The Born contribution to these amplitudes is well known (cf. [Appendix A](#)) and given by [61]:

$$T_1^{\text{Born}}(\nu, Q^2) = \frac{4\pi\alpha}{M} \left\{ \frac{Q^4 [F_1(Q^2) + F_2(Q^2)]^2}{Q^4 - 4M^2\nu^2} - F_1^2(Q^2) \right\}, \quad (5.5a)$$

$$T_2^{\text{Born}}(\nu, Q^2) = \frac{16\pi\alpha M Q^2}{Q^4 - 4M^2\nu^2} \left\{ F_1^2(Q^2) + \frac{Q^2}{4M^2} F_2^2(Q^2) \right\}, \quad (5.5b)$$

$$S_1^{\text{Born}}(\nu, Q^2) = \frac{2\pi\alpha}{M} \left\{ \frac{4M^2 Q^2 [F_1(Q^2) + F_2(Q^2)] F_1(Q^2)}{Q^4 - 4M^2\nu^2} - F_2^2(Q^2) \right\}, \quad (5.5c)$$

$$S_2^{\text{Born}}(\nu, Q^2) = -\frac{8\pi\alpha M^2 \nu}{Q^4 - 4M^2\nu^2} [F_1(Q^2) + F_2(Q^2)] F_2(Q^2), \quad (5.5d)$$

where  $F_1$  and  $F_2$  are the elastic Dirac and Pauli FFs of the nucleon, which are normalized to  $F_1(0) = Z$  and  $F_2(0) = \kappa$ . Introducing the Bjorken variable,  $x = Q^2/2M\nu$ , we recall that the physical region in electron scattering corresponds with  $x \in [0, 1]$ . Obviously the Born graphs exhibit the pole at  $\nu = Q^2/2M \equiv \nu_{\text{el}}$ , or equivalently  $x = 1$ . This nucleon-pole part of the Born contribution is isolated below, see Eq. (5.13). The non-Born part of the full amplitudes will be denoted as  $\bar{T}_i, \bar{S}_i$ .

## 5.2. Unitarity and Relation to Structure Functions

The optical theorem relates the absorptive parts of the forward VVCS amplitudes to the nucleon structure functions<sup>11</sup>, or equivalently, to the cross sections of virtual-photon absorption  $\gamma^* N \rightarrow X$ :<sup>12</sup>

$$\text{Im } T_1(\nu, Q^2) = \frac{4\pi^2\alpha}{M} f_1(x, Q^2) = \nu \sigma_T(\nu, Q^2), \quad (5.6a)$$

$$\text{Im } T_2(\nu, Q^2) = \frac{4\pi^2\alpha}{\nu} f_2(x, Q^2) = \frac{Q^2\nu}{\nu^2 + Q^2} [\sigma_T + \sigma_L](\nu, Q^2), \quad (5.6b)$$

$$\text{Im } S_1(\nu, Q^2) = \frac{4\pi^2\alpha}{\nu} g_1(x, Q^2) = \frac{M\nu^2}{\nu^2 + Q^2} \left[ \frac{Q}{\nu} \sigma_{LT} + \sigma_{TT} \right](\nu, Q^2), \quad (5.6c)$$

$$\text{Im } S_2(\nu, Q^2) = \frac{4\pi^2\alpha M}{\nu^2} g_2(x, Q^2) = \frac{M^2\nu}{\nu^2 + Q^2} \left[ \frac{\nu}{Q} \sigma_{LT} - \sigma_{TT} \right](\nu, Q^2), \quad (5.6d)$$

where the cross sections are defined as:  $\sigma_T = 1/2(\sigma_{1/2} + \sigma_{3/2})$  and  $\sigma_{TT} = 1/2(\sigma_{1/2} - \sigma_{3/2})$  for transversely polarized photons, and  $\sigma_L = 1/2(\sigma_{1/2} + \sigma_{-1/2})$  for longitudinal photons, where the subscript on the right-hand side (*rhs*) indicates the total helicity of the  $\gamma^* N$  state. The cross section  $\sigma_{LT}$  corresponds with a simultaneous helicity change of the photon (from longitudinal to transverse) and the nucleon (spin-flip) such that the total helicity is conserved. These unitarity relations hold in the physical region, where the Bjorken variable is confined to the unit interval.

Figure 5.2 illustrates the photoabsorption process. The structure functions describing the purely elastic scattering, shown in the left-hand panel of Fig. 5.2, are given in terms of the elastic FFs:

$$f_1^{\text{el}}(x, Q^2) = \frac{1}{2} G_M^2(Q^2) \delta(1 - x), \quad (5.7a)$$

$$f_2^{\text{el}}(x, Q^2) = \frac{1}{1 + \tau} [G_E^2(Q^2) + \tau G_M^2(Q^2)] \delta(1 - x), \quad (5.7b)$$

$$g_1^{\text{el}}(x, Q^2) = \frac{1}{2} F_1(Q^2) G_M(Q^2) \delta(1 - x), \quad (5.7c)$$

$$g_2^{\text{el}}(x, Q^2) = -\frac{\tau}{2} F_2(Q^2) G_M(Q^2) \delta(1 - x), \quad (5.7d)$$

<sup>11</sup>The unpolarized structure functions  $f_1$  and  $f_2$  are the standard  $F_1$  and  $F_2$ . However, the latter notation is reserved here for the Dirac and Pauli FFs respectively.

<sup>12</sup>The flux factor for virtual photons which goes into these cross sections is rather arbitrary, cf. [61] for common choices. Our expressions correspond to the flux factor choice  $K = \nu$ . Expressions in terms of the structure functions are not affected by the choice of the flux factor.



Figure 5.2: (a) ‘Elastic’ and (b) ‘inelastic’ part of the photoabsorption cross section. (a) is related to the ‘pole’ contribution, whereas (b) is related to the ‘non-pole’ contribution.

where  $\tau = Q^2/4M^2$ , and the electric and magnetic Sachs FFs are linearly related to the Dirac and Pauli FFs as:

$$G_E(Q^2) = F_1(Q^2) - \tau F_2(Q^2), \quad G_M(Q^2) = F_1(Q^2) + F_2(Q^2). \quad (5.8)$$

Furthermore,  $\delta(x)$  is the Dirac delta-function, such that

$$\delta(1-x) = \nu_{\text{el}} \delta(\nu - \nu_{\text{el}}), \quad \text{with } \nu_{\text{el}} \equiv 2M\tau. \quad (5.9)$$

In the limit,  $Q^2 \rightarrow \infty$ , fixed  $x$ , the structure functions are related to the parton distribution functions. We are, however, interested in the limit where  $Q$  and  $\nu$  are small. In this case the VVCS amplitudes can on one hand be expanded in terms of polarizabilities and e.m. radii, and on the other in terms of moments of structure functions. This expansion and the resulting relations between the static e.m. properties of the nucleon and the moments of structure functions will be discussed further below. Before that, we need to establish the dispersion relations (DRs) for the forward VVCS amplitudes.

### 5.3. Analyticity and Dispersion Relations

We next consider the analytic structure of the VVCS amplitudes  $T_i$  and  $S_i$  in the complex plane of  $\nu$ . We have already seen that the Born contribution contains the nucleon pole at the kinematics of elastic scattering,  $\nu = \nu_{\text{el}}$ . The inelastic processes are manifested in the branch cuts, starting at the first particle-production threshold  $\nu_0$  and extending to infinity. Due to crossing symmetry, the analytic structure for negative real  $\nu$  is similar. In any case, the physical singularities are confined to the real axis. Elsewhere in the complex plane the amplitudes are *analytic* (or, holomorphic) functions. The latter requirement is inferred by micro-causality, a fundamental postulate of special relativity which says that all the signals propagate strictly within the light-cone.

For the subsequent discussion it is important that the VVCS amplitudes do not have a pole in the limit  $Q^2 \rightarrow 0$ , then  $\nu \rightarrow 0$ . Such a pole can only come from the nucleon propagator entering the Born contribution. From Eq. (5.5) we see that the pole is absent from all the amplitudes except  $S_2$ . We therefore will write down the DR for  $\nu S_2$ , which is pole free for real photons.

These analytic properties, together with the crossing symmetry conditions from Eq. (5.4), are well-known to result in the following DRs (cf. Appendix B for the derivation):

$$T_i(\nu, Q^2) = \frac{2}{\pi} \int_{\nu_{\text{el}}}^{\infty} d\nu' \frac{\nu' \text{Im } T_i(\nu', Q^2)}{\nu'^2 - \nu^2 - i0^+}, \quad (5.10a)$$

$$S_1(\nu, Q^2) = \frac{2}{\pi} \int_{\nu_{\text{el}}}^{\infty} d\nu' \frac{\nu' \text{Im } S_1(\nu', Q^2)}{\nu'^2 - \nu^2 - i0^+}, \quad (5.10b)$$

$$\nu S_2(\nu, Q^2) = \frac{2}{\pi} \int_{\nu_{\text{el}}}^{\infty} d\nu' \frac{\nu'^2 \text{Im } S_2(\nu', Q^2)}{\nu'^2 - \nu^2 - i0^+}, \quad (5.10c)$$

where  $0^+$  is an infinitesimally small positive number. As emphasized in the derivation of these relations, they are only valid provided the ‘‘good’’ behavior of these amplitudes for large  $\nu$ . It turns out that for  $T_1$  the above

unsubtracted DR is not warranted and at least one subtraction is required. We postpone a detailed discussion of this issue till Sect. 5.4 and Sect. 5.5 while continuing to deal here with the unsubtracted DR.

Substituting the unitarity relations, Eq. (5.6), into Eq. (5.10) we have:<sup>13</sup>

$$T_1(\nu, Q^2) = \frac{8\pi\alpha}{M} \int_0^1 dx \frac{f_1(x, Q^2)}{1 - x^2(\nu/\nu_{\text{el}})^2 - i0^+} = \frac{2}{\pi} \int_{\nu_{\text{el}}}^\infty d\nu' \frac{\nu'^2 \sigma_T(\nu', Q^2)}{\nu'^2 - \nu^2 - i0^+}, \quad (5.12a)$$

$$T_2(\nu, Q^2) = \frac{16\pi\alpha M}{Q^2} \int_0^1 dx \frac{f_2(x, Q^2)}{1 - x^2(\nu/\nu_{\text{el}})^2 - i0^+} = \frac{2Q^2}{\pi} \int_{\nu_{\text{el}}}^\infty d\nu' \frac{\nu'^2 [\sigma_T + \sigma_L](\nu', Q^2)}{(\nu'^2 + Q^2)(\nu'^2 - \nu^2 - i0^+)}, \quad (5.12b)$$

$$S_1(\nu, Q^2) = \frac{16\pi\alpha M}{Q^2} \int_0^1 dx \frac{g_1(x, Q^2)}{1 - x^2(\nu/\nu_{\text{el}})^2 - i0^+} = \frac{2M}{\pi} \int_{\nu_{\text{el}}}^\infty d\nu' \frac{\nu'^3 [\frac{Q}{\nu'} \sigma_{LT} + \sigma_{TT}](\nu', Q^2)}{(\nu'^2 + Q^2)(\nu'^2 - \nu^2 - i0^+)}, \quad (5.12c)$$

$$\nu S_2(\nu, Q^2) = \frac{16\pi\alpha M^2}{Q^2} \int_0^1 dx \frac{g_2(x, Q^2)}{1 - x^2(\nu/\nu_{\text{el}})^2 - i0^+} = \frac{2M^2}{\pi} \int_{\nu_{\text{el}}}^\infty d\nu' \frac{\nu'^3 [\frac{\nu'}{Q} \sigma_{LT} - \sigma_{TT}](\nu', Q^2)}{(\nu'^2 + Q^2)(\nu'^2 - \nu^2 - i0^+)}. \quad (5.12d)$$

Substituting here the elastic structure functions, Eq. (5.7), we obtain the nucleon-pole contribution:

$$T_1^{\text{pole}}(\nu, Q^2) = \frac{4\pi\alpha}{M} \frac{\nu_{\text{el}}^2 G_M^2(Q^2)}{\nu_{\text{el}}^2 - \nu^2 - i0^+}, \quad (5.13a)$$

$$T_2^{\text{pole}}(\nu, Q^2) = \frac{8\pi\alpha \nu_{\text{el}}}{\nu_{\text{el}}^2 - \nu^2 - i0^+} \frac{G_E^2(Q^2) + \tau G_M^2(Q^2)}{1 + \tau}, \quad (5.13b)$$

$$S_1^{\text{pole}}(\nu, Q^2) = \frac{4\pi\alpha \nu_{\text{el}}}{\nu_{\text{el}}^2 - \nu^2 - i0^+} F_1(Q^2) G_M(Q^2), \quad (5.13c)$$

$$[\nu S_2]^{\text{pole}}(\nu, Q^2) = -\frac{2\pi\alpha \nu_{\text{el}}^2}{\nu_{\text{el}}^2 - \nu^2 - i0^+} F_2(Q^2) G_M(Q^2). \quad (5.13d)$$

These pole terms vanish in the limit  $Q^2 \rightarrow 0$ , then  $\nu \rightarrow 0$ , as required.

We are now in a position to derive the various sum rules arising from low-energy and/or low-momentum expansion of the CS amplitudes. The above DRs clearly show that the expansion in energy  $\nu$  is an expansion in the moments of structure functions. For example, the Burkhardt-Cottingham (BC) sum rule [184] arises from taking the low-energy limit,  $\nu \rightarrow 0$ , of the relation (5.12d) for  $\nu S_2$ :

$$0 = \int_0^1 dx g_2(x, Q^2), \quad (5.14)$$

valid for any  $Q^2 > 0$ . Note that, although the unitarity relations are valid in the physical region only, the DRs can be valid outside of the physical region. The photon virtuality must nevertheless be spacelike,  $Q^2 > 0$ , in order to exclude the particle production off the external photons.

Subtracting the DR (5.12d) at  $\nu = 0$ , and using the BC sum rule, we obtain:

$$S_2(\nu, Q^2) = \frac{64\pi\alpha M^4 \nu}{Q^6} \int_0^1 dx \frac{x^2 g_2(x, Q^2)}{1 - x^2(\nu/\nu_{\text{el}})^2 - i0^+} = \frac{2M^2 \nu}{\pi} \int_{\nu_{\text{el}}}^\infty d\nu' \frac{\nu' [\frac{\nu'}{Q} \sigma_{LT} - \sigma_{TT}](\nu', Q^2)}{(\nu'^2 + Q^2)(\nu'^2 - \nu^2 - i0^+)}. \quad (5.15)$$

This expression could be obtained immediately by writing the DR for  $S_2$ , rather than  $\nu S_2$ , but then we would not have established the BC sum rule.

<sup>13</sup>Using that, with  $x = \nu_{\text{el}}/\nu$ ,  $\nu_{\text{el}} = Q^2/2M$ , the change of the integration variable from  $\nu$  to  $x$  goes as:

$$\int_{\nu_{\text{el}}}^\infty \frac{d\nu}{\nu^n} f(\nu, Q^2) = \left(\frac{2M}{Q^2}\right)^{n-1} \int_0^1 dx x^{n-2} f(x, Q^2). \quad (5.11)$$

#### 5.4. Sum Rules for Real Photons

We start with considering the model-independent of (5.12) for the case of  $Q^2 = 0$ . The amplitudes  $T_2$  and  $S_2$  drop out, and so do the cross sections containing longitudinal photons. We thus have:

$$T_1(\nu, 0) = \frac{2}{\pi} \int_0^\infty d\nu' \frac{\nu'^2 \sigma_T(\nu')}{\nu'^2 - \nu^2 - i0^+}, \quad (5.16a)$$

$$S_1(\nu, 0) = \frac{2M}{\pi} \int_0^\infty d\nu' \frac{\nu' \sigma_{TT}(\nu')}{\nu'^2 - \nu^2 - i0^+}. \quad (5.16b)$$

The cross sections  $\sigma_T$  and  $\sigma_{TT}$  are, respectively, the unpolarized and helicity-difference photoabsorption cross sections:  $1/2 (\sigma_{1/2} \pm \sigma_{3/2})$ . The amplitudes  $T_1(\nu, 0)$  and  $S_1(\nu, 0)$  are (up to overall factors) identical to the RCS amplitudes  $\mathcal{A}_1(\nu, 0)$  and  $\mathcal{A}_3(\nu, 0)$  introduced in Sect. 3, and hence the above DRs apply to the latter amplitudes too.

The low-energy expansion of the amplitudes goes as:

$$\frac{1}{4\pi} T_1(\nu, 0) = -\frac{Z^2 \alpha}{M} + (\alpha_{E1} + \beta_{M1}) \nu^2 + [\alpha_{E1\nu} + \beta_{M1\nu} + 1/12 (\alpha_{E2} + \beta_{M2})] \nu^4 + O(\nu^6), \quad (5.17a)$$

$$\frac{1}{4\pi} S_1(\nu, 0) = -\frac{\alpha \kappa^2}{2M} + M \gamma_0 \nu^2 + M \bar{\gamma}_0 \nu^4 + O(\nu^6), \quad (5.17b)$$

where the  $O(\nu^0)$  terms represent the low-energy theorem (LET) [137, 138]; the scalar polarizabilities  $\alpha_E$  and  $\beta_M$  are introduced in Sect. 2; the forward spin polarizabilities  $\gamma_0$ ,  $\bar{\gamma}_0$  are linear combinations of spin polarizabilities, e.g.:

$$\gamma_0 = -(\gamma_{E1E1} + \gamma_{M1M1} + \gamma_{E1M2} + \gamma_{M1E2}). \quad (5.18)$$

The *rhs* of Eq. (5.16) can also be Taylor expanded in  $\nu^2$  and each term matched to the low-energy expansion of the amplitude on the left-hand side (*lhs*). We however run immediately into the following difficulty. At  $\nu = 0$  (the 0<sup>th</sup> order in  $\nu$ ), the relation for  $T_1$  yields an apparently wrong result:

$$-Z^2 \alpha / M = (2/\pi) \int_0^\infty d\nu \sigma_T(\nu). \quad (5.19)$$

The *lhs* is negative definite whereas the *rhs* is positive definite. The empirical knowledge of the photoabsorption cross section for the nucleon shows in addition that the integral on the *rhs* diverges. This invalidates the unsubtracted DR for  $T_1$ . A common choice is to make a subtraction at  $\nu = 0$ , and use the LET to obtain:

$$T_1(\nu, 0) = -\frac{4\pi Z^2 \alpha}{M} + \frac{2\nu^2}{\pi} \int_0^\infty d\nu' \frac{\sigma_T(\nu')}{\nu'^2 - \nu^2 - i0^+}. \quad (5.20)$$

The integral now converges and its evaluation for the proton will be discussed in Sect. 5.6.

Matching the low-energy expansion of  $T_1$  at  $O(\nu^2)$ , one obtains the Baldin sum rule [2]:

$$\alpha_{E1} + \beta_{M1} = \frac{1}{2\pi^2} \int_0^\infty d\nu \frac{\sigma_T(\nu)}{\nu^2}. \quad (5.21)$$

At  $O(\nu^4)$ , we obtain a sum rule for a linear combination of the energy slope of the dipole polarizabilities ( $\alpha_{E1\nu}$ ,  $\beta_{M1\nu}$ ) and the quadrupole polarizabilities ( $\alpha_{E2}$ ,  $\beta_{M2}$ ) [60]:

$$\alpha_{E1\nu} + \beta_{M1\nu} + 1/12 (\alpha_{E2} + \beta_{M2}) = \frac{1}{2\pi^2} \int_0^\infty d\nu \frac{\sigma_T(\nu)}{\nu^4}, \quad (5.22)$$

referred to as the 4<sup>th</sup>-order Baldin sum rule.

Considering the low-energy expansion of  $S_1$ , at the 0<sup>th</sup> order one obtains the celebrated Gerasimov-Drell-Hearn (GDH) sum rule [185–187]:

$$\frac{\alpha}{M^2} \kappa^2 = -\frac{1}{\pi^2} \int_0^\infty d\nu \frac{\sigma_{TT}(\nu)}{\nu}, \quad (5.23)$$

which expresses the anomalous magnetic moment  $\kappa$  in terms of an energy-weighted integral of the helicity-difference photoabsorption cross section. This is probably the best studied sum rule. It directly demonstrates the idea of expressing a purely quantum effect, which is the anomalous magnetic moment, in terms of a classical quantity, which is the cross section. The perturbative verifications of the GDH sum rule in QED and other quantum field theories provide further insight into quantum dynamics (see, e.g., Refs. [188–192]).

At  $O(\nu^2)$  one arrives at the forward spin polarizability (FSP) sum rule, also referred to as the Gell-Mann, Goldberger and Thirring (GGT) sum rule [183]:

$$\gamma_0 = \frac{1}{2\pi^2} \int_0^\infty d\nu \frac{\sigma_{TT}(\nu)}{\nu^3}, \quad (5.24)$$

while at  $O(\nu^4)$  one obtains the higher-order FSP sum rule [169]:

$$\bar{\gamma}_0 = \frac{1}{2\pi^2} \int_0^\infty d\nu \frac{\sigma_{TT}(\nu)}{\nu^5}. \quad (5.25)$$

The numerical evaluation of these sum rules based on empirical photoabsorption cross sections is discussed in Sect. 5.6.

### 5.5. Relations at Finite $Q$

The main idea in the derivation of sum rules is to use the unitarity relations in combination with the DRs, Eq. (5.12), and then expand the left- and right-hand sides in the photon energy  $\nu$  and the virtuality  $Q^2$ . In so doing, one expresses the static e.m. properties of the nucleon (e.g., magnetic moment, charge radius, polarizabilities), which appear as coefficients in the low-momentum expansion of the VVCS amplitudes, in terms of the moments of its structure functions. In what follows, we derive a number of such sum rules and relations for the spin-independent and spin-dependent properties of the nucleon.

#### 5.5.1. Spin-Independent Relations

As we have established, for  $Q^2 = 0$  the convergence properties of the  $T_1$  amplitude are such that its DR requires one subtraction. It is customary to choose  $\nu = 0$  as the subtraction point, leading to:

$$T_1(\nu, Q^2) = T_1(0, 0) + \frac{2}{\pi} \left\{ \int_{\nu_{\text{el}}}^\infty d\nu' \frac{\nu' \text{Im} T_1(\nu', Q^2)}{\nu'^2 - \nu^2 - i0^+} - \int_0^\infty d\nu' \frac{\text{Im} T_1(\nu', 0)}{\nu' - i0^+} \right\}. \quad (5.26)$$

The subtraction term, in accordance with the classic LET of Low [137], Gell-Mann and Goldberger [138], is given by the Thomson term:

$$T_1(0, 0) = -4\pi Z^2 \alpha / M, \quad (5.27)$$

while the rest of the amplitude  $T_1(\nu, Q^2)$  could completely be determined by an integral of  $\text{Im} T_1 = (4\pi^2 \alpha / M) f_1$ . That would be quite remarkable, because we could calculate  $T_1(0, Q^2)$  and then for instance take its non-Born piece which goes as:

$$\bar{T}_1(0, Q^2) = 4\pi \beta_{M1} Q^2 + O(Q^4), \quad (5.28)$$

and extract the magnetic polarizability. In other words, we could have a sum rule for  $\beta_{M1}$  and for  $\alpha_{E1}$  separately, rather than together as in the Baldin sum rule.

Unfortunately, this appears to be not possible, as the DR requires a subtraction at each  $Q^2$ , cf. [193–195]. In this case  $T_1(0, Q^2)$  is an unknown subtraction function, and the corresponding DR reads:

$$\begin{aligned} T_1(\nu, Q^2) &= T_1(0, Q^2) + \frac{2\nu^2}{\pi} \int_{\nu_{\text{el}}}^\infty d\nu' \frac{\text{Im} T_1(\nu', Q^2)}{\nu'(\nu'^2 - \nu^2 - i0^+)}, \\ &= T_1(0, Q^2) + \frac{32\pi \alpha M \nu^2}{Q^4} \int_0^1 dx \frac{x f_1(x, Q^2)}{1 - x^2(\nu/\nu_{\text{el}})^2 - i0^+}, \\ &= T_1(0, Q^2) + \frac{2\nu^2}{\pi} \int_{\nu_{\text{el}}}^\infty d\nu' \frac{\sigma_T(\nu', Q^2)}{\nu'^2 - \nu^2 - i0^+}. \end{aligned} \quad (5.29)$$

For the other spin-independent amplitude we shall continue to use the unsubtracted DR of Eq. (5.12b).

In the real-photon limit, an immediate observation is that

$$\frac{\partial}{\partial Q^2} T_2(\nu, Q^2) \Big|_{Q^2=0} = \frac{T_1(\nu, 0) - T_1(0, 0)}{\nu^2} = \frac{2}{\pi} \int_0^\infty d\nu' \frac{\sigma_T(\nu')}{\nu'^2 - \nu^2 - i0^+}. \quad (5.30)$$

For finite  $Q$ , the pole part of the amplitudes,  $T_i^{\text{pole}}$  in Eq. (5.13), satisfies the DR with the elastic part of the structure functions. We therefore consider just the non-pole parts and their determination from the inelastic structure functions.

The low-energy, low-momentum expansion of the spin-independent amplitudes is given by:

$$\begin{aligned} \frac{1}{4\pi} [T_1 - T_1^{\text{pole}}](\nu, Q^2) &= -\frac{Z^2\alpha}{M} + \left( \frac{Z\alpha}{3M} \langle r^2 \rangle_1 + \beta_{M1} \right) Q^2 + (\alpha_{E1} + \beta_{M1}) \nu^2 \\ &\quad + [\alpha_{E1\nu} + \beta_{M1\nu} + 1/12 (\alpha_{E2} + \beta_{M2})] \nu^4 + \dots, \end{aligned} \quad (5.31a)$$

$$\frac{1}{4\pi} [T_2 - T_2^{\text{pole}}](\nu, Q^2) = (\alpha_{E1} + \beta_{M1}) Q^2 + [\alpha_{E1\nu} + \beta_{M1\nu} + 1/12 (\alpha_{E2} + \beta_{M2})] Q^2 \nu^2 + \dots \quad (5.31b)$$

where, in case of  $T_1$ , the Thomson term and the Dirac radius  $\langle r^2 \rangle_1 = -6 \, d/dQ^2 F_1(Q^2)|_{Q^2=0}$ , come from the non-pole part of the Born contribution.

The fact that the same combination of polarizabilities enters in both amplitudes follows from Eq. (5.30). We thus have for instance that the Baldin sum rule can equivalently be written as:

$$\alpha_{E1} + \beta_{M1} = \lim_{Q^2 \rightarrow 0} \frac{8\alpha M}{Q^4} \int_0^{x_0} dx x f_1(x, Q^2) = \lim_{Q^2 \rightarrow 0} \frac{4\alpha M}{Q^4} \int_0^{x_0} dx f_2(x, Q^2), \quad (5.32)$$

where  $x_0$  is the inelastic threshold. At the next order in  $\nu^2$ , we have the 4<sup>th</sup>-order sum rule:

$$\alpha_{E1\nu} + \beta_{M1\nu} + 1/12 (\alpha_{E2} + \beta_{M2}) = \lim_{Q^2 \rightarrow 0} \frac{32\alpha M^3}{Q^6} \int_0^{x_0} dx x^3 f_1(x, Q^2) = \lim_{Q^2 \rightarrow 0} \frac{16\alpha M^3}{Q^6} \int_0^{x_0} dx x^2 f_2(x, Q^2). \quad (5.33)$$

These sum rules can be generalized to finite  $Q$ , and the usual choice is to do that using  $f_1$ . E.g., the generalization of the Baldin sum rule reads [61]:

$$\alpha_{E1}(Q^2) + \beta_{M1}(Q^2) = \frac{8\alpha M}{Q^4} \int_0^{x_0} dx x f_1(x, Q^2). \quad (5.34)$$

It was evaluated in Ref. [196], and more recently in Refs. [57, 58] using an improved empirical parametrization of the structure function  $f_1$ .

In general, the relation in Eq. (5.30) implies that the longitudinal structure function:

$$f_L(x, Q^2) = -2x f_1(x, Q^2) + f_2(x, Q^2), \quad (5.35)$$

which is known to vanish for asymptotically large  $Q^2$  (Callan–Gross relation), also vanishes for low  $Q^2$ , and its moments go as:  $\lim_{Q^2 \rightarrow 0} Q^{-4-2n} \int dx x^{2n} f_L(x, Q^2) = 0$ .

It is natural to consider the combination,  $\tilde{f}_L \equiv f_L + (2Mx/Q)^2 f_2 = Q^2 \sigma_L(\nu, Q^2)/4\pi^2\alpha$ , and define a longitudinal polarizability as:<sup>14</sup>

$$\alpha_L(Q^2) = \frac{4\alpha M}{Q^6} \int_0^{x_0} dx \tilde{f}_L(x, Q^2) = \frac{1}{2\pi^2} \int_{\nu_0}^\infty d\nu \frac{\sigma_L(\nu, Q^2)}{Q^2 \nu^2}. \quad (5.36)$$

At low  $Q^2$  this quantity is easily described in  $B\chi$ PT, but not in  $HB\chi$ PT, cf. [34, Fig. 3]. As all the quantities involving the longitudinal polarization, it is fairly insensitive to the  $\Delta(1232)$ -resonance excitation.

<sup>14</sup>This definition differs from the original one [61] by a factor  $1/Q^2$ , and as the result,  $\alpha_L(0)$  is not vanishing here.



### 5.5.2. Spin-Dependent Relations

The sum rule derivation for the spin-dependent amplitudes proceeds in the same steps. As noted earlier, the DR for  $\nu S_2$  in the limit  $\nu \rightarrow 0$  leads to the BC sum rule [184], see Eq. (5.14). This sum rule implies the following relation between the elastic and inelastic part of  $S_2$ :

$$I_2(Q^2) \equiv \frac{2M^2}{Q^2} \int_0^{x_0} dx g_2(x, Q^2) = \frac{1}{4} F_2(Q^2) G_M(Q^2). \quad (5.37)$$

We next consider the simultaneous expansion of the non-pole parts in  $\nu$  and  $Q^2$  [59, 197]:

$$\begin{aligned} \frac{1}{4\pi} [S_1 - S_1^{\text{pole}}](\nu, Q^2) &= \frac{\alpha}{2M} \kappa^2 \left[ -1 + \frac{1}{3} Q^2 \langle r^2 \rangle_2 \right] + M \gamma_0 \nu^2 + M Q^2 \left\{ \gamma_{E1M2} \right. \\ &\quad \left. - 3M\alpha [P'^{(M1,M1)1}(0) + P'^{(L1,L1)1}(0)] \right\} + O(\nu^4, \nu^2 Q^2, Q^4), \end{aligned} \quad (5.38a)$$

$$\begin{aligned} \frac{\nu}{4\pi} [S_2 - S_2^{\text{pole}}](\nu, 0) &= \frac{\alpha \kappa}{2} G_M(0) - M^2 \nu^2 \left\{ \gamma_0 + \gamma_{E1E1} \right. \\ &\quad \left. - 3M\alpha [P'^{(M1,M1)1}(0) - P'^{(L1,L1)1}(0)] \right\} + O(\nu^4, \nu^2 Q^2, Q^4), \end{aligned} \quad (5.38b)$$

where  $\kappa$  is the nucleon anomalous magnetic moment;  $\langle r^2 \rangle_2 = -6/\kappa \, d/dQ^2 F_2(Q^2)|_{Q^2=0}$  is the mean-square Pauli radius;  $\gamma_{E1M2}$  and  $\gamma_{E1E1}$  are the spin polarizabilities;  $\gamma_0$  is the forward spin polarizability; and  $P$ s are the generalized polarizabilities (GPs) coming from the VCS, see Eq. (5.46) below. In each case the first term originates from the difference between the Born and pole amplitudes, whereas polarizabilities affect the non-Born part of the amplitudes only.

On the *rhs* of the DRs for  $S_1$  and  $S_2$  we have an expansion in terms of moments of the spin structure functions  $g_1$  and  $g_2$ . The 0<sup>th</sup> moment of  $g_1$  is related to the generalized GDH integrals:

$$I_1(Q^2) = \frac{2M^2}{Q^2} \int_0^{x_0} dx g_1(x, Q^2), \quad (5.39a)$$

$$I_A(Q^2) = \frac{2M^2}{Q^2} \int_0^{x_0} dx g_{TT}(x, Q^2) = \frac{M^2}{4\pi^2 \alpha} \int_{\nu_0}^{\infty} \frac{d\nu}{\nu} \sigma_{TT}(\nu, Q^2), \quad (5.39b)$$

with  $g_{TT} = g_1 - (4M^2 x^2/Q^2) g_2$ . In the limit,  $Q \rightarrow 0$ ,  $\nu \rightarrow 0$ , they yield the GDH sum rule of (5.23):

$$-\frac{1}{4} \kappa^2 = I_1(0) = I_A(0). \quad (5.40)$$

The 2<sup>nd</sup> moments appear in the following generalization of the forward spin polarizabilities [61]:

$$\gamma_0(Q^2) = \frac{16\alpha M^2}{Q^6} \int_0^{x_0} dx x^2 g_{TT}(x, Q^2) = \frac{1}{2\pi^2} \int_0^{\infty} \frac{d\nu}{\nu^3} \sigma_{TT}(\nu, Q^2), \quad (5.41)$$

$$\delta_{LT}(Q^2) = \frac{16\alpha M^2}{Q^6} \int_0^{x_0} dx x^2 [g_1 + g_2](x, Q^2) = \frac{1}{2\pi^2} \int_0^{\infty} \frac{d\nu}{\nu^2 Q} \sigma_{LT}(\nu, Q^2), \quad (5.42)$$

which evidently satisfy the following relations at  $Q^2 = 0$ :

$$\gamma_0 = \lim_{Q^2 \rightarrow 0} \frac{16\alpha M^2}{Q^6} \int_0^{x_0} dx x^2 g_1(x, Q^2), \quad (5.43)$$

$$\delta_{LT} = \gamma_0 + \lim_{Q^2 \rightarrow 0} \frac{16\alpha M^2}{Q^6} \int_0^{x_0} dx x^2 g_2(x, Q^2). \quad (5.44)$$

The first of these is simply the GTT sum rule given in Eq. (5.24). At large  $Q^2$ , where the Wandzura–Wilczek relation [198] [quoted in Eq. (6.45) below] is applicable and the elastic contributions neglected, one can show [61]:  $\delta_{LT}(Q^2) = \frac{1}{3} \gamma_0(Q^2)$ .

From the  $Q^2$  term in the expansion of  $S_1$ , and the  $\nu^2$  term in the expansion of  $S_2$ , one obtains the following relations involving the GPs [59]:

$$\alpha I_1'(0) = \frac{1}{12} \alpha \kappa^2 \langle r^2 \rangle_2 + \frac{1}{2} M^2 \gamma_{E1M2} - \frac{3}{2} \alpha M^3 [P'^{(M1,M1)1}(0) + P'^{(L1,L1)1}(0)], \quad (5.45a)$$

$$\delta_{LT} = -\gamma_{E1E1} + 3\alpha M [P'^{(M1,M1)1}(0) - P'^{(L1,L1)1}(0)]. \quad (5.45b)$$

The momentum derivatives of the GPs are given by:

$$P'^{(L1,L1)1}(0) \pm P'^{(M1,M1)1}(0) \equiv \frac{d}{dq^2} \left[ P^{(L1,L1)1}(q^2) \pm P^{(M1,M1)1}(q^2) \right]_{q^2=0}, \quad (5.46)$$

with  $q^2$  being the initial photon c.m. three-momentum squared. The superscript indicates the multiplicities,  $L1(M1)$  denoting electric (magnetic) dipole transitions of the initial and final photons, and '1' implies that these transitions involve the spin-flip of the nucleon, cf. [66, 170]. An empirical implication of these relations, in the context of the so-called " $\delta_{LT}$ -puzzle", is briefly considered in Sect. 7.

Another combination of the 2<sup>nd</sup> moments of spin structure functions, i.e.:

$$\bar{d}_2(Q^2) = \int_0^{x_0} dx x^2 [3g_2(x, Q^2) + 2g_1(x, Q^2)], \quad (5.47)$$

is of interest in connection to the concept of *color polarizability* [199]. In terms of the above-introduced quantities it reads:

$$\bar{d}_2(Q^2) = \frac{Q^4}{8M^4} \left\{ \frac{M^2 Q^2}{\alpha} \delta_{LT}(Q^2) + [I_1(Q^2) - I_A(Q^2)] \right\}, \quad (5.48)$$

hence goes as  $Q^6$  for low  $Q$ .

### 5.6. Empirical Evaluations of Sum Rules

Recall that the forward RCS is described by two scalar amplitudes, denoted here [and in (4.10a)] as:

$$f(\nu) \equiv \frac{T_1(\nu, 0)}{4\pi} = \frac{\sqrt{s}}{M} (\Phi_1 + \Phi_5)|_{\theta=0}, \quad g(\nu) \equiv \frac{\nu S_1(\nu, 0)}{4\pi M} \frac{\sqrt{s}}{M} (\Phi_1 + \Phi_5)|_{\theta=0}. \quad (5.49)$$

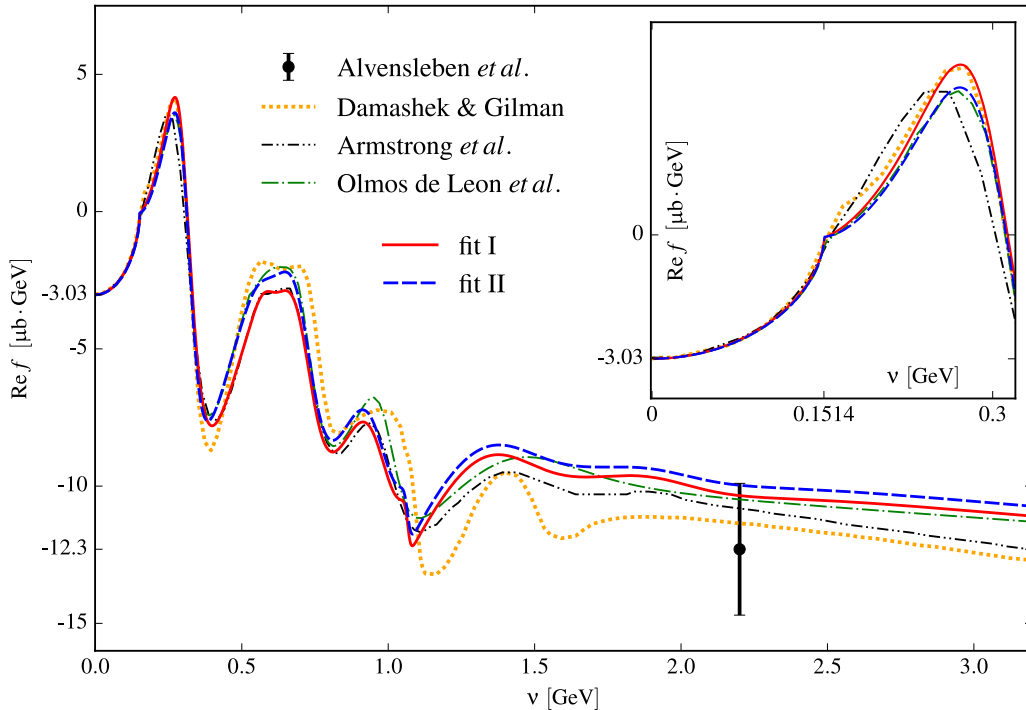


Figure 5.3: Amplitude  $f(\nu)$  for the proton obtained from Eq. (5.50a) using different fits of the total photoabsorption cross section [17, 60, 200, 201] (fit I & II refer to the results of Ref. [60]). The experimental point is from DESY [180].

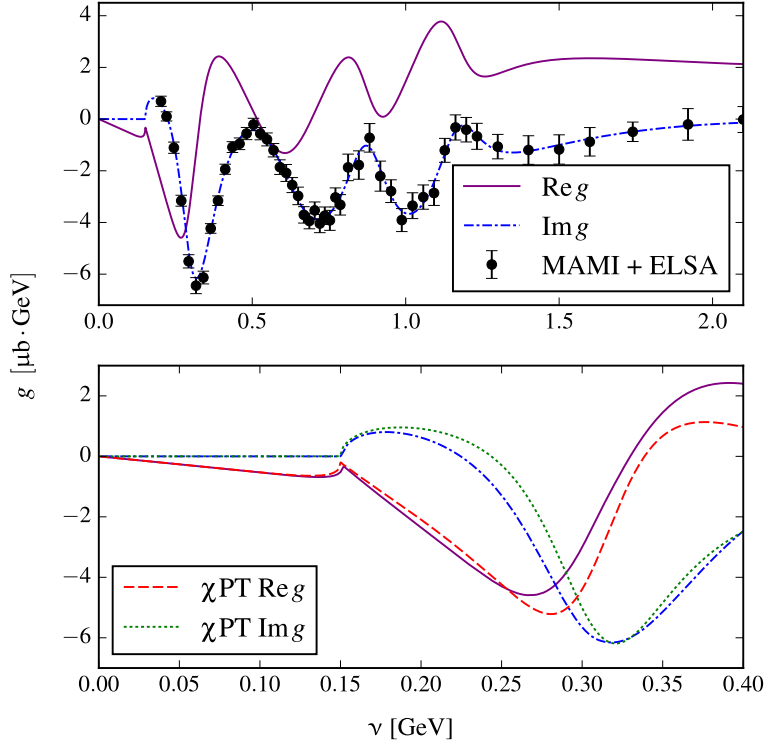


Figure 5.4: Spin-dependent amplitude  $g(\nu)$  obtained from Eq. (5.50b). The lower panel shows also the  $B\chi PT$  predictions for this amplitude [49, 54].

The corresponding DRs, Eqs. (5.20) and (5.16b), then read as follows:

$$f(\nu) = -\frac{Z^2\alpha}{M} + \frac{\nu^2}{2\pi^2} \int_0^\infty d\nu' \frac{\sigma_T(\nu')}{\nu'^2 - \nu^2 - i0^+}, \quad (5.50a)$$

$$g(\nu) = \frac{\nu}{2\pi^2} \int_0^\infty d\nu' \frac{\nu' \sigma_{TT}(\nu')}{\nu'^2 - \nu^2 - i0^+}. \quad (5.50b)$$

Therefore, given the total unpolarized cross section  $\sigma_T$  and the helicity-difference cross-section  $\sigma_{TT}$ , the forward CS can be completely determined. The cross sections for the proton are fairly well known. Their most recent fits and the evaluation of the integrals are performed by Gryniuk et al. [60]. The corresponding results for the amplitudes are displayed in Fig. 5.3 and Fig. 5.4. The first figure shows also the results of previous evaluations and an experimental point from the DESY 1973 experiment [180]. The second figure shows in the upper panel the fit to  $\text{Im } g$  together with the corresponding result for the real part, whereas in the lower panel these results are compared with a  $B\chi PT$  calculation [49] at lower energy. Given these amplitudes, one can determine the two, non-vanishing in the forward limit, observables:

$$\frac{d\sigma}{d\Omega_L} \Big|_{\theta=0} = |f|^2 + |g|^2, \quad \Sigma_{2z} \Big|_{\theta=0} = -\frac{fg^* + f^*g}{|f|^2 + |g|^2}. \quad (5.51)$$

Thus obtained  $\Sigma_{2z}$  [202], compared with the  $B\chi PT$  predictions, shows the importance of chiral dynamics in this observable, cf. [54, Fig. 16].

One can also evaluate the various sum rules presented in Sect. 5.4. Evaluations of the sum rules deriving from  $f(\nu)$  (i.e., Baldin sum rule, etc.) are gathered in Table 5.1 for the proton and neutron, respectively. These results are summarized and compared to the state-of-art  $\chi PT$  results in Figures 7.1 and 7.2.

Damashek and Gilman [200] initiated a study of the high-energy behavior of the amplitude  $f(\nu)$  for the proton. In addition to the Regge prediction, they found a constant contribution comparable in sign and magnitude to the Thomson term:  $-\alpha/M \simeq -3.03 \mu\text{b GeV}$ . This extra real constant is assumed to correspond to a

fixed  $J = 0$  Regge pole ( $\alpha_i(t) = 0$ ) [203, 204], originating from local photon interactions with the constituent quarks. Based on newer photoabsorption data, Gorchtein et al. [205] have obtained a significantly smaller value  $f(\infty) = (-0.72 \pm 0.35) \mu\text{b GeV}$ .

Recently, Gasser et al. [29] have made a sum rule determination of the proton-neutron difference (isovector combination) of the electric dipole polarizability:

$$\alpha_{E1}^{(p-n)} = -1.7(4) \times 10^{-4} \text{ fm}^3. \quad (5.52)$$

Their calculation is based on a Reggeon dominance assumption, which means there is no fixed pole in the isovector CS amplitude. It could be that the fixed pole, which is likely to be present for the proton, is canceled exactly by the one of the neutron. However, this is yet to be verified. The fact that the above value is in agreement with the empirical information on the isovector polarizability is certainly encouraging.

Table 5.1: Empirical evaluation of spin-independent sum rules for the proton and neutron.

	Baldin SR [ $10^{-4} \text{ fm}^3$ ]		4 <sup>th</sup> -order SR [ $10^{-4} \text{ fm}^5$ ]		6 <sup>th</sup> -order SR [ $10^{-4} \text{ fm}^7$ ]	Re $f(\nu = 2.2 \text{ GeV})$ [ $\mu\text{b GeV}$ ]
	Proton	Neutron	Proton	Neutron	Proton	Proton
Gryniuk et al. [60]	14.00 $\pm$ 0.20		6.04 $\pm$ 0.03		4.39 $\pm$ 0.03	-10.18
Armstrong et al. [201]						-10.8
Damashek and Gilman [200]	14.2 $\pm$ 0.3					
Schröder [206]	14.7 $\pm$ 0.7	13.3 $\pm$ 0.7	6.4	5.6		
Babusci et al. [207]	13.69 $\pm$ 0.14	14.40 $\pm$ 0.66				
Levchuk and L'vov [208]	14.0(3...5)	15.2 $\pm$ 0.4				
Olmos de León et al. [17]	13.8 $\pm$ 0.4					-10.5
MAID ( $\pi$ channel) [209]	11.63	13.28				
SAID ( $\pi$ channel) [210]	11.5	12.9				
Alvensleben et al. [180]						-12.3 $\pm$ 2.4

Table 5.2: Empirical evaluation of the GDH and GTT sum rules for the proton and neutron.

	GDH SR [ $\mu\text{b}$ ]		$\gamma_0$ [ $10^{-4} \text{ fm}^4$ ]	
	Proton	Neutron	Proton	Neutron
Sum rule value ( $lhs$ )	205	233		
GDH-Coll. [211–214]	212 $\pm$ 17	225	-1.01 $\pm$ 0.13	
Gryniuk et al. [202]	204.5 $\pm$ 9.4		-0.93 $\pm$ 0.06	
Pasquini et al. [169]	210 $\pm$ 15		-0.90 $\pm$ 0.14	
Babusci et al. [96]			-1.5	-0.4
Schumacher and Levchuk [215]			-0.58 $\pm$ 0.20	0.38 $\pm$ 0.22
MAID ( $\pi$ channel) [209]	-165.65	-132.32	-0.730	-0.005
SAID ( $\pi$ channel) [210]	-187	-137	-0.85	-0.08

The evaluations of the GDH and GTT sum rules, deriving from  $g(\nu)$ , are presented in Table 5.2 and Fig. 7.4. These results became largely possible due to the GDH-Collaboration data for the helicity-difference photoabsorption cross section, in the region from 0.2 to 2.9 GeV [211, 213, 216, 217].

For the proton, the running GDH integral,

$$I_{\text{run}}^{\text{GDH}}(\nu_{\text{max}}) = \int_{\nu_0}^{\nu_{\text{max}}} \frac{d\nu}{\nu} [\sigma_{3/2}(\nu) - \sigma_{1/2}(\nu)], \quad (5.53)$$

with  $\nu_0$  being the lowest particle-production threshold, effectively set by the pion-production threshold  $\nu_\pi = m_\pi + (m_\pi^2 + Q^2)/(2M)$ , evaluates to [211]:

$$I_{\text{run}}^{\text{GDH}}(2.9 \text{ GeV}) = 226 \pm 5_{\text{stat}} \pm 12_{\text{syst}} \mu\text{b}, \quad (5.54)$$

where the unmeasured low-energy region is covered by MAID [209] and SAID [210] analyses. The extrapolated result,

$$I_{\text{run}}^{\text{GDH}}(\infty) = 212 \pm 6_{\text{stat}} \pm 16_{\text{syst}} \mu\text{b}, \quad (5.55)$$

is in agreement with the GDH sum rule value (obtained by substituting the proton anomalous magnetic moment):  $205 \mu\text{b}$ . The negative contribution to the integrand at higher energies is supported by a Regge parametrization of the polarized data, as well as by fits of deep-inelastic scattering (DIS) data [218, 219].

The neutron cross section is extracted from the difference of deuteron and proton cross sections, see Arenhovel [220] for critical discussion. Presently, the GDH integral for the neutron is estimated to be  $225 \mu\text{b}$ , which compares well to the sum rule value of  $233 \mu\text{b}$ . Table 5.2 summarizes the GDH sum rule results for the proton and neutron.

In future, one would like to measure the neutron cross sections based on  $^3\text{He}$  targets. Since the proton spins are paired in the ground state, a polarized  $^3\text{He}$  target is a good alternative to the non-existent free neutron target. The neutron spin structure is quite similar to the one of  $^3\text{He}$ . Therefore, in contrast to deuterium, the magnetic moment of  $^3\text{He}$  is comparable to that of the neutron, with the GDH integral equal to:  $-496 \mu\text{b}$ . Below the pion-production threshold, the dominant channel is the two- and three-body breakup reactions:  $^3\text{He}(\vec{\gamma}n)d$  and  $^3\text{He}(\vec{\gamma}n)pp$ . The latter has been experimentally accessed at HIGS [221]. At MAMI, the helicity-dependent total inclusive  $^3\text{He}$  cross section is measured with circularly polarized photons in the energy range:  $200 < \nu < 500 \text{ MeV}$  [222]. An estimate of the GDH sum rule for the neutron based on  $^3\text{He}$  experiments has not yet been done.

## 6. Proton Structure in (Muonic) Hydrogen

An exciting development in the field of nucleon structure has come recently from atomic physics. The CREMA collaboration discovery of the  $2P - 2S$  transitions in muonic hydrogen ( $\mu\text{H}$ ) has led to a precision measurement of the proton charge radius [24, 25]. The resulting value is an order of magnitude more precise than that from hydrogen spectroscopy (H) or electron-proton ( $ep$ ) scattering. It also turned out to be substantially ( $7\sigma$ ) different from the CODATA value [223], which had been the standard value based on H and  $ep$  scattering. The latter discrepancy is known as the *proton-radius puzzle* (see Sect. 7.3 for more details and references).

In this section we examine the proton structure effects in hydrogen-like atoms. While all the following formulae are applicable to both H and  $\mu\text{H}$ , the numerics will only be worked out for  $\mu\text{H}$ . As far as proton structure is concerned, all the effects are much more pronounced in  $\mu\text{H}$ .<sup>15</sup> The proton charge radius, for example, is the second largest contribution to the  $\mu\text{H}$  Lamb shift (after the vacuum polarization due to the electron loop in QED), cf. Fig. 6.1.

The proton structure effects are naturally divided into two categories:

- (i) Finite-size (or ‘elastic’) effects, i.e., the effect of the elastic FFs,  $G_E$  and  $G_M$ .
- (ii) Polarizability<sup>16</sup> (or ‘inelastic’) effects, which basically is everything else.<sup>17</sup>

Assuming the proton e.m. structure is confined within a femtometer radius, the finite-size effects can be expanded in the moments of charge and magnetization distributions,  $\rho_E(r)$  and  $\rho_M(r)$ , which are the Fourier transforms of the elastic FFs  $G_E$  and  $G_M$ , respectively. To  $O(\alpha^5)$ , the finite-size effects in the hydrogen Lamb shift and hyperfine splitting (HFS) are found as (omitting recoil) [224]:

$$E_{\text{LS}} \equiv E(2P_{1/2}) - E(2S_{1/2}) = -\frac{Z\alpha}{12a^3} [R_E^2 - (2a)^{-1} R_F^3] + O(\alpha^6), \quad (6.1a)$$

$$E_{\text{HFS}}(nS) \equiv E(nS_{1/2}^{F=1}) - E(nS_{1/2}^{F=0}) = E_F(nS) [1 - 2a^{-1} R_Z] + O(\alpha^6), \quad (6.1b)$$

where  $a = 1/(Z\alpha m_r)$  is the Bohr radius,  $Z$  is the nuclear charge ( $Z = 1$  for the proton),  $E_F$  is the Fermi energy of the  $nS$ -level:

$$E_F(nS) = \frac{8Z\alpha}{3a^3} \frac{1 + \kappa}{mM} \frac{1}{n^3}, \quad (6.2)$$

and the radii are defined as follows (for other notations, see Sect. 1.1):

- Charge radius (shorthand for the root-mean-square (rms) radius of the charge distribution):

$$R_E = \sqrt{\langle r^2 \rangle_E}, \quad \langle r^2 \rangle_E \equiv \int d\mathbf{r} r^2 \rho_E(\mathbf{r}) = -6 \frac{d}{dQ^2} G_E(Q^2) \Big|_{Q^2=0}; \quad (6.3a)$$

- Friar radius (or, the 3<sup>rd</sup> Zemach moment):

$$R_F = \sqrt[3]{\langle r^3 \rangle_{E(2)}}, \quad \langle r^3 \rangle_{E(2)} \equiv \frac{48}{\pi} \int_0^\infty \frac{dQ}{Q^4} \left[ G_E^2(Q^2) - 1 + \frac{1}{3} R_E^2 Q^2 \right]; \quad (6.3b)$$

- Zemach radius:

$$R_Z \equiv -\frac{4}{\pi} \int_0^\infty \frac{dQ}{Q^2} \left[ \frac{G_E(Q^2) G_M(Q^2)}{1 + \kappa} - 1 \right]. \quad (6.3c)$$

A derivation of these formulae will be given in Sect. 6.2.

The proton polarizability effects begin to contribute at order  $(Z\alpha)^5 m_r^4$ . The usual way of calculating these effects is through the two-photon exchange (TPE) diagram, see Sect. 6.3. The elastic effects beyond the charge radius (i.e., the contributions of Friar and Zemach radii), together with some recoil corrections, are sometimes referred to as the ‘elastic TPE’. Therefore the TPE effect is split into the ‘elastic’ and ‘polarizability’ contribution (see, e.g., Fig. 6.1).

<sup>15</sup> In layman’s terms, because the Bohr radius of  $\mu\text{H}$  is about 200 times smaller than that of H, the muon comes much closer to the proton, thus having a “better view” (or, more precisely, spending considerably more time “inside the proton”, thus “feeling” less Coulomb attraction).

<sup>16</sup> In the literature *polarizability* is sometimes called *polarization*. We prefer to reserve the latter for the proton spin polarization.

<sup>17</sup> In exceptional cases, ‘inelastic’ may refer to only a part of the polarizability effect, as explained in Sect. 6.4.1.



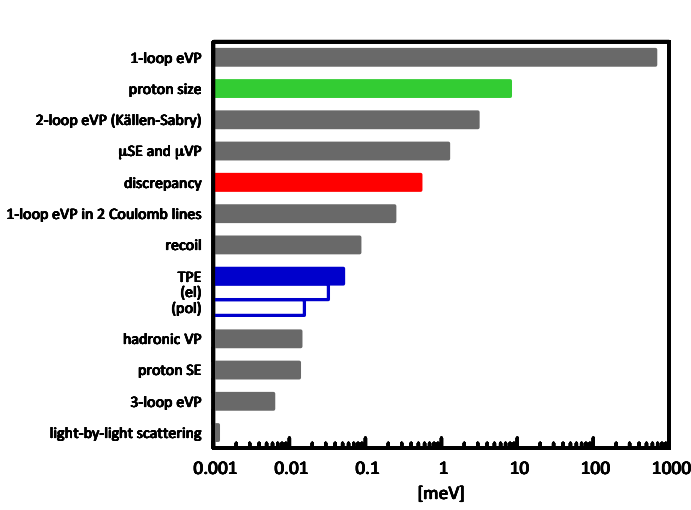


Figure 6.1: The budget of the  $\mu\text{H}$  Lamb shift [225]. The TPE is displayed in blue; we give estimates for the elastic and polarizability contributions (unfilled bars), as well as for the total TPE contribution (solid bar). The proton radius discrepancy (shown in red) amounts to 0.31 meV. The theoretical uncertainty is estimated as 0.0025 meV, cf. Eq. (6.6a).

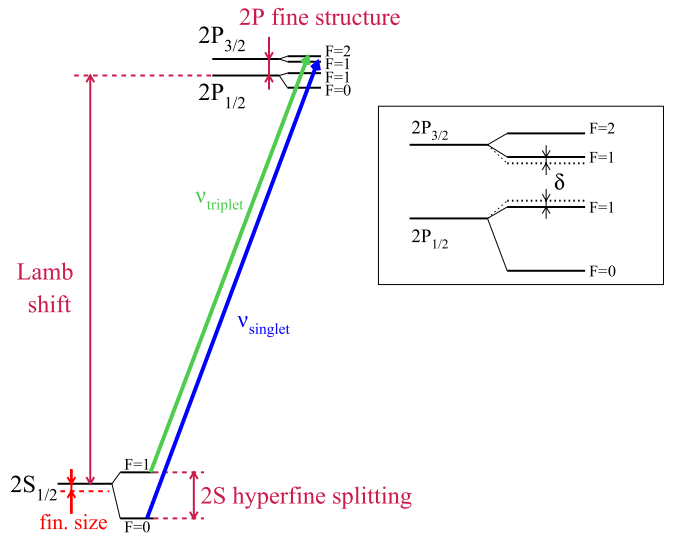


Figure 6.2:  $2S$  and  $2P$  energy levels in  $\mu\text{H}$ . The two measured transition frequencies,  $\nu_t$  [24] and  $\nu_s$  [25], are indicated together with the Lamb shift, fine and hyperfine structure, and finite-size effects. The main figure is drawn to scale. The inset zooms in on the  $2P$  states. Here, the mixing of the  $2P^{F=1}$ -levels shifts them by  $\pm\delta$ . Plot courtesy of Aldo Antognini.

### 6.1. Charge and Zemach Radii from Muonic Hydrogen

Figure 6.2 shows the  $n = 2$  energy-level scheme of  $\mu\text{H}$  and the measured transitions, i.e.:

$$h\nu_t = E(2P_{3/2}^{F=2}) - E(2S_{1/2}^{F=1}), \quad (6.4a)$$

$$h\nu_s = E(2P_{3/2}^{F=1}) - E(2S_{1/2}^{F=0}). \quad (6.4b)$$

The obtained experimental values for the Lamb shift and the HFS [24, 25, 225],

$$E_{\text{LS}}^{\text{exp}} = 1/4 h\nu_s + 3/4 h\nu_t - E_{\text{FS}}(2P) - 1/8 E_{\text{HFS}}(2P_{3/2}) - 1/4 \delta = 202.3706(23) \text{ meV}, \quad (6.5a)$$

$$E_{\text{HFS}}^{\text{exp}}(2S) = h\nu_s - h\nu_t + E_{\text{HFS}}(2P_{3/2}) - \delta = 22.8089(51) \text{ meV}, \quad (6.5b)$$

thus rely on the theoretical calculation of the fine and hyperfine splittings of the  $2P$ -levels [226]:

- $2P$  fine structure splitting:  $E_{\text{FS}}(2P) = 8.352082 \text{ meV}$ ,
- $2P_{3/2}$  hyperfine structure splitting:  $E_{\text{HFS}}(2P_{3/2}) = 3.392588 \text{ meV}$ ,
- $2P^{F=1}$  level mixing:  $\delta = 0.14456 \text{ meV}$ .

Furthermore, the extraction of charge and Zemach radii from  $\mu\text{H}$  relies on the following theoretical description of the  $(2P - 2S)$  Lamb shift and the  $2S$  HFS [225] (in units of meV):

$$E_{\text{LS}}^{\text{th}} = 206.0336(15) - 5.2275(10) (R_E/\text{fm})^2 + E_{\text{LS}}^{\text{TPE}}, \quad \text{with } E_{\text{LS}}^{\text{TPE}} = 0.0332(20), \quad (6.6a)$$

$$E_{\text{HFS}}^{\text{th}}(2S) = 22.9763(15) - 0.1621(10) (R_Z/\text{fm}) + E_{\text{HFS}}^{\text{pol}}(2S), \quad \text{with } E_{\text{HFS}}^{\text{pol}}(2S) = 0.0080(26), \quad (6.6b)$$

where  $E_{\text{LS}}^{\text{TPE}}$  contains the Friar radius, recoil finite-size effects, and the polarizability effects;  $E_{\text{HFS}}^{\text{pol}}(2S)$  is the HFS polarizability effect only. The precise numerical values of these TPE effects will be considered in Sect. 6.4. For review of the QED effects we refer to Refs. [224, 227, 228].

Fitting the theory to experiment thus allows one to extract both the proton charge radius:  $R_E = 0.84087(39)$  fm, and the Zemach radius:  $R_Z = 1.082(37)$  fm.<sup>18</sup> One caveat here, as pointed out by Karshenboim [231, 232], is that this extraction relies on the Friar radius obtained from empirical FFs, which in turn have a different  $R_E$  than extracted from the  $\mu$ H Lamb shift. This issue will be discussed in Sect. 6.2.2.

## 6.2. Finite-Size Effects by Dispersive Technique

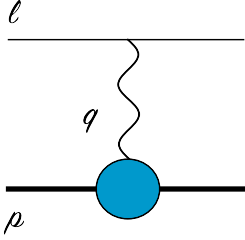


Figure 6.3: One-photon exchange graph with nucleon FFs, giving rise to FSE.

The usual derivation of the finite-size effects (FSE) is done in terms of the charge and magnetization densities (see, e.g., Friar [233]), which makes it difficult to derive the relativistic corrections. We choose a different path [234] and derive the Breit potential from the manifestly Lorentz-invariant expression for the Feynman diagram of Fig. 6.3, with the e.m. vertex of the nucleus given by:<sup>19</sup>

$$\Gamma^\mu = Ze\gamma^\mu F_1(Q^2) - \frac{Ze}{2M}\gamma^{\mu\nu}q_\nu F_2(Q^2). \quad (6.7)$$

The Dirac and Pauli FFs are then assumed to fulfill the once-subtracted DRs:

$$\begin{pmatrix} F_1(Q^2) \\ F_2(Q^2) \end{pmatrix} = \begin{pmatrix} 1 \\ \kappa \end{pmatrix} - \frac{Q^2}{\pi} \int_{t_0}^{\infty} \frac{dt}{t(t+Q^2)} \text{Im} \begin{pmatrix} F_1(t) \\ F_2(t) \end{pmatrix}, \quad (6.8)$$

with  $t_0$  being the lowest particle-production threshold. The use of the DRs makes the rest of the derivation to be very much analogous to Schwinger's method of calculating the Uehling (vacuum polarization) effect [235]. The Breit potential for the Uehling effect was considered in, e.g., Refs. [227, 236].

At leading order (in  $1/c$ ) we obtain the following terms for the Breit potential in momentum space:

$$V_{\text{eFF}}(Q) = 4Z\alpha \int_{t_0}^{\infty} \frac{dt}{t} \frac{\text{Im} G_E(t)}{t+Q^2}, \quad (6.9a)$$

$$V_{\text{mFF}}^{l=0}(Q) = \frac{4\pi Z\alpha}{3mM} [F(F+1) - \frac{3}{2}] \left\{ 1 + \kappa - \frac{Q^2}{\pi} \int_{t_0}^{\infty} \frac{dt}{t} \frac{\text{Im} G_M(t)}{t+Q^2} \right\}, \quad (6.9b)$$

where the magnetic (spin-dependent) part is only given for the  $S$ -states ( $l = 0$ ). The imaginary part (discontinuity along the branch cuts) of the electric and magnetic Sachs FFs is straightforwardly related to the one of Dirac and Pauli FFs:

$$\text{Im} G_E(t) = \text{Im} F_1(t) + \frac{t}{(2M)^2} \text{Im} F_2(t), \quad (6.10a)$$

$$\text{Im} G_M(t) = \text{Im} F_1(t) + \text{Im} F_2(t). \quad (6.10b)$$

The potential in coordinate space is obtained via Fourier transform,

$$V(r) = \frac{4\pi}{(2\pi)^3 r} \int_0^{\infty} dQ Q V(Q) \sin Qr, \quad (6.11)$$

with the following result:

$$V_{\text{eFF}}(r) = \frac{Z\alpha}{\pi r} \int_{t_0}^{\infty} \frac{dt}{t} e^{-r\sqrt{t}} \text{Im} G_E(t), \quad (6.12a)$$

$$V_{\text{mFF}}^{l=0}(r) = \frac{4\pi Z\alpha}{3mM} [F(F+1) - \frac{3}{2}] (1 + \kappa) \rho_M(r), \quad (6.12b)$$

<sup>18</sup>The first  $\mu$ H measurement [24] had only determined  $\nu_t$ , and hence needed theory input for the  $2S$  HFS too:  $E_{\text{HFS}}(2S) = 22.8148(78)$  meV [229] (using  $R_Z = 1.022$  fm [230]).

<sup>19</sup>Here we introduce the e.m. FFs of a spin-1/2 nucleus. For hydrogen they are of course identical to the proton FFs. The Compton scattering formalism of the previous sections is applicable to spin-1/2 nuclei with  $Z > 1$ , provided we replace the FFs as:  $F_i \rightarrow ZF_i$ , and set  $F_1(0) = 1$ ,  $F_2(0) = \kappa$ , rather than  $Z, \kappa$  of the nucleon case. Likewise, we replace the structure functions:  $f_i \rightarrow Z^2 f_i$ ,  $g_i \rightarrow Z^2 g_i$ .

where the magnetization density  $\rho_M$  (the Fourier transform of  $G_M$ ) is a Laplace-type of transform of  $\text{Im } G_M$ :

$$\rho_M(r) = \frac{1}{(2\pi)^2 r} \int_{t_0}^{\infty} dt \frac{\text{Im } G_M(t)}{1 + \kappa} e^{-r\sqrt{t}}. \quad (6.13)$$

The latter definition shows explicitly that a spherically symmetric density is a Lorentz invariant quantity. An analogous definition, but in terms of  $\text{Im } G_E$ , applies to the charge density  $\rho_E(r)$ .

The FF effect can now be worked out using time-independent perturbation theory. For example, the energy shift of the  $nl$ -level due to a spherically symmetric correction  $V_\delta(r)$  to the Coulomb potential  $V_C(r) = -Z\alpha/r$  is to 1<sup>st</sup> order given by:

$$E_{nl}^{(\delta)} \equiv \langle nlm | V_\delta | nlm \rangle = \frac{1}{2\pi^2} \int_0^\infty dQ Q^2 w_{nl}(Q) V_\delta(Q) = \int_0^\infty dr r^2 R_{nl}^2(r) V_\delta(r), \quad (6.14)$$

where the momentum-space expression contains the convolution of the momentum-space wave functions,

$$w_{nl}(Q) = \int d\mathbf{p} \varphi_{nlm}^*(\mathbf{p} + \mathbf{Q}) \varphi_{nlm}(\mathbf{p}), \quad (6.15)$$

while the coordinate-space one contains the radial wave functions  $R_{nl}(r)$ . The explicit forms of the wave functions can be found in, e.g., Bethe and Salpeter [237]. For completeness we give here the expressions for  $1S$ ,  $2S$ , and  $2P$  states:

$$\begin{aligned} R_{10}(r) &= \frac{2}{a^{3/2}} e^{-r/a}, & w_{1S}(Q) &= \frac{16}{(4 + (aQ)^2)^2}, \\ R_{20}(r) &= \frac{1}{\sqrt{2} a^{3/2}} \left(1 - \frac{r}{2a}\right) e^{-r/2a}, & w_{2S}(Q) &= \frac{(1 - (aQ)^2)(1 - 2(aQ)^2)}{(1 + (aQ)^2)^4}, \\ R_{21}(r) &= \frac{1}{\sqrt{3} (2a)^{3/2}} \frac{r}{a} e^{-r/2a}, & w_{2P}(Q) &= \frac{1 - (aQ)^2}{(1 + (aQ)^2)^4}. \end{aligned} \quad (6.16)$$

For the following discussions it is useful to note the asymptotic behavior of  $w$  for large  $Q$ :

$$w_{nS}(Q) \stackrel{Q \rightarrow \infty}{\sim} \frac{16\pi}{aQ^4} \phi_n^2, \quad (6.17)$$

where  $\phi_n = 1/\sqrt{\pi a^3 n^3}$  is the coordinate-space wave function at the origin,  $r = 0$ .

### 6.2.1. Lamb Shift

Consider first the correction due to the electric FF ( $G_E$ ), as given by Eq. (6.12a). At 1<sup>st</sup> order, it yields the following correction to the  $2P - 2S$  Lamb shift:

$$E_{\text{LS}}^{(\text{eFF})} = -\frac{Z\alpha}{2\pi a^3} \int_{t_0}^{\infty} dt \frac{\text{Im } G_E(t)}{(\sqrt{t} + Z\alpha m_r)^4}, \quad (6.18a)$$

$$= -\frac{\pi Z\alpha}{3a^3} \int_0^\infty dr r^4 e^{-r/a} \rho_E(r), \quad (6.18b)$$

$$= -\frac{Z\alpha}{12a^3} \sum_{k=0}^{\infty} \frac{(-Z\alpha m_r)^k}{k!} \langle r^{k+2} \rangle_E = -\frac{(Z\alpha)^4 m_r^3}{12} \left( \langle r^2 \rangle_E - Z\alpha m_r \langle r^3 \rangle_E \right) + \dots, \quad (6.18c)$$

where in the last steps we have expanded in the moments of the charge distribution:

$$\langle r^N \rangle_E \equiv 4\pi \int_0^\infty dr r^{N+2} \rho_E(r) = \frac{(N+1)!}{\pi} \int_{t_0}^{\infty} dt \frac{\text{Im } G_E(t)}{t^{N/2+1}}. \quad (6.19)$$

One should keep in mind though that the expansion in moments is not necessarily convergent. For instance, Eq. (6.18a) tells us that the expansion is applicable when the nearest particle-production threshold is well above the inverse Bohr radius, i.e.:  $Z\alpha m_r \ll \sqrt{t_0}$ .

Incidentally, one of the early proposals for solving the proton-radius puzzle [238] does not work out precisely because the expansion in moments is not applicable for the choice of  $\rho_E$  proposed therein. The fine-tuning of  $\rho_E$  affected mainly the region  $r > a$ , enhancing the Friar radius by almost a factor of 3, and thus achieving a huge impact on the Lamb shift, according to Eq. (6.1a). On the other hand, according to the exact formula (6.18b), the region above the Bohr radius makes a negligible impact on the Lamb shift, which was verified explicitly by us [234] for the model of Ref. [238].

It is also useful to have an expression in terms of  $G_E$  itself:

$$E_{\text{LS}}^{\langle \text{eFF} \rangle} = -\frac{2Z\alpha}{\pi} \int_0^\infty dQ w_{2P-2S}(Q) G_E(Q^2), \quad \text{with } w_{2P-2S}(Q) = 2(Z\alpha m_r)^4 Q^2 \frac{(Z\alpha m_r)^2 - Q^2}{[(Z\alpha m_r)^2 + Q^2]^4}. \quad (6.20)$$

Using the expression for the weighting function,  $w$ , in terms of the wave functions, cf. Eq. (6.15), it is easy to see that for  $G_E(Q^2) = \text{const}$  the effect vanishes. That is, the charge normalization drops out. Note also that this FF effect is still of  $O(\alpha^4)$ , despite the  $O(\alpha^5)$  overall prefactor. The naive expansion of  $w$  in  $\alpha$  does not work, as the resulting integral is infrared divergent. As seen below more explicitly, this infrared enhancement yields in the end the correct charge radius contribution of  $O(\alpha^4)$ .

To complete the derivation of the standard formulae for the FSE in the Lamb shift to  $O(\alpha^5)$ , we take the potential to the 2<sup>nd</sup> order in perturbation theory. The 2<sup>nd</sup>-order contribution at  $O(\alpha^5)$  comes from the continuum states only and amounts to:

$$E_{\text{LS}}^{\langle \text{eFF} \rangle \langle \text{eFF} \rangle} = \frac{Z\alpha}{a^4} \frac{2}{\pi} \int_0^\infty \frac{dQ}{Q^4} [G_E(Q^2) - 1]^2 + O(\alpha^6) = -\frac{Z\alpha}{12a^4} \left[ \langle r^3 \rangle_E - \frac{1}{2} \langle r^3 \rangle_{E(2)} \right] + O(\alpha^6). \quad (6.21)$$

Adding this result to the  $O(\alpha^5)$  term from the 1<sup>st</sup> order, Eq. (6.18c), we can see that the 2<sup>nd</sup>-order effect replaces the 3<sup>rd</sup> charge radius  $\langle r^3 \rangle_E$  by the 3<sup>rd</sup> Zemach moment  $\langle r^3 \rangle_{E(2)}$ , resulting in Eq. (6.1a).

### 6.2.2. Consistency of the Charge Radius Extraction

The consistency problem, recently addressed by Karshenboim [231], is basically that *in order to compute the Friar radius (6.3b), and hence its contribution to the Lamb shift (6.1a), one must know the charge radius  $R_E$ , which in turn needs to be extracted from the Lamb shift*. Presently the  $\mu\text{H}$  extraction of  $R_E$  uses as input the value of  $R_F$  obtained from the empirical FF, which has a different  $R_E$ . This obviously is not consistent and leads to a systematic uncertainty.

To see the origin of this problem, let us examine the exact (unexpanded in moments) FSE to 2<sup>nd</sup> order in perturbation theory:

$$E_{\text{LS}}^{\text{FSE}} \equiv E_{\text{LS}}^{\langle \text{eFF} \rangle} + E_{\text{LS}}^{\langle \text{eFF} \rangle \langle \text{eFF} \rangle} = -\frac{Z\alpha}{\pi} \int_0^\infty dQ w_{2P-2S}(Q) G_E^2(Q^2), \quad (6.22)$$

where the weighting function is given in Eq. (6.20). This form clearly shows that the Lamb shift is a functional of the FF. Ideally, one needs to find  $G_E$  which fits the  $ep$  and atomic data simultaneously. This, however, has not yet been realized.

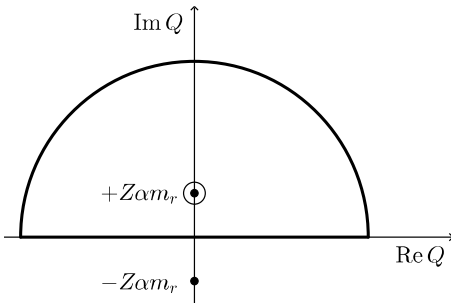


Figure 6.4: Poles of  $w_{2l}$ , and the contour in the complex  $Q$  plane.

Let us evaluate the integral by the residue method. For this we consider the complex  $Q$  plane, Fig. 6.4. The poles of  $w(Q)$  are at

$$Q = \pm i Z\alpha m_r. \quad (6.23)$$

The singularities of  $G_E(Q^2)$  also lie on the imaginary axis, since it obeys the DR of the type (6.8), see Eq. (C.5). The integrand is even in  $Q$  and hence we may extend the integration to negative  $Q$ . We then close the contour in the upper half-plane, use the residue theorem, and neglect the integral over the big semicircle to arrive at

$$\int_0^\infty dQ w(Q) G_E^2(Q^2) = \pi i \text{Res}[w(Q) G_E^2(Q^2)]_{Q=iZ\alpha m_r} + \dots, \quad (6.24)$$

where the dots stand for the residue of  $G_E$  poles. Those can be computed using the DR or an explicit ansatz (e.g., an empirical parametrization) for  $G_E$ . When using the DR of (C.5) one simply obtains the Friar radius contribution written in terms of  $\text{Im } G_E$ , cf. Eq. (C.8).

The residue over the pole of  $w$  evaluates to:

$$\text{Res}[w(Q) g(Q^2)]_{Q=iZ\alpha m_r} = i(Z\alpha m_r)^3 [1/4 g'(Q^2) + Q^2 g''(Q^2) + 1/3 Q^4 g'''(Q^2)]_{Q^2=-(Z\alpha m_r)^2}, \quad (6.25)$$

where we have introduced for a moment  $g \equiv G_E^2$ , and the primes denote the derivatives over  $Q^2$ . Obviously, the first term dominates (lowest in  $\alpha$ ) and yields the usual  $R_E^2$  contribution of  $O((Z\alpha)^4 m_r^3)$ , cf. Eq. (6.1a).

It is interesting to observe that Eq. (6.25) is only dependent on the derivatives of  $G_E$ , and thus does not involve any of the odd moments, which are integrals of  $G_E$ , see Eq. (C.7). The contribution of odd moments, and in particular the one of the Friar radius, comes from the singularities of  $G_E$ . Thus, the consistency problem in question is absent if the rms charge radius and the poles of  $G_E$  are *uncorrelated*. We, however, are not aware at the moment of an empirical parametrization in which the charge radius and the poles are not correlated. Quite the opposite, the correlation is usually strong. The simplest example is provided by the dipole form,  $G_E(Q^2) = (1 + Q^2/\Lambda^2)^{-2}$ . Both the radius and the pole positions are given by the mass parameter  $\Lambda$ : the radius is  $12/\Lambda^2$ , while the pole is at  $Q = \pm i\Lambda$ . An empirical parametrization with weak correlation between the value of  $G_E'(0)$  and the position of its poles would be preferred from this point of view.

General constraints on the FF parametrizations have recently been discussed at length by Sick et al. [239–242]. One finds in particular that certain parametrizations have unphysical poles which result in weird charge or magnetization distributions. To take the advantage of studying the  $r$ -space simultaneously, it has been suggested to parametrize the FF in a basis with analytic Fourier transform, e.g., with a sum of Gaussians. It would be interesting to see if these kind of parametrizations lead to weaker correlation between the rms radius and the FF poles.

### 6.2.3. Hyperfine Splitting

The HFS, introduced in Eq. (6.1b), receives at first only the magnetic contribution:

$$E_{\text{HFS}}^{\langle m\text{FF} \rangle}(nS) = \frac{4Z\alpha}{3\pi mM} \int_0^\infty dQ Q^2 w_{nS}(Q) G_M(Q^2), \quad (6.26a)$$

$$= \frac{8\pi Z\alpha}{3mM} (1 + \kappa) \int_0^\infty dr r^2 R_{n0}^2(r) \rho_M(r), \quad (6.26b)$$

where  $w_{nS}$  is given by Eq. (6.15). Setting in this expression  $G_M = 1 + \kappa$ , or equivalently  $\rho_M(r) = \delta(r)/4\pi r^2$ , yields the Fermi energy,  $E_F(nS)$ , given in Eq. (6.2). Here, the expansion in  $\alpha$  works straightforwardly (we can expand under the integrals), and we obtain:

$$\frac{E_{\text{HFS}}^{\langle m\text{FF} \rangle}(nS)}{E_F(nS)} = 1 - \frac{2}{a} \langle r \rangle_M + O(\alpha^2), \quad (6.27)$$

where the first moment of  $\rho_M(r)$  can equivalently be written as:

$$\langle r \rangle_M = -\frac{4}{\pi} \int_0^\infty \frac{dQ}{Q^2} \left[ \frac{G_M(Q^2)}{1 + \kappa} - 1 \right]. \quad (6.28)$$

At the 2<sup>nd</sup> order in perturbation theory, we obtain the interference between the potentials of the electric and magnetic term:

$$\frac{E_{\text{HFS}}^{\langle e\text{FF} \rangle \langle m\text{FF} \rangle}(nS)}{E_F(nS)} = \frac{8}{a\pi} \int_0^\infty \frac{dQ}{Q^2} [G_E(Q^2) - 1] \frac{G_M(Q^2)}{1 + \kappa} + O(\alpha^2). \quad (6.29)$$

Adding up the 1<sup>st</sup>- and 2<sup>nd</sup>-order contributions, we obtain the well-known FSE in the HFS given by Eq. (6.1b).

Taking  $V_{m\text{FF}}^{l=0}$  to 2<sup>nd</sup> order gives rise to  $E^{\langle m\text{FF} \rangle \langle m\text{FF} \rangle}$ , which is a higher-order recoil effect. This, and some other, recoil effects are treated more properly within the approach we consider next.

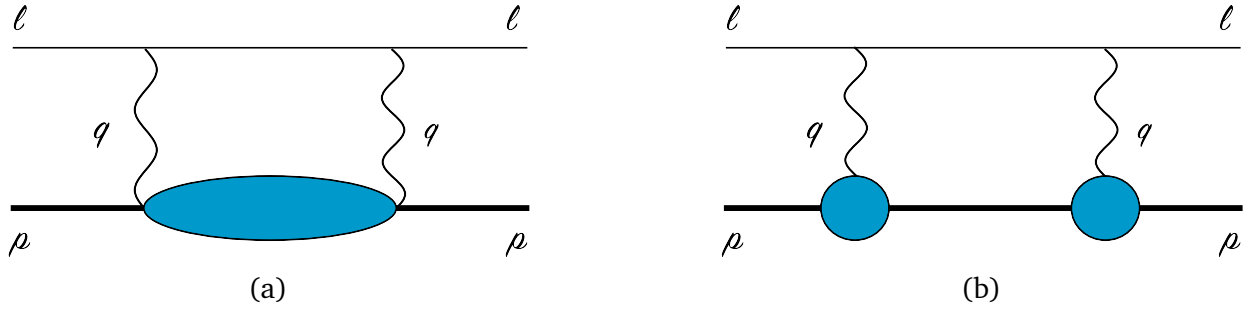


Figure 6.5: (a) TPE diagram in forward kinematics: the horizontal lines correspond to the lepton and the proton (bold), where the ‘blob’ represents all possible excitations. (b) Elastic contribution to the TPE. The crossed diagrams are not drawn.

### 6.3. Structure Effects through Two-Photon Exchange

Having obtained the standard FSE of (6.1) using the Breit potential, we consider here a different approach. We consider the correction, to the Coulomb potential, due to the TPE, see Fig. 6.5 (a). A great advantage of this approach is that one can access the inelastic effects of the proton structure [243, 244]. On the other hand, it is less systematic and cannot be used without matching to a systematic expansion. We shall only use it to 1<sup>st</sup>-order perturbation theory and match the elastic part, Fig. 6.5 (b), with the FSE derived from the Breit potential.

Let us note right away that the TPE contains an iteration of the Coulomb potential present in the wave functions. However, we need not to worry about the double-counting. The Coulomb interaction by itself is harmless, as it gives no contribution to the Lamb shift or HFS.

To  $O(\alpha^5)$  it will be sufficient to evaluate the TPE amplitude at zero energy ( $p \cdot \ell = mM$ ) and momentum transfer ( $t = 0$ ). The resulting amplitude yields a constant potential in momentum space, which of course translates to a  $\delta$ -function potential in coordinate space. The energy shift is thus proportional to the wave-function at the origin, and hence only the  $S$ -levels are affected.

The forward TPE amplitude is a one-loop integral involving the doubly-virtual Compton scattering (VVCS) amplitude. The latter has been discussed in Sect. 5. According to Eq. (5.1), its tensor structure decomposes into a symmetric, spin-independent part parametrized by the scalar amplitudes  $T_{1,2}(\nu, Q^2)$ , and an antisymmetric, spin-dependent part parametrized by  $S_{1,2}(\nu, Q^2)$ . The HFS obviously depends on the latter, while the Lamb shift depends on the former.

More specifically, the shift of the  $nS$ -level is given by:

$$\Delta E(nS) = 8\pi\alpha m \phi_n^2 \frac{1}{i} \int_{-\infty}^{\infty} \frac{d\nu}{2\pi} \int \frac{d\mathbf{q}}{(2\pi)^3} \frac{(Q^2 - 2\nu^2) T_1(\nu, Q^2) - (Q^2 + \nu^2) T_2(\nu, Q^2)}{Q^4(Q^4 - 4m^2\nu^2)}, \quad (6.30)$$

with  $\phi_n^2 = 1/(\pi n^3 a^3)$  the wave function squared at the origin, and  $\nu = q_0$ ,  $Q^2 = \mathbf{q}^2 - q_0^2$ . The correction to the HFS is given by:

$$\frac{E_{\text{HFS}}(nS)}{E_F(nS)} = \frac{4m}{\mu} \frac{1}{i} \int_{-\infty}^{\infty} \frac{d\nu}{2\pi} \int \frac{d\mathbf{q}}{(2\pi)^3} \frac{1}{Q^4 - 4m^2\nu^2} \left\{ \frac{(2Q^2 - \nu^2)}{Q^2} S_1(\nu, Q^2) + 3 \frac{\nu}{M} S_2(\nu, Q^2) \right\}. \quad (6.31)$$

To proceed further, one performs a Wick rotation, i.e. changes the integration over  $q_0$  to  $Q_0 = -iq_0$ . Note that this is only possible at vanishing external energy (threshold) of lepton-proton scattering. At finite energy one needs to take care of the poles moving across the imaginary  $q_0$  axis (see, e.g., Ref. [245]).

After the Wick rotation, the integration four-momentum is Euclidean and we can evaluate it in hyperspherical coordinates,

$$Q^\mu = Q(\cos \chi, \sin \chi \sin \theta \cos \varphi, \sin \chi \sin \theta \sin \varphi, \sin \chi \cos \theta).$$

The integrals over  $\theta$  and  $\varphi$  can be done right away, yielding a factor of  $4\pi$ . The integral over  $\nu = iQ \cos \chi$  can be done after substituting the DRs for the VVCS amplitudes, Eq. (5.12). Introducing the ‘lepton velocity’



$v_l = \sqrt{1 + 4m^2/Q^2}$ , we obtain the following expression for the  $S$ -level shift:

$$\begin{aligned} \Delta E(nS) &= \frac{16(Z\alpha)^2 m}{M} \phi_n^2 \int_0^\infty \frac{dQ}{Q^3} \int_0^1 dx \frac{1}{v_l + \sqrt{1 + x^2 \tau^{-1}}} \\ &\times \left\{ \frac{f_1(x, Q^2)}{x} - \frac{f_2(x, Q^2)}{2\tau} + \frac{1}{(1 + v_l)(1 + \sqrt{1 + x^2 \tau^{-1}})} \left( \frac{2f_1(x, Q^2)}{x} + \frac{f_2(x, Q^2)}{2\tau} \right) \right\}, \end{aligned} \quad (6.32)$$

and the HFS:

$$\begin{aligned} \frac{E_{\text{HFS}}(nS)}{E_F(nS)} &= \frac{16Z\alpha m M}{\pi(1 + \kappa)} \int_0^\infty \frac{dQ}{Q^3} \int_0^1 dx \frac{1}{v_l + \sqrt{1 + x^2 \tau^{-1}}} \\ &\times \left\{ \left[ 1 + \frac{1}{2(v_l + 1)(1 + \sqrt{1 + x^2 \tau^{-1}})} \right] 2g_1(x, Q^2) + 3g_2(x, Q^2) \right\}. \end{aligned} \quad (6.33)$$

These are the master formulae containing all the structure effects to  $O(\alpha^5)$ . One ought to be careful though in matching the contribution of the elastic structure functions (5.7) to the standard FSE of (6.1). In the non-relativistic (heavy-mass) limit we obtain:<sup>20</sup>

$$\Delta E^{\text{el}}(nS) = -16(Z\alpha)^2 m_r \phi_n^2 \int_0^\infty \frac{dQ}{Q^4} G_E^2(Q^2), \quad (6.34a)$$

$$E_{\text{HFS}}^{\text{el}}(nS) = \frac{64(Z\alpha)^2 m_r}{3mM} \phi_n^2 \int_0^\infty \frac{dQ}{Q^2} G_M(Q^2) G_E(Q^2). \quad (6.34b)$$

The correct matching is achieved by regularizing the infrared divergencies with the convoluted wave functions, i.e.,  $w(Q)$  in Eq. (6.15). For example, to obtain the charge radius contribution to the  $2P - 2S$  Lamb shift one should replace  $\phi_n^2$  in Eq. (6.34a) with:  $-aw_{2P-2S}(Q) Q^4/16\pi$ . For the HFS, the replacement in Eq. (6.34b) is:  $\phi_n^2 \rightarrow aw_{nS}(Q) Q^4/16\pi$ , yielding the correct Fermi energy and Zemach radius contributions. The infrared-safe contributions, such as the recoil and polarizability corrections, need no regularization. In what follows we only consider those kind of contributions.

## 6.4. Empirical Evaluations

### 6.4.1. Lamb Shift

The  $O(\alpha^5)$  effects of proton structure in the Lamb shift are usually divided into the effect of (i) the Friar radius, (ii) finite-size recoil, and (iii) polarizabilities. The first two are sometimes combined into (i') the 'elastic' TPE contribution. The 'polarizability' effect is often split between (ii') the 'inelastic' TPE and (iii') a 'subtraction' term, i.e., the contribution of  $\bar{T}_1(0, Q^2)$ .

The elastic and inelastic TPE contributions are well-constrained by the available empirical information on, respectively, the proton FFs and unpolarized structure functions, whereas the subtraction contribution must be modeled. It certainly helps to know that

$$\lim_{Q^2 \rightarrow 0} \bar{T}_1(0, Q^2)/Q^2 = 4\pi\beta_{M1}, \quad (6.35)$$

but otherwise, the  $Q^2$  behavior of this amplitude leaves room to imagination. For example, Pachucki [246] and later Martynenko [247] use:

$$\bar{T}_1(0, Q^2) = 4\pi\beta_{M1} Q^2 / (1 + Q^2/\Lambda^2)^4, \quad (6.36)$$

with  $\Lambda^2 = 0.71 \text{ GeV}^2$ , whereas Carlson and Vanderhaeghen [248] and Birse and McGovern [249] use more sophisticated forms, inspired by chiral loops. The leading-order [ $O(p^3)$ ]  $\chi$ PT calculation contains a genuine prediction for the subtraction function, as well as for the whole polarizability effect, see Sect. 6.5 for more details.

<sup>20</sup>For the expansion we use,  $1/(v_l + v) \simeq \frac{Q}{2(m+M)} (1 - Q^2/8mM)$ ,  $[2(v_l + 1)(v + 1)]^{-1} \simeq Q^2/8mM$ .

Table 6.1: Summary of available dispersive calculations for the TPE correction to the  $2S$ -level in  $\mu\text{H}$ . Energy shifts are given in  $\mu\text{eV}$ ,  $\beta_{M1}$  is given in  $10^{-4} \text{ fm}^3$ .

	Pachucki [246]	Martynenko [247]	Carlson & Vanderhaeghen [248] <sup>b</sup>	Birse & McGovern [249]	Gorchtein et al. [253] <sup>a</sup>
$\beta_{M1}$	1.56(57)[256]	1.9(5) [257]	3.4(1.2)[146, 147]	3.1(5)[65]	
$\Delta E^{\text{subt}}(2S)$	1.9	2.3	5.3(1.9)	4.2(1.0)	−2.3(4.6)
$\Delta E^{\text{inel}}(2S)$	−13.9 [258, 259]	−16.1	−12.7(5)[260, 261]	−12.7(5) <sup>c</sup>	−13.0(6) [260–262]
$\Delta E^{\text{pol}}(2S)$	−12(2)	−13.8(2.9)	−7.4(2.0)	−8.5(1.1)	−15.3(4.6)
$\Delta E^{\text{el}}(2S)$	−23.2(1.0)[263]		$\begin{cases} -27.8[264] \\ -29.5(1.3)[265] \\ -30.8[266, 267] \end{cases}$	−24.7(1.6) <sup>d</sup>	−24.5(1.2) [264–266]
$\Delta E(2S)$	−35.2(2.2)		−36.9(2.4)	−33(2)	−39.8(4.8)

<sup>a</sup>Adjusted values; the original values of Ref. [253],  $\Delta E^{\text{subt}}(2S) = 3.3$  and  $\Delta E^{\text{el}}(2S) = -30.1$ , are based on a different decomposition into the elastic and polarizability contributions.

<sup>b</sup>In this work a separation of the amplitude into ‘pole’ and ‘non-pole’, rather than ‘Born’ and ‘non-Born’, was chosen. It is pointed out in Ref. [249] that the ‘pole’ decomposition applied in [248] is inconsistent with the standard definition of the magnetic polarizability used ibidem.

<sup>c</sup>Value taken from Ref. [248].

<sup>d</sup>Result taken from Ref. [248] (FF [265]) with reinstated ‘non-pole’ Born piece.

An early study of the electric polarizability effect on the  $S$ -level shift in electronic and muonic atoms can be found in Ref. [250]. That work exploited an unsubtracted DR for the longitudinal amplitude  $T_L(\nu, Q^2) = (1 + \nu^2/Q^2) T_2(\nu, Q^2) - T_1(\nu, Q^2)$ , as introduced in Ref. [251]. As we have discussed in the previous section, such a DR is not valid for the proton.

A first standard dispersive calculation of the TPE effect was done by Pachucki [246], see also [227, 252]. The most recent updates can be found in Refs. [248, 249]. Presently, the recommended value is that of Birse and McGovern [249]. A somewhat different dispersive evaluation has recently been done by Gorchtein et al. [253]. There, the high-energy behavior of the subtraction function is related to the fixed  $J = 0$  Regge pole [203] through a finite-energy sum rule (see Eq. (29) in Ref. [253]).

Table 6.1 summarizes the dispersive evaluations of the TPE effects in the  $\mu\text{H}$  Lamb shift, while the  $\chi\text{PT}$  predictions can be found in Table 6.3. The corresponding ‘polarizability’ and ‘elastic’ TPE results are represented in the summary plots, see Fig. 7.9 and Fig. 7.10. Table 6.1 also shows the value of the magnetic polarizability used in the evaluations, since this is the main source of discrepancy among them.

Other frameworks, different from DR and  $\chi\text{PT}$ , for calculating the TPE effects in the Lamb shift can be found in [254] and [255]. The values obtained in these works are generally in agreement with the dispersive results. For example, Mohr et al. [255] quote:

$$\Delta E^{\text{inel}}(2S) = -17 \mu\text{eV}, \quad \Delta E^{\text{el}}(2S) = -20 \mu\text{eV}. \quad (6.37)$$

#### 6.4.2. Hyperfine Splitting

The leading-order HFS is given by the Fermi energy of the  $nS$ -level, cf. Eq. (6.2). The full HFS is divided into the following contributions:<sup>21</sup>

$$E_{\text{HFS}}(nS) = [1 + \Delta_{\text{QED}} + \Delta_{\text{weak}} + \Delta_{\text{structure}}] E_F(nS). \quad (6.38)$$

We are interested in the proton-structure correction, which is split into three terms: Zemach radius, recoil, and polarizability contribution,

$$\Delta_{\text{structure}} = \Delta_Z + \Delta_{\text{recoil}} + \Delta_{\text{pol}}. \quad (6.39)$$

<sup>21</sup>A review of polarizability corrections to the hydrogen HFS can be found in Ref. [268, Sect. 3]. A detailed formalism of the structure-dependent corrections to the  $2S$  HFS in both H and  $\mu\text{H}$  is given in Ref. [269], with comments on various conventions.

All of these can be deduced from Eq. (6.31), and are thus given in terms of the spin-dependent VVCS amplitudes  $S_1$  and  $S_2$ , which satisfy the DRs of Eqs. (5.12c)<sup>22</sup> and (5.15). This means the entire TPE contribution is given by the spin structure functions  $g_1$  and  $g_2$ . To separate out the polarizability contribution, one can write the DRs for the non-Born (polarizability) part of the amplitudes only:

$$\bar{S}_1(\nu, Q^2) = \frac{2\pi Z^2 \alpha}{M} F_2^2(Q^2) + \frac{16\pi Z^2 \alpha M}{Q^2} \int_0^{x_0} dx \frac{g_1(x, Q^2)}{1 - x^2(\nu/\nu_{\text{el}})^2}, \quad (6.40a)$$

$$\nu \bar{S}_2(\nu, Q^2) = \frac{64\pi Z^2 \alpha M^4 \nu^2}{Q^6} \int_0^{x_0} dx x^2 \frac{g_2(x, Q^2)}{1 - x^2(\nu/\nu_{\text{el}})^2}. \quad (6.40b)$$

One should not be perplexed by the Pauli FF term,  $F_2^2$ , appearing in  $\bar{S}_1$ . Its purpose is to cancel the elastic contribution of the GDH integral  $I_1(Q^2)$ , such that  $\bar{S}_1$  is indeed proportional to polarizabilities alone.

Let us now specify the decomposition of the structure-dependent correction into the three terms of Eq. (6.39). The first one is the Zemach contribution [273]:

$$\Delta_Z = \frac{8Z\alpha m_r}{\pi} \int_0^\infty \frac{dQ}{Q^2} \left[ \frac{G_E(Q^2)G_M(Q^2)}{1 + \kappa} - 1 \right] \equiv -2Z\alpha m_r R_Z. \quad (6.41)$$

The second one is the remaining elastic TPE contribution, which is a recoil-type of correction to the Zemach term:

$$\Delta_{\text{recoil}} = \frac{Z\alpha}{\pi(1 + \kappa)} \int_0^\infty \frac{dQ}{Q} \left( \frac{G_M(Q^2)}{Q^2} \frac{16mM}{v_l + v} \left\{ \left[ 1 + \frac{1}{2(v_l + 1)(v + 1)} \right] F_1(Q^2) - \frac{3\tau}{2} F_2(Q^2) \right\} - \frac{8m_r G_M(Q^2)G_E(Q^2)}{Q} - \frac{m F_2^2(Q^2)}{M} \frac{5 + 4v_l}{(1 + v_l)^2} \right). \quad (6.42)$$

Finally, the polarizability contribution is written as:

$$\Delta_{\text{pol}} = \frac{Z\alpha m}{2\pi(1 + \kappa)M} [\delta_1 + \delta_2] = \Delta_1 + \Delta_2, \quad (6.43a)$$

with the separate contributions due to  $g_1$  and  $g_2$  given by:

$$\delta_1 = 2 \int_0^\infty \frac{dQ}{Q} \left( \frac{5 + 4v_l}{(v_l + 1)^2} [4I_1(Q^2) + F_2^2(Q^2)] + \frac{8M^2}{Q^2} \int_0^1 dx g_1(x, Q^2) \right. \\ \left. \times \left\{ \frac{4}{v_l + \sqrt{1 + x^2\tau^{-1}}} \left[ 1 + \frac{1}{2(v_l + 1)(1 + \sqrt{1 + x^2\tau^{-1}})} \right] - \frac{5 + 4v_l}{(v_l + 1)^2} \right\} \right), \quad (6.43b)$$

$$\delta_2 = 96M^2 \int_0^\infty \frac{dQ}{Q^3} \int_0^1 dx g_2(x, Q^2) \left\{ \frac{1}{v_l + \sqrt{1 + x^2\tau^{-1}}} - \frac{1}{v_l + 1} \right\}. \quad (6.43c)$$

As emphasized before, our decomposition into  $\Delta_{\text{recoil}}$  and  $\Delta_{\text{pol}}$  corresponds with the decomposition into the Born and non-Born part. In this way, the decomposition is consistent with Pachucki [227], Carlson et al. [269], Bodwin and Yennie [274] and different from Martynenko [229], Faustov et al. [230]. In the latter works, the  $F_2^2$  term was shared differently between the elastic and polarizability contributions. The conversion between the two decompositions can be found in Ref. [269].

Let us now consider the numerical results. Early works mainly studied the proton structure corrections to the ground-state HFS in H [243, 244, 278, 279]. More recent evaluations of the polarizability contribution to the H HFS can be found in Refs. [271, 272, 280–282], radiative corrections are calculated in Ref. [277]. The most recent calculations of the polarizability contribution to the HFS in H are:

$$\text{Carlson et al. [275]} : \quad \Delta_{\text{pol}}^{\text{H}} = 1.88 \pm 0.64 \text{ ppm}, \quad (6.44a)$$

$$\text{Faustov et al. [276]} : \quad \Delta_{\text{pol}}^{\text{H}} = 2.2 \pm 0.8 \text{ ppm}. \quad (6.44b)$$

<sup>22</sup>The validity of the unsubtracted DRs is based on Regge theory [270], see also [271, 272] for a discussion of the no-subtraction assumption.

Table 6.2: Summary of available dispersive calculations for the TPE correction to the  $2S$  HFS of  $\mu\text{H}$ .

Reference	$R_Z$ [fm]	$\Delta_Z$ [ppm]	$\Delta_{\text{recoil}}$ [ppm]	$\Delta_{\text{pol}}$ [ppm]	$\Delta_1$ [ppm]	$\Delta_2$ [ppm]	$\Delta_{\text{structure}}$ [ppm]	$E_{2S \text{ HFS}}$ [meV]
Carlson et al. [275] <sup>a</sup>	1.080	-7703	931	351(114)	370(112)	-19(19)	-6421(140)	22.8146(49) [269]
Faustov et al. [276]				470(104)	518	-48		
Martynenko et al. [230]	1.022	-7180		460(80)	514	-58		22.8138(78)
Experiment [25]	1.082(37) <sup>b</sup>							22.8089(51)

<sup>a</sup>QED and structure-independent corrections are taken from Martynenko [229]. The Zemach term includes radiative corrections:  $\Delta_Z = -2\alpha m_r R_Z(1 + \delta_Z^{\text{rad}})$ , with  $\delta_Z^{\text{rad}}$  of Refs. [274, 277].

<sup>b</sup>Extraction based on the recoil and polarizability corrections from Ref. [275] (1st row of the Table).

The available dispersive calculations for the  $2S$  TPE correction to the HFS in  $\mu\text{H}$  are listed in Table 6.2 and, in a more illustrative form, Fig. 7.11. Some of the results are given in terms of the  $2S$  Fermi energy in  $\mu\text{H}$ :  $E_F(2S) = 22.8054 \text{ meV}$ .

Most of the calculations show a relatively small effect from  $g_2$ , see  $\Delta_2$  in Table 6.2. It seems to be well within the uncertainty of the  $g_1$  contribution ( $\Delta_1$ ). However, it is important to note here that the spin structure function  $g_2$  of the proton has not been measured experimentally in the low- $Q$  region, relevant to the atomic calculations. The above evaluations are either modeling  $g_2$ , or make use of the Wandzura-Wilczek relation [198] to express it in terms of  $g_1$ :<sup>23</sup>

$$g_2^{\text{WW}}(x, Q^2) = -g_1(x, Q^2) + \int_x^1 \frac{dx'}{x'} g_1(x', Q^2). \quad (6.45)$$

The latter relation is for asymptotically large  $Q^2$ . It is certainly violated for low  $Q^2$ —it's only a question of how badly. The ongoing JLab measurement of proton  $g_2$  [283] is extremely important for answering that question.

Information on the structure function  $g_1$  is available for momentum-transfers larger than  $Q_{\text{min.}}^2 \sim 0.05 \text{ GeV}^2$  [284]. Below this threshold, the  $Q^2$ -integrand of Eq. (6.43b) is interpolated by exploiting the sum rules. In the case of H, where the electron mass can safely be neglected, the slope of the integrand is fixed by the GDH sum rule (5.23). In  $\mu\text{H}$  the dependence on the muon mass is not negligible, and the GTT sum rule (5.24) proves to be useful, cf. Carlson et al. [275].

## 6.5. Chiral EFT Evaluations

Below  $O(p^4)$ ,  $\chi\text{PT}$  provides a genuine prediction for the TPE effects. At  $O(p^4)$  there is a number of low-energy constants (LECs), entering through the effective lepton-lepton-nucleon-nucleon ( $\ell\ell NN$ ) coupling, whose values are presently unknown. Therefore, the predictive power is lost at this order. Here we only consider the "predictive orders", i.e.,  $O(p^3)$  and  $O(p^{7/2})$ . These will be called the leading (LO) and next-to-leading (NLO) order, respectively.<sup>24</sup>

### 6.5.1. Lamb Shift

The leading-order [ $O(p^3)$ ] calculations of the  $\mu\text{H}$  Lamb shift have been done in both heavy-baryon ( $\text{HB}\chi\text{PT}$ ) and baryon ( $\text{B}\chi\text{PT}$ ) frameworks [55, 285]. The diagrams arising in these calculations are shown in Fig. 6.6. The LO  $\text{HB}\chi\text{PT}$  result for the polarizability contribution to the  $2S$ -level shift is well described by the following simple formula [55]:

$$\Delta E_{\text{HB}\chi\text{PT}}^{\text{pol}}(2S) = \frac{\alpha^5 m_r^3 g_A^2}{4(4\pi f_\pi)^2} \frac{m_\mu}{m_\pi} \left(1 - 10G + 6 \ln 2\right) \simeq -16.1 \text{ } \mu\text{eV}, \quad (6.46)$$

where  $G \simeq 0.9160$  is the Catalan constant; other parameters are defined in Sect. 1.1. The LO  $\text{B}\chi\text{PT}$  result is somewhat smaller in magnitude, see Table 6.3. This is mainly because of the smaller value of the proton

<sup>23</sup>This relation automatically satisfies the BC sum rule, i.e.,  $\int_0^1 dx g_2^{\text{WW}}(x, Q^2) = 0$ , as easily seen via the Fubini rule.

<sup>24</sup>Technically, the leading order is  $O(p^2)$ , but it is included in the Coulomb interaction.

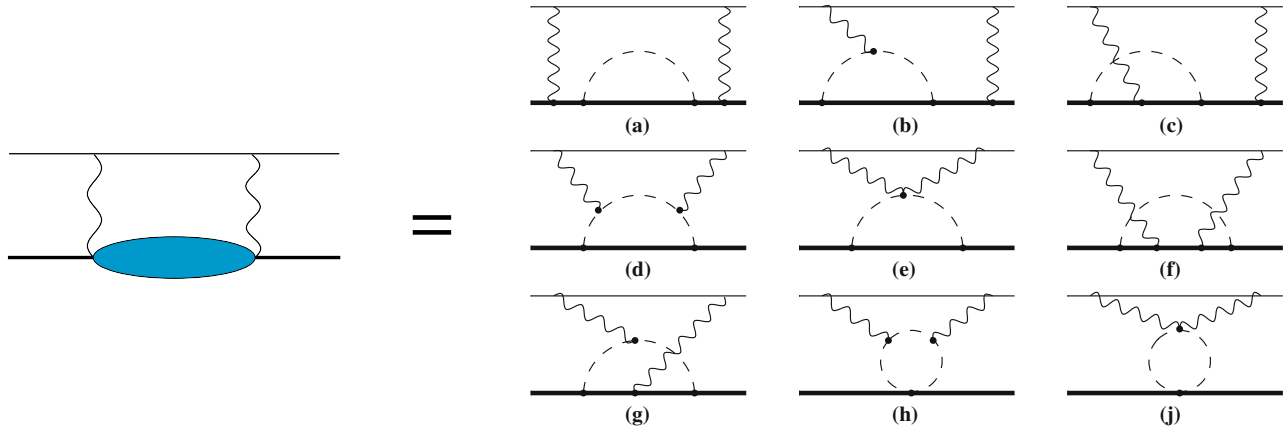


Figure 6.6: The TPE diagrams of elastic lepton-nucleon scattering to  $O(p^3)$  in  $\chi$ PT. Diagrams obtained from these by crossing and time-reversal symmetry are not drawn.

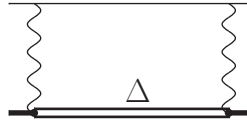


Figure 6.7: TPE diagram with  $\Delta(1232)$ , represented by the double line.

electric polarizability  $\alpha_{E1}$  arising in  $B\chi$ PT at leading order, cf. Sect. 2.4. The  $\pi\Delta$  loops at  $O(p^{7/2})$  are expected to correct this situation.

At next-to-leading order [ $O(p^{7/2})$ ], the diagrams with the  $\Delta(1232)$ -isobar arise, of which the one in Fig. 6.7 dominates the magnetic polarizability of the proton. In the Lamb shift, however, the magnetic polarizability is suppressed, and this particular diagram is suppressed too [55].

The calculations including the  $\Delta$  have thus far been done in  $HB\chi$ PT only [56]. The resulting NLO polarizability contribution is larger in magnitude than the LO, see Table 6.3 and Fig. 7.9. This is simply because in  $HB\chi$ PT the  $\Delta$  gives too large of a correction to the polarizabilities, cf. Eq. (2.8). On the other hand, the  $HB\chi$ PT underpredicts the elastic TPE contribution, see Table 6.3 and Fig. 7.10, because the Friar radius comes out to be smaller than the empirical value. The total value for the TPE effect in  $HB\chi$ PT happens to be in agreement with the empirical expectations.

Table 6.3: Summary of available  $\chi$ PT calculations for the TPE effect in the  $2S$ -level shift of  $\mu$ H (in  $\mu$ eV).

	Nevado & Pineda LO $HB\chi$ PT [285]	Alarcón et al. LO $B\chi$ PT [55]	Peset & Pineda NLO $HB\chi$ PT [286]
$\Delta E^{\text{pol}}(2S)$	-18.5(9.3)	-8.2( $^{+1.2}_{-2.5}$ )	-26.2(10.0)
$\Delta E^{\text{el}}(2S)$	-10.1(5.1)		-8.3(4.3)

### 6.5.2. Hyperfine Splitting

The LO  $B\chi$ PT calculation of the HFS should in addition to the diagrams in Fig. 6.6 include the neutral-pion exchange, Fig. 6.8. The latter effect, however, turned out to be consistent with 0, at least for the  $\mu$ H  $2S$  HFS [287]:

$$E_{\text{HFS}}^{(\pi^0)}(2S) = 0.02 \pm 0.04 \mu\text{eV}, \quad (6.47)$$

where the uncertainty comes from the experimental error of the  $\pi^0 \rightarrow e^+e^-$  decay width. In retrospect this is not so surprising, since the pion-exchange vanishes in the forward kinematics, and as such becomes suppressed by an additional  $\alpha$ .

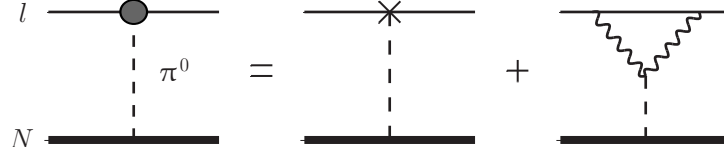


Figure 6.8: Pion-exchange in hydrogen.

A substantially larger pion-exchange effect has recently been found in Refs. [288, 289]. The calculation of Zhou and Pang [288] suffers from a technical mistake, as pointed out in [289]. On the other hand, Huong et al. [289] neglect the  $Q^2$ -dependence of the pion coupling to leptons which is not a good approximation for the reason explained below.

The non-relativistic limit of the pion-exchange potential reads (for the  $S$ -waves):

$$V_{\pi^0}^{l=0}(Q) = -\frac{F(F+1) - 3/2}{3mM} \frac{Q^2}{Q^2 + m_\pi^2} g_{\pi NN} F_{\pi\ell\ell}(Q^2), \quad (6.48)$$

where  $F = 0$  or  $1$  is the eigenvalue of the total angular momentum,  $m_\pi$  is the neutral-pion mass,  $g_{\pi NN}$  is the pion-nucleon coupling constant, and  $F_{\pi\ell\ell}$  is the FF describing the pion coupling to leptons. The latter satisfies the well-known (once-subtracted) DR [290]:

$$F_{\pi\ell\ell}(Q^2) = F_{\pi\ell\ell}(0) - \frac{Q^2}{\pi} \int_0^\infty \frac{ds}{s} \frac{\text{Im } F_{\pi\ell\ell}(s)}{s + Q^2}, \quad \text{with } \text{Im } F_{\pi\ell\ell}(s) = -\frac{\alpha^2 m \text{ arccosh}(\sqrt{s}/2m)}{2\pi f_\pi \sqrt{1 - 4m^2/s}}, \quad (6.49)$$

where  $f_\pi$  is the pion-decay constant,  $m$  is the lepton mass. This decomposition into the subtraction constant and the effect of the  $2\gamma$  loop is illustrated in Fig. 6.8. The subtraction constant can be extracted from the experimental value of the  $\pi^0 \rightarrow e^+e^-$  decay width, which in terms of the FF is given by:

$$\Gamma(\pi^0 \rightarrow e^+e^-) = \frac{m_\pi}{8\pi} \sqrt{1 - \frac{4m_e^2}{m_\pi^2}} |F_{\pi ee}(-m_\pi^2)|^2. \quad (6.50)$$

Now, the point is that the FF in Eq. (6.49) does not admit a good Taylor expansion around  $Q^2 = 0$ , because of the branch cut starting at 0. Hence, in contrast to the  $\pi NN$  FF, we cannot neglect its  $Q^2$ -dependence. A straightforward calculation yields the following result for the HFS effect:

$$E_{\text{HFS}}^{(\pi^0)}(nS) = -E_F(nS) \frac{g_{\pi NN} m_r}{2\pi(1 + \kappa)m_\pi} \left[ F(0) + \frac{\alpha^2 m}{2\pi^2 f_\pi} I\left(\frac{m_\pi}{2m}\right) \right], \quad (6.51)$$

where we introduce the following integral,

$$I(\gamma) \equiv 2 \int_0^\infty \frac{d\xi}{1 + (\xi/\gamma)} \frac{\arccos \xi}{\sqrt{1 - \xi^2}}. \quad (6.52)$$

For H,  $\gamma \gg 1$ , and one can make use of the expansion:  $I(\gamma) = 7\pi^2/12 + \ln^2(2\gamma) + O(1/\kappa)$ . For the more general situation,  $\gamma = \sin \theta \geq 0$ , we have:

$$I(\sin \theta) = \tan \theta [\text{Cl}_2(2\theta) - \pi \ln \tan(\theta/2)], \quad (6.53)$$

where  $\text{Cl}_2(\theta) = -\int_0^\theta dt \ln(2 \sin t/2) = \frac{i}{2} [\text{Li}_2(e^{-i\theta}) - \text{Li}_2(e^{i\theta})]$  is the the Clausen integral;  $\text{Li}_2(x)$  is the Euler dilogarithm. The numerical values for the electron and muon, respectively, are:  $I(m_\pi/2m_e) \simeq 36.8316$ ,  $I(m_\pi/2m_\mu) \simeq 3.4634$ .

We find that in H and  $\mu$ H alike, there is a large cancellation between the two terms in Eq. (6.51), or equivalently between the two diagrams in Fig. 6.8. The resulting  $\mu$ H value is the one quoted above, in Eq. (6.47).

A preliminary calculation [287] shows that in total the LO B $\chi$ PT effects amount to the following polarization contribution to the  $2S$  HFS of  $\mu$ H:

$$O(p^3): \quad E_{\text{HFS}}^{\text{pol}}(2S) = 0.87 \pm 0.42 \mu\text{eV}. \quad (6.54)$$



This is about an order of magnitude smaller than the effect obtained in the empirical dispersive calculations, cf. Table 6.2. However, it can be expected that the  $\Delta$ -excitation mechanism of Fig. 6.7 can play an important role here. It remains to be seen whether this NLO effect will restore the agreement between the  $\chi$ PT and dispersive results.

## 7. Summary Plots and Conclusions

To summarize and conclude we have compiled the following summary plots surveying the recent results for nucleon polarizabilities and for their contribution to the  $2S$ -levels of muonic hydrogen.

### 7.1. Scalar Polarizabilities

Figures 7.1 and 7.2 present the situation for  $\alpha_{E1} + \beta_{M1}$  and  $\beta_{M1}$  of the proton and neutron, respectively. In the top of the left panels we have the results of the Baldin sum-rule evaluations considered in Table 5.1. The orange band indicates the weighted-average of these evaluations.

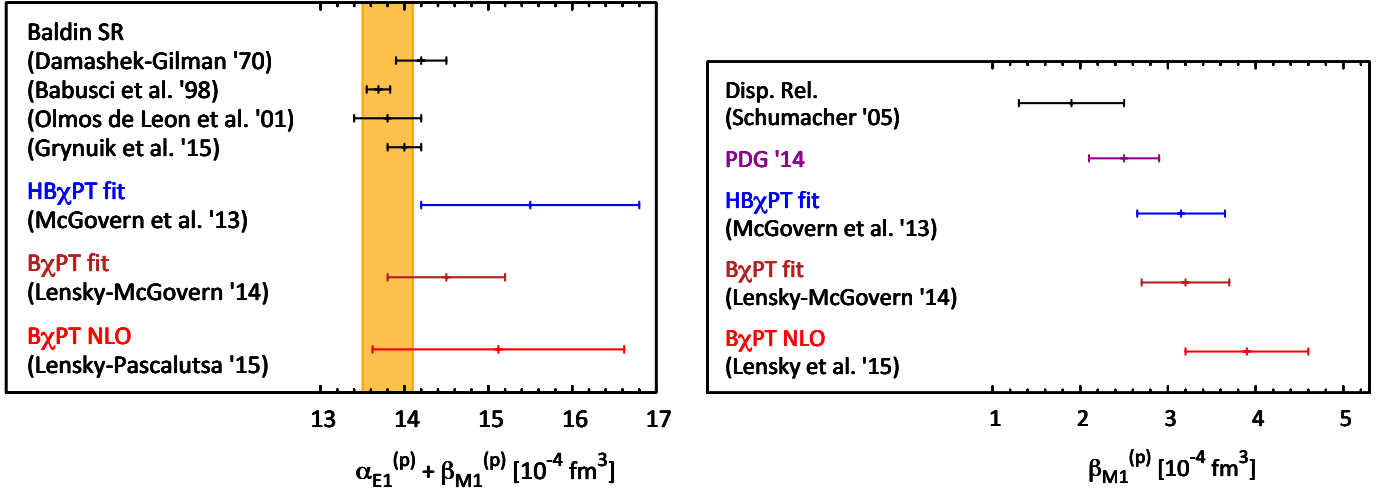


Figure 7.1: Left panel: sum of the electric and magnetic dipole polarizabilities of the proton. Right panel: the magnetic dipole polarizability of the proton. The orange band is the weighted average over the Baldin sum rule evaluations listed in Table 5.1. The DR prediction for  $\beta_{M1}^{(p)}$  can be found in the review of Schumacher [62]. “Lensky-Pascalutsa '15” refers to Ref. [34, 124], whereas “Lensky et al. '15” refers to Ref. [54]. All other references and declarations are given in the text.

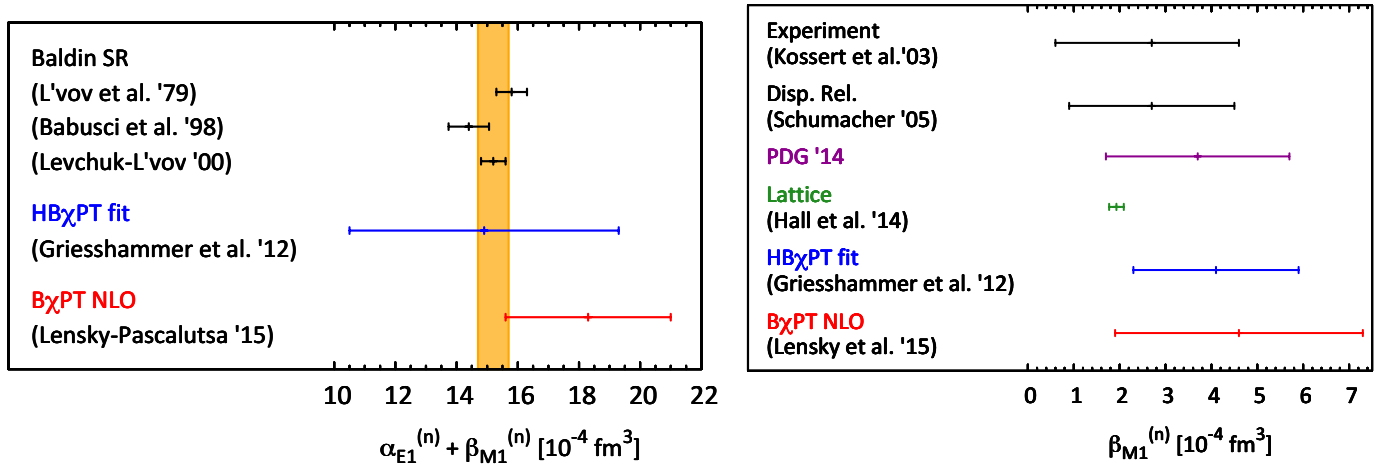


Figure 7.2: Left panel: sum of the electric and magnetic dipole polarizabilities of the neutron. Right panel: the magnetic dipole polarizability of the neutron. The orange band is the weighted average over the Baldin sum rule evaluations listed in Table 5.1. The experimental results for  $\beta_{M1}^{(n)}$  are from Refs. [291, 292] and [62]. Other references are given in the text.

It appears that there is a substantial tension in the value of the proton magnetic polarizability, cf. the right panel of Fig. 7.1. An emerging objective in this area is to reduce the uncertainty on  $\beta_{M1}^{(p)}$  by approximately 50%

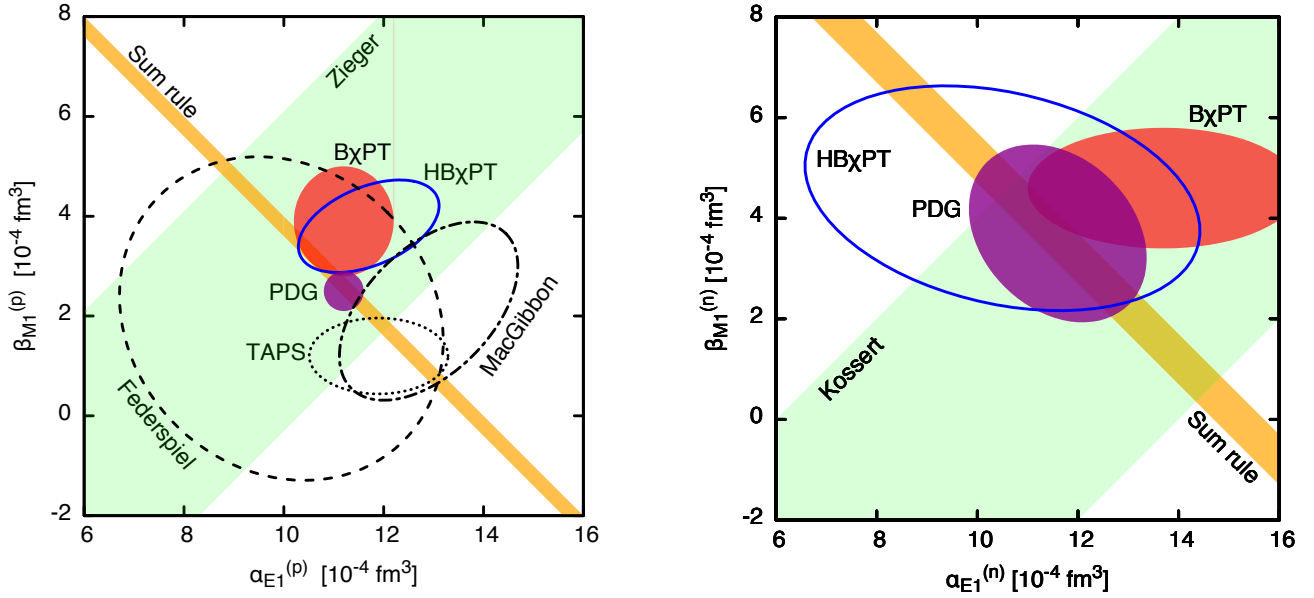


Figure 7.3: Plot of  $\alpha_{E1}$  versus  $\beta_{M1}$  for the proton (left panel) and neutron (right panel), respectively. The orange band is the average over the Baldin sum rule evaluations listed in Table 5.1. References and declarations are given in the text, cf. also Fig. 7.1 and 7.2.

through a measurement technique that is ideally independent of the Baldin sum rule. The utilization of photon beams with high intensity and high linear polarization will be a key part of these investigations. Exploratory measurements are currently underway at HI $\gamma$ S and Mainz.

In the area of the neutron scalar polarizabilities, the recent Lund publication [15] of elastic CS on the deuteron is an important milestone. For the first time, relatively high statistics and wide kinematic coverage elastic data are available, and the data are analyzable with state-of-the-art effective-field theory calculations. With the unfortunate discontinuation of the CS program at Lund, the focus will now likely shift to other labs and different nuclear targets. At Mainz an experiment to measure elastic CS on  $^4\text{He}$  is in preparation.

Another graphical representation of the experimental and theoretical results for the dipole polarizabilities,  $\alpha_{E1}$  and  $\beta_{M1}$ , is shown in Fig. 7.3. The orange band again represents the constraint by the Baldin sum rule. The light green bands show experimental constraints on the difference of dipole polarizabilities, i.e.,  $\alpha_{E1} - \beta_{M1}$ , cf. Kossert et al. [291, 292] and Zieger et al. [16]. For the proton, other experimental constraints are shown by black lines: Federspiel et al. [10], MacGibbon et al. [12] and TAPS [17]. The  $B\chi\text{PT}$  constraint are from Ref. [54]. The  $HB\chi\text{PT}$  constraint are from Ref. [51], in case of the proton, and [65], in case of the neutron. Obviously the knowledge of the neutron polarizabilities is less precise than for the proton. This is mainly due to the lack of free neutron targets.

Note that in these plots we have used the most recent PDG values [71]:

$$\alpha_{E1}^{(p)} = (11.2 \pm 0.4) \times 10^{-4} \text{ fm}^3, \quad \beta_{M1}^{(p)} = (2.5 \mp 0.4) \times 10^{-4} \text{ fm}^3, \quad (7.1a)$$

$$\alpha_{E1}^{(n)} = (11.6 \pm 1.5) \times 10^{-4} \text{ fm}^3, \quad \beta_{M1}^{(n)} = (3.7 \mp 2.0) \times 10^{-4} \text{ fm}^3. \quad (7.1b)$$

They are different from the 2012 and earlier editions by inclusion of the global data fit analysis [51].

What has emerged from the low- $Q^2$  studies, see Fig. 4.16, is interesting and provocative; there may well be a non-dipole-like structure in  $\alpha_{E1}(Q^2)$  at  $Q^2 \approx 0.33 \text{ GeV}^2$ . If correct, this would indicate that the proton has a pronounced structure in its induced polarization at large transverse distances, 0.5 to 1 fm, cf. Fig. 4.17. New data are required to confirm this. The Mainz A1 collaboration have taken VCS data at  $Q^2 \approx 0.1, 0.2$  and  $0.5 \text{ GeV}^2$ , and this data is currently under analysis. Formulating connections between VCS and VVCS polarizabilities at finite  $Q^2$  is a future task and could be of interest in this context.

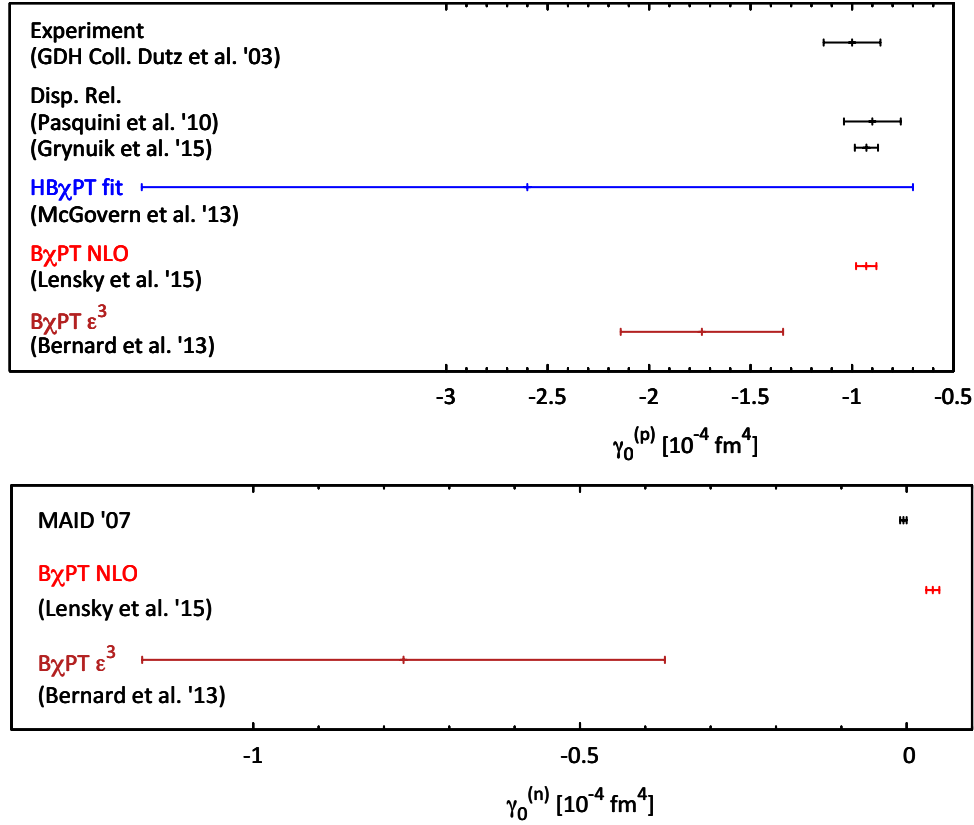


Figure 7.4: Forward spin polarizability,  $\gamma_0$ , of the proton (top panel) and neutron (bottom panel). Shown are the experimental value from the GDH-Collaboration [213], the DR result of Pasquini et al. [169], the HB $\chi$ PT fit of McGovern et al. [51], the B $\chi$ PT predictions of Lensky et al. [34, 124] and Bernard et al. [33]. All other references and declarations are given in the text or the Tables 4.2 and 5.2.

## 7.2. Spin Polarizabilities

The theoretical and experimental results for the proton spin polarizabilities have been presented in Table 4.2. Figure 7.4 summarizes the situation for the forward spin polarizability of the proton and neutron. The sum rule evaluations therein are from Table 5.2. Results for the backward spin polarizability of the proton are shown in Fig. 7.5.

A milestone in this area has been the recent Mainz publication of double polarized CS data for the  $\Sigma_{2x}$  asymmetry, and the global analysis of CS asymmetry data, leading to the first measurement of all four spin polarizabilities,  $\gamma_{E1E1}$ ,  $\gamma_{M1M1}$ ,  $\gamma_{E1M2}$ , and  $\gamma_{M1E2}$ , cf. Table 4.2 [38]. At Mainz new data have been taken on the linear polarization asymmetry  $\Sigma_3$ , and the double polarization asymmetry with longitudinally polarized target  $\Sigma_{2z}$ .

An attainable goal in this area is to reduce the uncertainties in spin polarizabilities, currently at  $\approx \pm 1 \times 10^{-4} \text{ fm}^4$ , by approximately 50%. Given that CS count rates for a 2 cm long frozen spin butanol target are very low compared to a 10 cm liquid hydrogen target, long running times on polarized targets may not be the best approach to drive down errors. Another strategy is to combine a global anal-

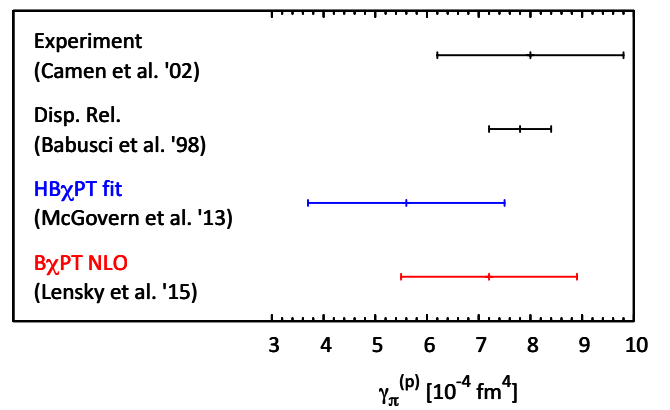


Figure 7.5: Backward spin polarizability,  $\gamma_\pi$ , of the proton. We show the experimental value from Camen [20], cf. Eq. (4.12), the fixed- $t$  DR result of Babusci et al. [96], the HB $\chi$ PT fit of McGovern et al. [51] and the B $\chi$ PT prediction of Lensky et al. [54].

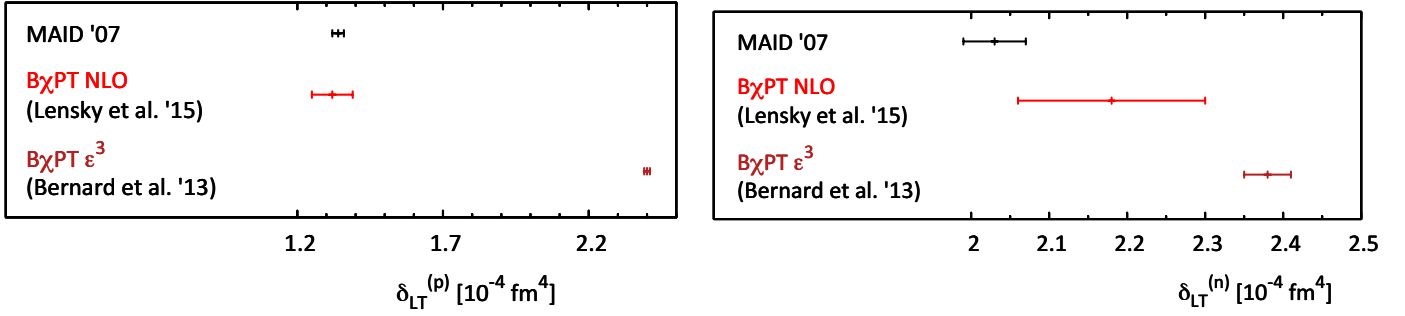


Figure 7.6: Longitudinal-transverse polarizability,  $\delta_{LT}$ , for the proton (left panel) and neutron (right panel), respectively. We show the  $B\chi PT$  predictions of Lensky et al. [34, 124] and Bernard et al. [33], and a result from MAID [209].

ysis of the asymmetry data,  $\Sigma_3$ ,  $\Sigma_{2x}$  and  $\Sigma_{2z}$ , with measurements of backward angle CS cross sections in the  $\Delta(1232)$  region. Because the  $\Sigma_{2z}$  asymmetry for backward angle CS approaches 1 (see Fig. 4.13), unpolarized CS preferentially selects one initial target polarization, and there is reasonable sensitivity to the spin polarizabilities in the unpolarized cross sections.

The longitudinal-transverse polarizability,  $\delta_{LT}$ , and the forward spin polarizability,  $\gamma_0$ , deserve a special attention. Their values at the real-photon point are shown in Fig. 7.6 and 7.4 for the proton and neutron, respectively. On the theory side, the baryon  $\chi PT$  yields genuine predictions for the spin polarizabilities, cf. Bernard et al. [33] and Lensky et al. [34, 124]. On the empirical side, we have for instance the results from the latest version of the MAID partial-wave analysis (MAID'07), which is based on the empirical knowledge of the single-pion photoproduction cross section  $\sigma_{LT}$ . Especially for  $\delta_{LT}^{(p)}$ , one  $B\chi PT$  result is in significant contradiction with MAID, while the other one is in agreement. The two  $B\chi PT$  calculations are done in different counting schemes for the  $\Delta$ -isobar contributions, cf. Sect. 2.4. As result, the  $\epsilon^3$  calculation includes in addition the graphs with several  $\Delta$ -propagators, and in particular the one where the photons couple minimally to the  $\Delta$  inside the chiral loop. The latter graph is allegedly making up all the difference [293]. This would mean the  $\pi\Delta$  channel is extremely important for this

quantity and that is why the MAID estimate would be inadequate. New JLab data [283] for  $\delta_{LT}^{(p)}$  down to virtualities of  $0.02 \text{ GeV}^2$  are currently at a final stage of analysis and will shed a further light on this “ $\delta_{LT}$  puzzle”. Complementary, as a check one could simply study the effect of this graph for the sum of the scalar polarizabilities,  $\alpha_{E1} + \beta_{M1}$ . There the empirical number is very well-known from the Baldin sum rule. This is yet another incarnation of the “ $\delta_{LT}$  puzzle” and at the moment this discrepancy is an open problem of  $B\chi PT$ . For  $\gamma_0$  the

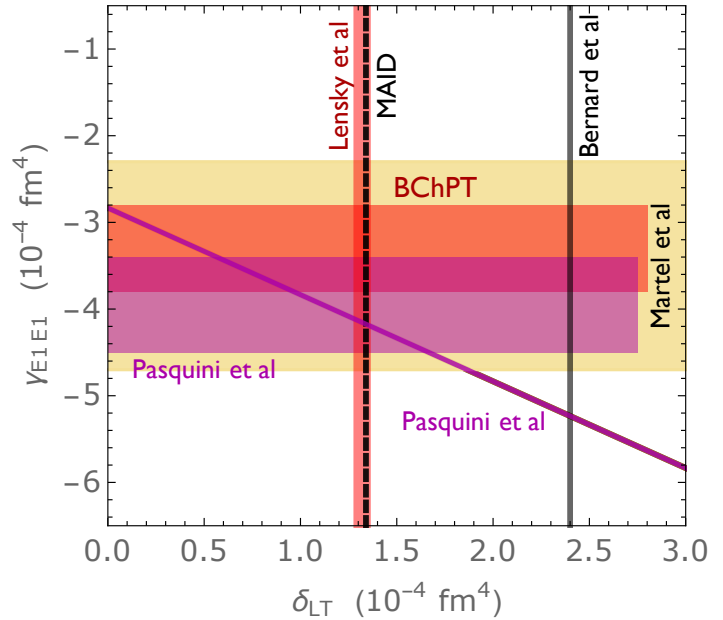


Figure 7.7: Spin polarizabilities,  $\gamma_{E1E1}$  versus  $\delta_{LT}$ , for the proton. Results for  $\gamma_{E1E1}$  (horizontal bands) are from: the experiment of Martel et al. [38] (beige), the  $B\chi PT$  calculation of Lensky et al. [54] (red), and the fixed- $t$  DR calculation of [96, 97] (purple). Results for  $\delta_{LT}$  (vertical bands) are from: MAID [209] (dashed line), Lensky et al. [34] (red), and Bernard et al. [33] (gray). The line across is based on the relation of (5.45b) using the values of GPs from the DR calculation of Pasquini et al. [149].

situation is less severe, the agreement with the GTT sum rule is much better, but still the discrepancy between different counting schemes remains.

Another view of this problem is presented in Fig. 7.7. The vertical lines clearly show the discrepancy in  $\delta_{LT}$ . The red bands are from the NNLO calculations of Lensky et al. [34, 54] using the  $\delta$ -expansion. They are consistent with the DR approach. It would be interesting to see the  $\epsilon$ -expansion result of Bernard et al. [33] for  $\gamma_{E1E1}$  too, because it seems it would contradict with the empirical results in either the GP's slope [cf. Eq. (5.45b)] or  $\gamma_{E1E1}$  itself.

### 7.3. Status of the Proton-Radius Puzzle

Currently, the value of the proton rms charge radius extracted from H spectroscopy disagrees with the  $\mu$ H value by nearly five standard deviations:

- H [223]:  $R_E = 0.8758(77)$  fm;<sup>25</sup>
- $\mu$ H [25, 225]:  $R_E = 0.84087(39)$  fm.

On the other hand, the elastic electron-proton ( $ep$ ) scattering, which is the classic way of accessing the charge radius, yields conflicting results on the charge and magnetic rms radii:

- Sick [240]:  $R_E = 0.886(8)$  fm,  $R_M = 0.868(24)$  fm;
- Lorenz et al. [295]:  $R_E = 0.840 [0.828 \dots 0.855]$  fm,  $R_M = 0.848 [0.843 \dots 0.854]$  fm;
- Bernauer et al. [294] (world data):

$$\begin{aligned}
 R_E &= 0.879(5)_{\text{stat}}(4)_{\text{syst}}(2)_{\text{model}}(4)_{\text{group}} \text{ fm}, \\
 R_E^{\text{TPE,a}} &= 0.876(5)_{\text{stat}}(4)_{\text{syst}}(2)_{\text{model}}(5)_{\text{group}} \text{ fm}, \\
 R_E^{\text{TPE,b}} &= 0.875(5)_{\text{stat}}(4)_{\text{syst}}(2)_{\text{model}}(5)_{\text{group}} \text{ fm}, \\
 R_M &= 0.777(13)_{\text{stat}}(9)_{\text{syst}}(5)_{\text{model}}(2)_{\text{group}} \text{ fm}, \\
 R_M^{\text{TPE,a}} &= 0.803(13)_{\text{stat}}(9)_{\text{syst}}(5)_{\text{model}}(3)_{\text{group}} \text{ fm}, \\
 R_M^{\text{TPE,b}} &= 0.799(13)_{\text{stat}}(9)_{\text{syst}}(5)_{\text{model}}(3)_{\text{group}} \text{ fm},
 \end{aligned}$$

where the superscript refers to the set of applied TPE corrections: TPE,a [296], TPE,b [297, 298].

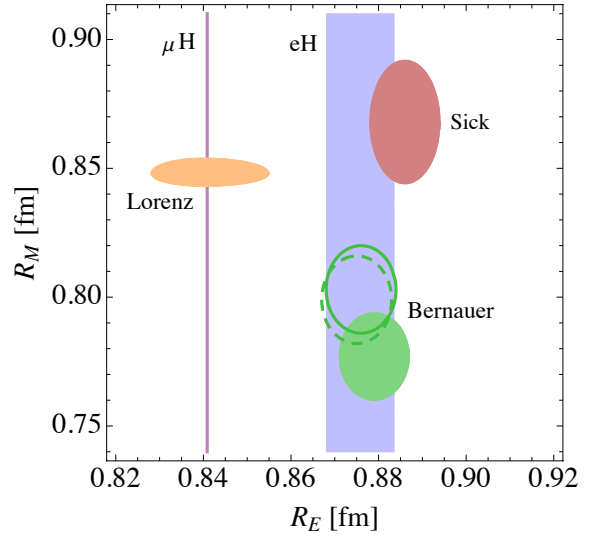


Figure 7.8: Determination of the proton's electric and magnetic radii. The shown values are given in the text. The green lines display the Bernauer fit with TPE corrections: TPE,a (solid), TPE,b (dashed). The different uncertainties given in Ref. [294] are added in quadrature.

The current situation is illustrated in Fig. 7.8. The CODATA 2010 recommended value, which combines the H and some of the  $ep$  scattering results, is [223]:

$$R_E(\text{H} + ep) = 0.8775(51) \text{ fm}, \quad (7.2)$$

which is in  $7\sigma$  disagreement with the  $\mu$ H result. This value does not include the interpretation of the  $ep$  scattering data based on dispersive approaches [295, 299, 300].

Further details can be found in dedicated reviews [69, 70]. A nice overview of the current and future experimental activities called to resolve the puzzle has recently been given by Antognini et al. [301].

### 7.4. Proton Structure in Muonic Hydrogen

Figures 7.9 and 7.10 display the various results of the dispersive and  $\chi$ PT calculations for the ‘polarizability’ and ‘elastic’ contributions of the TPE correction to the Lamb shift in  $\mu$ H. The corresponding values for the dispersive calculations are listed in Table 6.1, whereas the  $B\chi$ PT and  $HB\chi$ PT predictions are summarized in

<sup>25</sup>Based on H and D spectroscopy. From H alone (neglecting the isotope-shift measurements)  $R_E = 0.8796(56)$  fm.



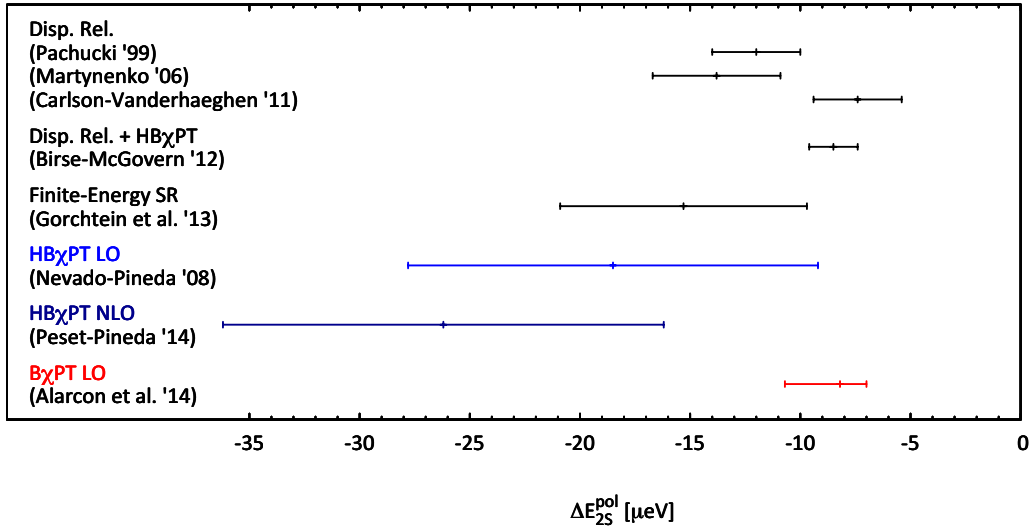


Figure 7.9: Proton polarizability effect in the  $2S$ -level shift of  $\mu\text{H}$ .

Table 6.3. In Fig. 7.10, we also show the contribution of the Friar radius ( $3^{\text{rd}}$  Zemach moment) from Jentschura [302] and Borie [228]. We also quote the result from the bound-state QED approach of Mohr et al. [255], cf. Eq. (6.37).

Figure 7.9 shows an overall agreement among the dispersive and  $B\chi\text{PT}$  calculations of the proton polarizability correction. The dispersive results involve the modeling of the ‘subtraction’ contribution which rely on the empirical value of proton  $\beta_{M1}$ , cf. Table 6.1, and Eqs. (6.35), (6.36). Given this model dependence, the agreement with the leading-order  $B\chi\text{PT}$  prediction is quite remarkable.

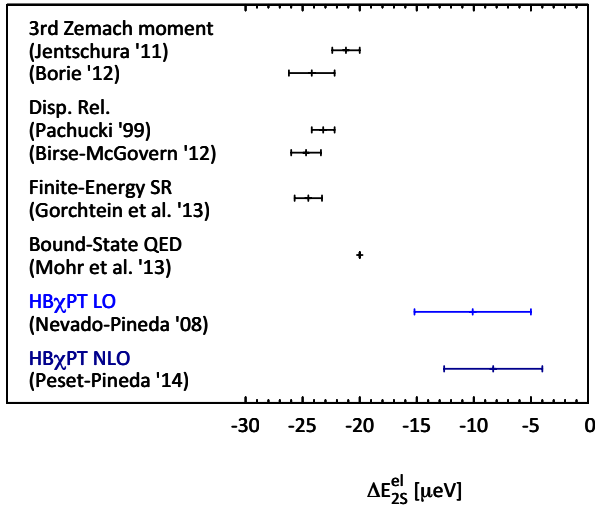


Figure 7.10: ‘Elastic’ TPE effect in the  $2S$ -level shift of  $\mu\text{H}$ .

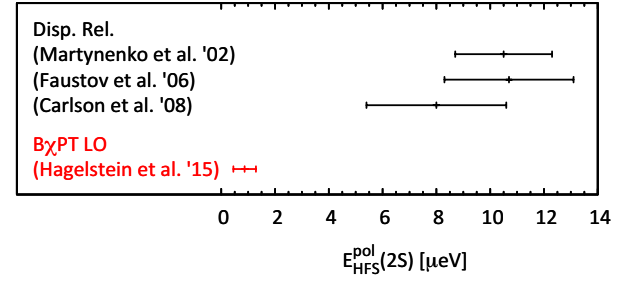


Figure 7.11: Proton polarizability effect in the  $2S$  HFS of  $\mu\text{H}$ .

Figure 7.10 shows the situation for the ‘elastic’ contribution. Since this contribution is completely determined by empirical FFs, the dispersive calculations agree very well. The bound-state QED approach of Ref. [255] gives a compatible result. The  $HB\chi\text{PT}$  results are not in good agreement with the empirical evaluations because the FFs are not well reproduced in these calculations.

Concerning the HFS, the polarizability corrections to the  $2S$  HFS are summarized in Fig. 7.11. The leading-order  $\chi\text{PT}$  prediction is quoted from Eq. (6.54). It is rather small compared with the dispersive calculations, which are taken from the  $\Delta_{\text{pol}}$  column of Table 6.2 and converted to  $\mu\text{eV}$  (multiplying the number in the column with  $E_F(2S) \times 10^{-6} \simeq 0.0228054 \mu\text{eV}$ ). Account of the  $\Delta(1232)$ -resonance excitation in  $\chi\text{PT}$  is expected

to improve the agreement. The different dispersive calculations are in agreement with each other and serve as input for the recent extraction of the proton Zemach radius [25].

Precise calculations of proton structure effects will be required to enable a direct measurement of the  $\mu\text{H}$  ground-state HFS (see, e.g., Sect. 6 of Ref. [303]). The corresponding transition is much narrower than the observed  $2S - 2P$  transitions, and hence is much harder to find. Quantitative theory guidance will be very important here. Once found, the HFS transition will greatly amplify the precision of our understanding of the proton structure in general, and of proton polarizabilities in particular.

Until then, in the words of the title of this paper, the *nucleon polarizabilities* are taken *from Compton scattering* and serve as input *to hydrogen atom*. We look forward to the times when the reverse is possible.

## Acknowledgements

We thank A. Alexandru, A. Antognini, C. Collicott, J. M. M. Hall, H. Fonvieille, P. P. Martel, and V. Sokhoyan for providing figures and useful insights into their work. We thank Jeremy Green, Misha Gorchtein, Vadim Lensky, Anatoly L’vov, Barbara Pasquini, Randolph Pohl and Marc Vanderhaeghen for reading the manuscript and their valuable remarks. R. M. thanks and acknowledges the Mainz A2 Compton collaboration for their critical support. V. P. gratefully acknowledges the inspiring discussions with Aldo Antognini, Carl Carlson, Misha Gorchtein, Savely Karshenboim, Marc Vanderhaeghen, and Thomas Walcher, which found their vague reflection in the pages of this manuscript.

This work was supported by the Deutsche Forschungsgemeinschaft (DFG) through the Collaborative Research Center SFB 1044 [The Low-Energy Frontier of the Standard Model], and the Graduate School DFG/GRK 1581 [Symmetry Breaking in Fundamental Interactions], and by the U.S. Department of Energy under grant DE-FG02-88ER40415.

## Appendix A. Born Contribution in RCS and VVCS amplitudes

For RCS, the Born term is given by the tree-level graphs with the photon coupling to the nucleon charge  $Ze$  and the anomalous magnetic moment  $\kappa$ . The invariant amplitudes of the overcomplete tensor decomposition of Eq. (3.28) are given by [? ]:

$$\mathcal{A}_i^{\text{Born}}(s, t) = \begin{cases} \mathcal{A}_i^s(\nu, t) + \mathcal{A}_i^s(-\nu', t), & \text{for } i = 1, 2, 8 \\ \mathcal{A}_i^s(\nu, t) - \mathcal{A}_i^s(-\nu', t), & \text{for } i = 3, \dots, 7, \end{cases} \quad (\text{A.1})$$

with  $\mathcal{A}_i^s$  being the contribution of the  $s$ -channel graph:

$$\begin{aligned} \mathcal{A}_1^s(\nu, t) &= -\frac{1}{2M} \left[ Z^2 + \frac{t}{4M\nu}(Z + \kappa)^2 + \frac{1}{2}\kappa^2 \left( \frac{\nu}{M} + \frac{t}{4M^2} \right) \right], \\ \mathcal{A}_2^s(\nu, t) &= \frac{\kappa}{2M^2\nu} \left[ Z + \frac{1}{2}\kappa \left( 1 - \frac{\nu}{2M} - \frac{t}{8M^2} \right) \right], \\ \mathcal{A}_3^s(\nu, t) &= \mathcal{A}_1^s(\nu, t), \\ \mathcal{A}_4^s(\nu, t) &= -\frac{1}{4M^2\nu} \left[ (Z + \kappa)^2 + \frac{\nu}{2M}\kappa^2 \right], \\ \mathcal{A}_5^s(\nu, t) &= \frac{(Z + \kappa)^2}{4M^2\nu}, \\ \mathcal{A}_6^s(\nu, t) &= -\frac{Z(Z + \kappa)}{4M^2\nu}, \\ \mathcal{A}_7^s(\nu, t) &= \frac{\kappa^2}{16M^4\nu}, \\ \mathcal{A}_8^s(\nu, t) &= -\mathcal{A}_4^s(\nu, t), \end{aligned} \quad (\text{A.2})$$

Adding it up, we obtain:

$$\mathcal{A}_1^{\text{Born}} = -\frac{Z^2}{M} - \frac{(Z + \kappa)^2 \xi_0^2}{M(\xi^2 - \xi_0^2)}, \quad \mathcal{A}_2^{\text{Born}} = -\frac{\kappa^2}{4M^3} + \frac{2M(2Z\kappa + \kappa)\xi_0 - \kappa^2 \xi_0^2}{4M^3(\xi^2 - \xi_0^2)}, \quad (\text{A.3a})$$

$$\mathcal{A}_3^{\text{Born}} = -2M\xi \left[ \frac{\kappa^2}{4M^3} + \frac{(Z + \kappa)^2 \xi_0}{2M^2(\xi^2 - \xi_0^2)} \right] = -2M\xi \mathcal{A}_8^{\text{Born}}, \quad (\text{A.3b})$$

$$\mathcal{A}_4^{\text{Born}} = -\frac{(Z + \kappa)^2 \xi}{2M^2(\xi^2 - \xi_0^2)} = -\mathcal{A}_5^{\text{Born}}, \quad \mathcal{A}_6^{(\text{B})} = -\frac{Z(Z + \kappa)\xi}{2M^2(\xi^2 - \xi_0^2)}, \quad \mathcal{A}_7^{\text{Born}} = \frac{\kappa^2 \xi}{8M^4(\xi^2 - \xi_0^2)}. \quad (\text{A.3c})$$

where  $\xi_0 = -q \cdot q' / 2M = t / 4M$  and  $\xi^2 - \xi_0^2 = \nu\nu'$  for real photons.

To obtain the Born contribution to the forward VVCS amplitudes, Eq. (5.5), one may use

$$T_1 = e^2 \mathcal{A}_1, \quad T_2 = \frac{e^2 Q^2}{\nu^2} (\mathcal{A}_1 + Q^2 \mathcal{A}_2), \quad (\text{A.4a})$$

$$S_1 = \frac{e^2 M}{\nu} [\mathcal{A}_3 + Q^2 (\mathcal{A}_5 + \mathcal{A}_6)], \quad S_2 = e^2 M^2 (\mathcal{A}_5 + \mathcal{A}_6), \quad (\text{A.4b})$$

with  $\xi = \nu$  and  $\xi_0 = -q^2 / 2M = Q^2 / 2M$ , and replace

$$Z \rightarrow F_1(Q^2), \quad \kappa \rightarrow F_2(Q^2). \quad (\text{A.5})$$

Often, the  $\pi^0$ -exchange contribution is considered to be a part of the Born contribution. The only non-vanishing amplitude for the  $\pi^0$ -exchange graph is:

$$\mathcal{A}_8^{(\pi^0)} = -\frac{(2Z - 1)g_A}{(2\pi f_\pi)^2} \frac{M}{m_{\pi^0}^2 - t}. \quad (\text{A.6})$$

## Appendix B. Derivation of a Dispersion Relation

Consider  $f(\nu)$ , an analytic function in the entire complex  $\nu$  plane except for the branch cut on the real axis, starting at  $\nu_0$  and extending to infinity, as shown in Fig. B.1 (a). In the case when there are left- and right-hand branch cuts, located symmetrically around  $\nu = 0$ , corresponding to Fig. B.1 (b), we can assume that

$$f(\nu) = f_s(\nu) \pm f_s(-\nu), \quad (\text{B.1})$$

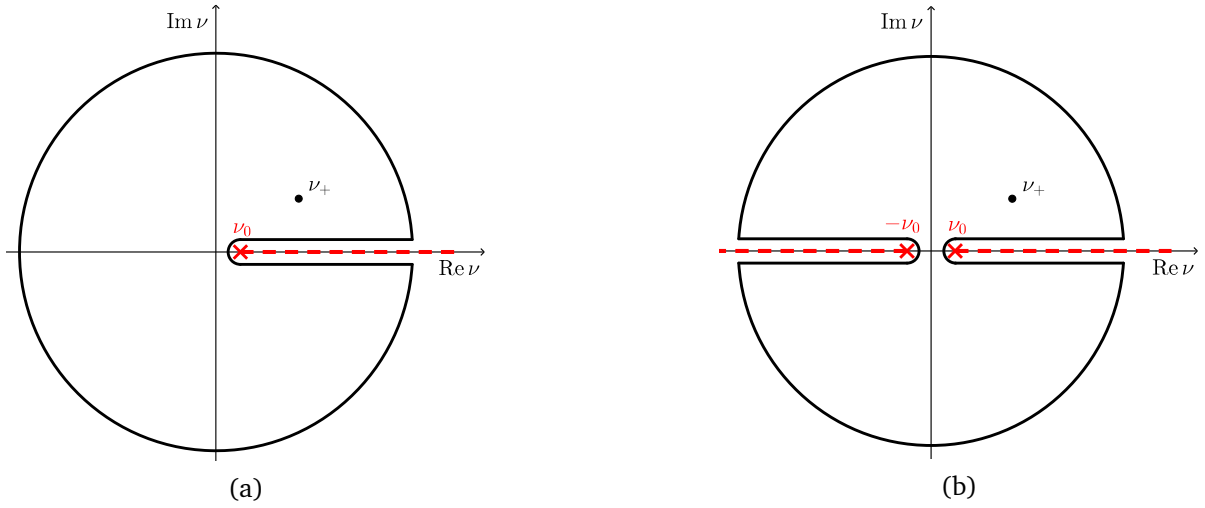


Figure B.1: Contours in the complex  $\nu$  plane for (a) a single cut along the positive real axis, and (b) branch cuts along the positive and negative real axes.

where  $f_s$  has only the right-hand cut. Hence, for our purpose it is sufficient to only consider the case of Fig. B.1 (a).

The starting point is Cauchy's formula for analytic functions:

$$f(\nu_+) = \frac{1}{2\pi i} \oint_C d\xi \frac{f(\xi)}{\xi - \nu_+}, \quad (\text{B.2})$$

where the contour  $C$  avoids the branch cut on the real axis, as seen in Fig. B.1, and  $\nu_+$  is in the region of analyticity (i.e., inside the contour). We choose  $\nu_+ = \nu + i\delta$ , where  $\nu$  and  $\delta$  are real. We will take the limit  $\delta \rightarrow 0$  in the end.

Next, we assume that  $f$  drops to zero for all large  $|\nu_+|$ , and it does so sufficiently fast, such that the integral over the big semicircle can be neglected.<sup>26</sup> We are then left with only the integrals around the cut:

$$f(\nu_+) = \lim_{\epsilon \rightarrow 0^+} \frac{1}{2\pi i} \int_{\nu_0}^{\infty} d\xi \left[ \frac{f(\xi + i\epsilon)}{\xi - \nu_+ + i\epsilon} - \frac{f(\xi - i\epsilon)}{\xi - \nu_+ - i\epsilon} \right], \quad (\text{B.3})$$

where  $\epsilon$  is the gap between the contour and the real axis. The integral over the small semicircle around  $\nu_0$  vanishes in the limit  $\epsilon \rightarrow 0$ , since  $f$  has no poles at  $\nu_0$ .

Employing the Schwarz reflection principle for analytic functions:

$$f^*(s) = f(s^*), \quad (\text{B.4})$$

and substituting  $\nu_+ = \nu + i\delta$ , we have

$$f(\nu_+) = \lim_{\epsilon \rightarrow 0^+} \frac{1}{2\pi i} \int_{\nu_0}^{\infty} d\xi \left[ \frac{f(\xi + i\epsilon)}{\xi - \nu - i(\delta - \epsilon)} - \frac{f^*(\xi + i\epsilon)}{\xi - \nu - i(\delta + \epsilon)} \right]. \quad (\text{B.5})$$

With  $\epsilon < \delta$ , the limit  $\epsilon \rightarrow 0$  can now be taken explicitly, since  $\delta$  takes over the signs of the imaginary parts, hence

$$\begin{aligned} f(\nu_+) &= \frac{1}{2\pi i} \int_{\nu_0}^{\infty} d\xi \frac{f(\xi) - f^*(\xi)}{\xi - \nu - i\delta} = \frac{1}{\pi} \int_{\nu_0}^{\infty} d\xi \frac{\text{Im} f(\xi)}{\xi - \nu - i\delta} \\ &= \frac{1}{\pi} \int_{\nu_0}^{\infty} d\xi \left[ \frac{\xi - \nu}{(\xi - \nu)^2 + \delta^2} + \frac{i\delta}{(\xi - \nu)^2 + \delta^2} \right] \text{Im} f(\xi). \end{aligned} \quad (\text{B.6})$$

Taking the limit to the real axis,  $\delta \rightarrow 0$ , we obtain the sought DR:

$$f(\nu) = \lim_{\delta \rightarrow 0^+} f(\nu_+) = \frac{1}{\pi} \int_{\nu_0}^{\infty} d\xi \frac{\text{Im} f(\xi)}{\xi - \nu - i0^+} = \frac{1}{\pi} \int_{\nu_0}^{\infty} d\xi \frac{\text{Im} f(\xi)}{\xi - \nu} + i \text{Im} f(\nu). \quad (\text{B.7})$$

<sup>26</sup>When this is not the case, we could replace  $f(\nu_+)$  with  $f(\nu_+)/\nu_+^n$ , provided we do not introduce another pole by doing that. So, for small  $\nu_+$ ,  $f$  should go as  $\nu_+^n$ . If  $f$  does not have any obvious zeros, one can make a subtraction. The subtracted function, by definition, has a zero at the subtraction point.

Coming back to the case when  $f$  is given as in Eq. (B.1), with  $f_s$  satisfying the above DR, we then obviously have

$$f(\nu) = \frac{1}{\pi} \int_{\nu_0}^{\infty} d\xi \left[ \frac{1}{\xi - \nu - i0^+} \pm \frac{1}{\xi + \nu - i0^+} \right] \text{Im} f_s(\xi) = \frac{2}{\pi} \int_{\nu_0}^{\infty} d\xi \left\{ \frac{\xi}{\nu} \right\} \frac{\text{Im} f(\xi)}{\xi^2 - \nu^2 - i0^+}, \quad (\text{B.8})$$

where in the last step we have used  $\text{Im} f(\xi) = \text{Im} f_s(\xi)$ , which is true if  $\nu_0 \geq 0$ . The situation with negative  $\nu_0$  is in principle treatable but is beyond the present scope.

## Appendix C. Collection/Index of Formulae

□ Kinematical invariants and relations for real Compton scattering (RCS)

$$\eta = \frac{M^4 - su}{M^2}, \quad \nu = \frac{s - M^2}{2M}, \quad \nu' = \frac{M^2 - u}{2M}. \quad (\text{3.14})$$

$$\omega = \frac{s - M^2}{2\sqrt{s}} = \frac{M\nu}{\sqrt{s}}, \quad \omega_B = \frac{s - u}{2\sqrt{4M^2 - t}}, \quad \epsilon_B = \frac{1}{2} \sqrt{4M^2 - t}. \quad (\text{C.1})$$

$$\xi = \frac{s - u}{4M} = \frac{\nu + \nu'}{2} = \frac{\omega_B \epsilon_B}{M}, \quad 4\xi^2 - \frac{t^2}{4M^2} = \eta - t = 4\nu\nu'. \quad (\text{C.2})$$

$$\begin{aligned} t &= 2M(\nu' - \nu) = -2\nu\nu'(1 - \cos \vartheta) = -2\omega^2(1 - \cos \theta) = -2\omega_B^2(1 - \cos \theta_B), \\ dt &= 2M d\nu' = (1/\pi) \nu'^2 d\Omega_L = (1/\pi) \omega^2 d\Omega_{cm}, \\ \cos^2(\vartheta/2) &= \eta/(4\nu\nu'), \quad \sin^2(\vartheta/2) = -t/(4\nu\nu'), \quad \sin \vartheta = \sqrt{-t\eta}/(2\nu\nu'), \\ \cos^2(\theta/2) &= \eta/(2\nu)^2, \quad \sin^2(\theta/2) = -t/(2\omega)^2, \quad \sin \theta = \sqrt{-t\eta s}/(2M\nu^2), \\ \cos^2(\theta_B/2) &= \eta/(2\xi)^2, \quad \sin^2(\theta_B/2) = -t/(2\omega_B)^2, \quad \sin \theta_B = \sqrt{-t\eta}/(2\xi\omega_B), \\ \tan(\vartheta/2) &= (-t/\eta)^{1/2} = M/\sqrt{s} \tan(\theta/2) = M/\epsilon_B \tan(\theta_B/2). \end{aligned} \quad (\text{C.3})$$

□ Relations for the forward doubly-virtual Compton scattering (VVCS)

$$\nu = \omega_B = \xi = \frac{1}{2} \eta^{1/2} = \frac{s - u}{4M} = \frac{s - M^2 + Q^2}{2M} = \frac{Q^2}{2Mx} = \frac{2M\tau}{x} \quad (\text{C.4})$$

$$\int_{\frac{Q^2}{2M}}^{\infty} \frac{d\nu}{\nu^n} f(\nu, Q^2) = \left( \frac{2M}{Q^2} \right)^{n-1} \int_0^1 dx x^{n-2} f(x, Q^2) \quad (\text{5.11})$$

□ Elastic structure functions

$$f_1^{\text{el}}(x, Q^2) = \frac{1}{2} G_M^2(Q^2) \delta(1 - x), \quad (\text{5.7a})$$

$$f_2^{\text{el}}(x, Q^2) = \frac{1}{1 + \tau} [G_E^2(Q^2) + \tau G_M^2(Q^2)] \delta(1 - x), \quad (\text{5.7b})$$

$$g_1^{\text{el}}(x, Q^2) = \frac{1}{2} F_1(Q^2) G_M(Q^2) \delta(1 - x), \quad (\text{5.7c})$$

$$g_2^{\text{el}}(x, Q^2) = -\frac{\tau}{2} F_2(Q^2) G_M(Q^2) \delta(1 - x). \quad (\text{5.7d})$$

□ Nucleon-pole and Born contributions to the forward VVCS amplitudes

$$T_1^{\text{pole}}(\nu, Q^2) = \frac{4\pi\alpha}{M} \frac{\nu_{\text{el}}^2 G_M^2(Q^2)}{\nu_{\text{el}}^2 - \nu^2 - i0^+} = T_1^{\text{Born}}(\nu, Q^2) + \frac{4\pi\alpha}{M} F_1^2(Q^2), \quad (\text{5.13a})$$

$$T_2^{\text{pole}}(\nu, Q^2) = \frac{8\pi\alpha \nu_{\text{el}}}{\nu_{\text{el}}^2 - \nu^2 - i0^+} \frac{G_E^2(Q^2) + \tau G_M^2(Q^2)}{1 + \tau} = T_2^{\text{Born}}(\nu, Q^2), \quad (\text{5.13b})$$

$$S_1^{\text{pole}}(\nu, Q^2) = \frac{4\pi\alpha \nu_{\text{el}}}{\nu_{\text{el}}^2 - \nu^2 - i0^+} F_1(Q^2) G_M(Q^2) = S_1^{\text{Born}}(\nu, Q^2) + \frac{2\pi\alpha}{M} F_2^2(Q^2), \quad (\text{5.13c})$$

$$[\nu S_2]^{\text{pole}}(\nu, Q^2) = -\frac{2\pi\alpha \nu_{\text{el}}^2}{\nu_{\text{el}}^2 - \nu^2 - i0^+} F_2(Q^2) G_M(Q^2) = \frac{\nu_{\text{el}}^2}{\nu} S_2^{\text{Born}}(\nu, Q^2). \quad (\text{5.13d})$$

□ Sum rules

$$\text{Baldin: } \alpha_{E1} + \beta_{M1} = \frac{1}{2\pi^2} \int_{\nu_0}^{\infty} \frac{d\nu}{\nu^2} \sigma(\nu) \quad (5.21)$$

$$4^{\text{th}}\text{-order: } \alpha_{E1\nu} + \beta_{M1\nu} + 1/12 (\alpha_{E2} + \beta_{M2}) = \frac{1}{2\pi^2} \int_{\nu_0}^{\infty} \frac{d\nu}{\nu^4} \sigma(\nu) \quad (5.22)$$

$$\text{Gerasimov–Drell–Hearn (GDH): } -\frac{\alpha}{M^2} \mathcal{K}^2 = \frac{1}{2\pi^2} \int_{\nu_0}^{\infty} \frac{d\nu}{\nu} [\sigma_{1/2}(\nu) - \sigma_{3/2}(\nu)] \quad (5.23)$$

$$\text{Gell-Mann–Goldberger–Thirring (GTT): } \gamma_0 = \frac{1}{4\pi^2} \int_{\nu_0}^{\infty} \frac{d\nu}{\nu^3} [\sigma_{1/2}(\nu) - \sigma_{3/2}(\nu)] \quad (5.24)$$

$$5^{\text{th}}\text{-order: } \bar{\gamma}_0 = \frac{1}{4\pi^2} \int_{\nu_0}^{\infty} \frac{d\nu}{\nu^5} [\sigma_{1/2}(\nu) - \sigma_{3/2}(\nu)] \quad (5.25)$$

$$\text{Burkhardt–Cottingham (BC): } 0 = \int_0^1 dx g_2(x, Q^2) = \frac{\tau}{2} [4 I_2(Q^2) - F_2(Q^2) G_M(Q^2)] \quad (5.14)$$

$$\text{spin-GP sum: } \frac{d}{dQ^2} [P^{(L1, L1)1}(q^2) + P^{(M1, M1)1}(q^2)]_{q^2=0} = \frac{\gamma_{E1M2}}{3\alpha M} - \frac{2}{3M^3} \frac{d}{dQ^2} [\frac{1}{4} F_2^2(Q^2) + I_1(Q^2)]_{Q^2=0} \quad (5.45a)$$

$$\text{spin-GP difference: } \frac{d}{dQ^2} [P^{(L1, L1)1}(q^2) - P^{(M1, M1)1}(q^2)]_{q^2=0} = \frac{\gamma_{E1E1} + \delta_{LT}}{3\alpha M} \quad (5.45b)$$

□ Dispersion relations for the Sachs FFs [for Dirac and Pauli FFs, see Eq. (6.8)]

$$\begin{pmatrix} G_E(Q^2) \\ G_M(Q^2) \end{pmatrix} = \begin{pmatrix} 1 \\ 1 + \kappa \end{pmatrix} - \frac{Q^2}{\pi} \int_{t_0}^{\infty} \frac{dt}{t(t+Q^2)} \text{Im} \begin{pmatrix} G_E(t) \\ G_M(t) \end{pmatrix}. \quad (C.5)$$

□ Moments of the (spherically-symmetric) charge distribution, for any  $N$ :

$$\langle r^N \rangle_E \equiv 4\pi \int_0^{\infty} dr r^{N+2} \rho_E(r) = \frac{\Gamma(N+2)}{\pi} \int_{t_0}^{\infty} dt \frac{\text{Im} G_E(t)}{t^{N/2+1}}, \quad (6.19)$$

with the normalization  $\langle r^0 \rangle_E = 1$ . Equivalently, for integer  $N$ :

$$\langle r^{2N} \rangle_E = (-1)^N \frac{(2N+1)!}{N!} G_E^{(N)}(0), \quad (C.6)$$

$$\begin{aligned} \langle r^{2N+1} \rangle_E &= (-1)^{N+1} (2N+2)! \frac{2}{\pi} \int_0^{\infty} \frac{dQ}{Q^{2N+2}} \left[ G_E(Q^2) - \sum_{k=0}^N \frac{Q^{2k}}{k!} G_E^{(k)}(0) \right], \\ &= (-1)^{N+1} (2N+2)! \frac{2}{\pi} \int_0^{\infty} \frac{dQ}{Q^{2N+2}} \left[ G_E(Q^2) - \sum_{k=0}^N \frac{(-Q^2)^k}{(2k+1)!} \langle r^{2k} \rangle_E \right]. \end{aligned} \quad (C.7)$$

The moments of the magnetization distribution,  $\langle r^N \rangle_M$ , are defined similarly by replacing  $G_E$  with  $G_M/(1+\kappa)$ .

□ Friar radius (or, the 3<sup>rd</sup> Zemach moment of the charge distribution)

$$R_F = \sqrt[3]{\langle r^3 \rangle_{E(2)}}, \quad \langle r^3 \rangle_{E(2)} \equiv \frac{48}{\pi} \int_0^{\infty} \frac{dQ}{Q^4} \left[ G_E^2(Q^2) - 1 + \frac{1}{3} R_E^2 Q^2 \right], \quad (6.3b)$$

$$= 2\langle r^3 \rangle_E + \frac{24}{\pi^2} \int_{t_0}^{\infty} dt \int_{t_0}^{\infty} dt' \frac{\text{Im} G_E(t) \text{Im} G_E(t')}{(t't)^{3/2}(\sqrt{t'} + \sqrt{t})}. \quad (C.8)$$

□ Zemach radius

$$R_Z \equiv -\frac{4}{\pi} \int_0^{\infty} \frac{dQ}{Q^2} \left[ \frac{G_E(Q^2) G_M(Q^2)}{1 + \kappa} - 1 \right] \quad (6.3c)$$

$$= \langle r \rangle_E + \langle r \rangle_M - \frac{2}{\pi^2} \int_{t_0}^{\infty} \frac{dt}{t} \frac{\text{Im} G_M(t')}{1 + \kappa} \int_{t_0}^{\infty} \frac{dt'}{t'} \frac{\text{Im} G_E(t')}{\sqrt{t'} + \sqrt{t}} \quad (C.9)$$

□ Finite-size effects



a)  $2P - 2S$  Lamb shift:

$$E_{\text{LS}} = -\frac{Z\alpha}{\pi} \int_0^\infty dQ w_{2P-2S}(Q) G_E^2(Q^2) \quad (6.22)$$

$$= -\frac{Z\alpha}{12a^3} [R_E^2 - (2a)^{-1} R_F^3] + O(\alpha^6). \quad (6.1a)$$

b)  $nS$  hyperfine splitting (HFS):

$$E_{\text{HFS}}(nS) = \frac{4Z\alpha}{3\pi mM} \int_0^\infty dQ Q^2 w_{nS}(Q) G_E(Q^2) G_M(Q^2) \quad (6.34b)$$

$$= E_F(nS) [1 - 2a^{-1} R_Z] + O(\alpha^6), \quad (6.1b)$$

with the convolution of momentum-space wave functions:

$$w_{1S}(Q) = \frac{16}{(4 + (aQ)^2)^2}, \quad w_{2S}(Q) = \frac{(1 - (aQ)^2)(1 - 2(aQ)^2)}{(1 + (aQ)^2)^4}, \quad w_{2P-2S}(Q) = \frac{2(aQ)^2(1 - (aQ)^2)}{(1 + (aQ)^2)^4}, \quad (6.16)$$

and the Fermi energy:

$$E_F(nS) = \frac{8Z\alpha}{3a^3} \frac{1 + \kappa}{mM} \frac{1}{n^3}. \quad (6.2)$$

## References

- [1] A. Klein, Phys. Rev. 99 (1955) 998–1008.
- [2] A. M. Baldin, Nucl. Phys. 18 (1960) 310–317.
- [3] C. L. Oxley, V. L. Telegdi, Phys. Rev. 100 (1955) 435–436.
- [4] C. L. Oxley, Phys. Rev. 110 (1958) 733–737.
- [5] G. E. Pugh, R. Gomez, D. H. Frisch, G. S. Janes, Phys. Rev. 105 (1957) 982–995.
- [6] L. G. Hyman, R. Ely, D. H. Frisch, M. A. Wahlig, Phys. Rev. Lett. 3 (1959) 93–96.
- [7] G. Bernardini, A. O. Hanson, A. C. Odian, T. Yamagata, L. B. Auerbach, I. Filosofo, Nuovo Cim. 18 (1960) 1203–1236.
- [8] V. I. Goldansky, et al., Nucl. Phys. 18 (1960) 473 – 491.
- [9] P. Baranov, G. Buinov, V. Godin, V. Kuznetsova, V. Petrunkin, L. Tatarinskaya, V. Shirthenko, L. Shtarkov, V. Yurtchenko, Yu. Yanulis, Phys. Lett. B 52 (1974) 122–124.
- [10] F. J. Federspiel, et al., Phys. Rev. Lett. 67 (1991) 1511–1514.
- [11] E. L. Hallin, et al., Phys. Rev. C 48 (1993) 1497–1507.
- [12] B. E. MacGibbon, et al., Phys. Rev. C 52 (1995) 2097–2109.
- [13] G. Blanpied, et al., Phys. Rev. C 64 (2001) 025203.
- [14] P. Bourgeois, et al., Phys. Rev. C 84 (2011) 035.
- [15] L. S. Myers, et al., Phys. Rev. Lett. 113 (2014) 262506.
- [16] A. Zieger, et al., Phys. Lett. B 278 (1992) 34–38 [Erratum: Phys. Lett. B 281 (1992) 417].
- [17] V. Olmos de León, et al., Eur. Phys. J. A 10 (2001) 207–215.
- [18] G. Galler, et al., Phys. Lett. B 503 (2001) 245.
- [19] S. Wolf, et al., Eur. Phys. J. A 12 (2001) 231.
- [20] M. Camen, et al., Phys. Rev. C 65 (2002) 032202.
- [21] J. Roche, et al., Phys. Rev. Lett. 85 (2000) 708–711.
- [22] P. Janssens, et al., Eur. Phys. J. A 37 (2008) 1–8.
- [23] G. Laveissière, et al., Phys. Rev. Lett. 93 (2004) 122001.
- [24] R. Pohl, et al., Nature 466 (2010) 213–216.
- [25] A. Antognini, F. Nez, K. Schuhmann, F. D. Amaro, F. Biraben, et al., Science 339 (2013) 417–420.
- [26] J. C. Bernauer, R. Pohl, Sci. Am. 310 (2014) 18–25.
- [27] A. Walker-Loud, C. E. Carlson, G. A. Miller, Phys. Rev. Lett. 108 (2012) 232301.
- [28] F. B. Erben, P. E. Shanahan, A. W. Thomas, R. D. Young, Phys. Rev. C 90 (2014) 065205.
- [29] J. Gasser, M. Hoferichter, H. Leutwyler, A. Rusetsky, Eur. Phys. J. C 75 (2015) 375.
- [30] K. Slifer, in: Proceedings, 21st Conference on New Trends in High-Energy Physics (Experiment, Phenomenology, Theory), Yalta, Crimea, Ukraine, September 15–22, 2007 [nucl-ex/0711.4411].
- [31] J. P. Chen, Eur. Phys. J. ST 162 (2008) 103–116.
- [32] J. P. Chen, A. Deur, S. Kuhn, Z. E. Meziani, J. Phys. Conf. Ser. 299 (2011) 012005.

- [33] V. Bernard, E. Epelbaum, H. Krebs, U.-G. Meissner, Phys. Rev. D 87 (2013) 054032.
- [34] V. Lensky, J. M. Alarcón, V. Pascalutsa, Phys. Rev. C 90 (2014) 055202.
- [35] E. Downie, et al., Measurement of the Proton Scalar Polarizabilities, 2012. Proposal to the Mainz Microtron MAMI-A2/06-2012.
- [36] N. Krupina, V. Pascalutsa, Phys. Rev. Lett. 110 (2013) 262001.
- [37] D. Hornidge, Measurement of the Proton Spin Polarizabilities, 2012. Proposal to the Mainz Microtron MAMI-A2/05-2012.
- [38] P. P. Martel, et al., Phys. Rev. Lett. 114 (2015) 112501.
- [39] H. R. Weller, et al., Prog. Part. Nucl. Phys. 62 (2009) 257–303.
- [40] M. Ahmed, HIGS Proposal P-06-10 (2010).
- [41] M. Engelhardt, Phys. Rev. D 76 (2007).
- [42] W. Detmold, B. C. Tiburzi, A. Walker-Loud, Phys. Rev. D 79 (2009) 094505.
- [43] W. Detmold, B. C. Tiburzi, A. Walker-Loud, Phys. Rev. D 81 (2010) 054502.
- [44] T. Primer, W. Kamleh, D. Leinweber, M. Burkardt, Phys. Rev. D 89 (2014) 034508.
- [45] J. M. M. Hall, D. B. Leinweber, R. D. Young, Phys. Rev. D 89 (2014) 054511.
- [46] M. Lujan, A. Alexandru, W. Freeman, F. Lee, Phys. Rev. D 89 (2014) 074506.
- [47] E. Chang, W. Detmold, K. Orginos, A. Parreno, M. J. Savage, B. C. Tiburzi, S. R. Beane, hep-lat/1506.05518 (2015).
- [48] V. Lensky, V. Pascalutsa, Pisma Zh. Eksp. Teor. Fiz. 89 (2009) 127–132. [JETP Lett. 89 (2009) 108].
- [49] V. Lensky, V. Pascalutsa, Eur. Phys. J. C 65 (2010) 195–209.
- [50] V. Lensky, J. A. McGovern, D. R. Phillips, V. Pascalutsa, Phys. Rev. C 86 (2012) 048201.
- [51] J. A. McGovern, D. R. Phillips, H. W. Griesshammer, Eur. Phys. J. A 49 (2013) 12.
- [52] V. Lensky, J. A. McGovern, Phys. Rev. C 89 (2014) 032202.
- [53] A. H. Blin, T. Gutsche, T. Ledwig, V. E. Lyubovitskij, Phys. Rev. D 92 (2015) 096004.
- [54] V. Lensky, J. McGovern, V. Pascalutsa, hep-ph/1510.02794 [to appear in Eur. Phys. J. C] (2015).
- [55] J. M. Alarcón, V. Lensky, V. Pascalutsa, Eur. Phys. J. C 74 (2014) 2852.
- [56] C. Peset, A. Pineda, Nucl. Phys. B 887 (2014) 69–111.
- [57] A. Sibirtsev, P. G. Blunden, Phys. Rev. C 88 (2013) 065202.
- [58] N. L. Hall, A. W. Thomas, R. D. Young, Phys. Rev. D 89 (2014) 117502.
- [59] V. Pascalutsa, M. Vanderhaeghen, Phys. Rev. D 91 (2015) 051503 (R).
- [60] O. Gryniuk, F. Hagelstein, V. Pascalutsa, Phys. Rev. D 92 (2015) 074031.
- [61] D. Drechsel, B. Pasquini, M. Vanderhaeghen, Phys. Rept. 378 (2003) 99–205.
- [62] M. Schumacher, Prog. Part. Nucl. Phys. 55 (2005) 567–646.
- [63] S. E. Kuhn, J.-P. Chen, E. Leader, Prog. Part. Nucl. Phys. 63 (2009) 1–50.
- [64] D. R. Phillips, J. Phys. G 36 (2009) 104004.
- [65] H. Griesshammer, J. McGovern, D. Phillips, G. Feldman, Prog. Part. Nucl. Phys. 67 (2012) 841–897.

- [66] P. A. M. Guichon, M. Vanderhaeghen, *Prog. Part. Nucl. Phys.* 41 (1998) 125–190.
- [67] B. R. Holstein, S. Scherer, *Ann. Rev. Nucl. Part. Sci.* 64 (2014) 51–81.
- [68] R. Pohl, R. Gilman, G. A. Miller, K. Pachucki, *Ann. Rev. Nucl. Part. Sci.* 63 (2013) 175–204.
- [69] C. E. Carlson, *Prog. Part. Nucl. Phys.* 82 (2015) 59–77.
- [70] S. G. Karshenboim, E. Y. Korzinin, V. A. Shelyuto, V. G. Ivanov, *Journal of Physical and Chemical Reference Data* 44 (2015) 031202.
- [71] K. A. Olive, et al., *Chin. Phys. C* 38 (2014) 090001.
- [72] S. Capstick, B. D. Keister, *Phys. Rev. D* 46 (1992) 84.
- [73] S. Capstick, B. D. Keister, *Phys. Rev. D* 47 (1993) 860–866.
- [74] P. C. Hecking, G. F. Bertsch, *Phys. Lett. B* 99 (1981) 237.
- [75] A. Schafer, R. Muller, D. Vasak, W. Greiner, *Phys. Lett. B* 143 (1984) 323–325.
- [76] R. Weiner, W. Weise, *Phys. Lett. B* 159 (1985) 85.
- [77] N. N. Scoccola, W. Weise, *Nucl. Phys. A* 517 (1990) 495–508.
- [78] M. Chemtob, *Nucl. Phys. A* 473 (1987) 613.
- [79] B. Golli, R. Sraka, *Phys. Lett. B* 312 (1993) 24–29.
- [80] B. Schwesinger, *Phys. Lett. B* 298 (1993) 17–21.
- [81] W. Broniowski, T. D. Cohen, *Phys. Rev. D* 47 (1993) 299–312.
- [82] W. Broniowski, M. K. Banerjee, T. D. Cohen, *Phys. Lett. B* 283 (1992) 22–26.
- [83] E. N. Nikolov, W. Broniowski, K. Goeke, *Nucl. Phys. A* 579 (1994) 398–412.
- [84] A. C. Hearn, E. Leader, *Phys. Rev.* 126 (1962) 789–805.
- [85] A. I. L'vov, V. A. Petrun'kin, M. Schumacher, *Phys. Rev. C* 55 (1997) 359–377.
- [86] D. Drechsel, M. Gorchtein, B. Pasquini, M. Vanderhaeghen, *Phys. Rev. C* 61 (2000) 015204.
- [87] B. Pasquini, D. Drechsel, M. Vanderhaeghen, *Phys. Rev. C* 76 (2007) 015203.
- [88] S. Kondratyuk, O. Scholten, *Nucl. Phys. A* 677 (2000) 396–422.
- [89] S. Kondratyuk, O. Scholten, *Phys. Rev. C* 64 (2001) 024005.
- [90] A. Gasparyan, M. F. M. Lutz, *Nucl. Phys. A* 848 (2010) 126–182.
- [91] A. M. Gasparyan, M. F. M. Lutz, B. Pasquini, *Nucl. Phys.* (2011) 79–92.
- [92] V. Pascalutsa, O. Scholten, *Nucl. Phys. A* 591 (1995) 658–674.
- [93] T. Feuster, U. Mosel, *Phys. Rev. C* 59 (1999) 460–491.
- [94] Y. Zhang, K. Savvidy, *Phys. Rev. C* 88 (2013) 064614.
- [95] G. Eichmann, C. S. Fischer, *Phys. Rev. D* 87 (2013) 036006.
- [96] D. Babusci, G. Giordano, A. I. L'vov, G. Matone, A. M. Nathan, *Phys. Rev. C* 58 (1998) 1013–1041.
- [97] B. R. Holstein, D. Drechsel, B. Pasquini, M. Vanderhaeghen, *Phys. Rev. C* 61 (2000) 034316.
- [98] S. Ragusa, *Phys. Rev. D* 47 (1993) 3757–3767.
- [99] C. W. Bernard, T. Draper, K. Olynyk, M. Rushton, *Phys. Rev. Lett.* 49 (1982) 1076.

- [100] H. R. Fiebig, W. Wilcox, R. M. Woloshyn, Nucl. Phys. B 324 (1989) 47.
- [101] C. Aubin, K. Orginos, V. Pascalutsa, M. Vanderhaeghen, Phys. Rev. D 79 (2009) 051502.
- [102] A. Alexandru, F. X. Lee, PoS LATTICE2008 (2008) 145 [hep-lat/0810.2833].
- [103] W. Detmold, B. C. Tiburzi, A. Walker-Loud, Phys. Rev. D 73 (2006) 114505.
- [104] W. Freeman, A. Alexandru, M. Lujan, F. X. Lee, Phys. Rev. D 90 (2014) 054507.
- [105] M. Lujan, A. Alexandru, W. Freeman, F. Lee, PoS LATTICE2014 (2014) 153 [hep-lat/1411.0047].
- [106] S. Aoki, et al., Phys. Rev. D 79 (2009) 034503.
- [107] J. Green, O. Gryniuk, G. von Hippel, H. B. Meyer, V. Pascalutsa, Phys. Rev. Lett. 115 (2015) 222003.
- [108] S. Weinberg, Physica A 96 (1979) 327.
- [109] J. Gasser, H. Leutwyler, Ann. Phys. 158 (1984) 142.
- [110] J. Gasser, M. E. Sainio, A. Svarc, Nucl. Phys. B 307 (1988) 779.
- [111] H. Georgi, Ann. Rev. Nucl. Part. Sci. 43 (1993) 209–252.
- [112] E. E. Jenkins, A. V. Manohar, Phys. Lett. B 255 (1991) 558–562.
- [113] M. N. Butler, M. J. Savage, Phys. Lett. B 294 (1992) 369–374.
- [114] V. Bernard, N. Kaiser, U.-G. Meissner, Int. J. Mod. Phys. E (1995) 193–346.
- [115] V. Bernard, N. Kaiser, U. G. Meissner, Phys. Rev. Lett. 67 (1991) 1515–1518.
- [116] V. Bernard, N. Kaiser, U. G. Meissner, Nucl. Phys. B (1992) 346–370.
- [117] T. R. Hemmert, B. R. Holstein, J. Kambor, Phys. Rev. D 55 (1997) 5598–5612.
- [118] R. P. Hildebrandt, H. W. Griesshammer, T. R. Hemmert, B. Pasquini, Eur. Phys. J. A 20 (2004) 293–315.
- [119] J. M. Hall, V. Pascalutsa, Eur. Phys. J. C 72 (2012) 2206.
- [120] L. Geng, Front. Phys. China 8 (2013) 328–348.
- [121] V. Pascalutsa, M. Vanderhaeghen, S. N. Yang, Phys. Rept. 437 (2007) 125–232.
- [122] T. R. Hemmert, B. R. Holstein, J. Kambor, Phys. Lett. B 395 (1997) 89–95.
- [123] V. Pascalutsa, D. R. Phillips, Phys. Rev. C 67 (2003) 055202.
- [124] J. M. Alarcón, F. Hagelstein, V. Lensky, V. Pascalutsa (in preparation).
- [125] J. M. Alarcón, J. Martin Camalich, J. A. Oller, Phys. Rev. D 85 (2012) 051503.
- [126] A. N. Hiller Blin, T. Ledwig, M. J. Vicente Vacas, Phys. Lett. B 747 (2015) 217–222.
- [127] V. Pascalutsa, M. Vanderhaeghen, Phys. Rev. Lett. 95 (2005) 232001.
- [128] V. Pascalutsa, M. Vanderhaeghen, Phys. Rev. D 73 (2006) 034003.
- [129] V. Pascalutsa, M. Vanderhaeghen, Phys. Rev. Lett. 94 (2005) 102003.
- [130] V. Pascalutsa, M. Vanderhaeghen, Phys. Rev. D 77 (2008) 014027.
- [131] R. Tarrach, Nuovo Cim. A 28 (1975) 409.
- [132] W.-y. Tsai, L. L. DeRaad, K. A. Milton, Phys. Rev. D 6 (1972) 1428–1438.
- [133] A. Klein, Y. Nishina, Z. Phys. 52 (1929) 853.

- [134] V. I. Ritus, Sov. Phys. JETP 5 (1957) 1249.
- [135] W. Pfeil, H. Rollnik, S. Stankowski, Nucl. Phys. B 73 (1974) 166–188.
- [136] W. Thirring, The London, Edinburgh, and Dublin Philosophical Magazine and Journal of Science 41 (1950) 1193–1194.
- [137] F. E. Low, Phys. Rev. 96 (1954) 1428–1432.
- [138] M. Gell-Mann, M. L. Goldberger, Phys. Rev. 96 (1954) 1433–1438.
- [139] K. M. Watson, Phys. Rev. 95 (1954) 228–236.
- [140] I. Guiasu, E. Radescu, Annals Phys. 120 (1979) 145.
- [141] A. Aleksejevs, S. Barkanova, J. Phys. G 38 (2011) 035004.
- [142] A. Aleksejevs, S. Barkanova, Nucl. Phys. Proc. Suppl. 245 (2013) 17–24.
- [143] R. Worden, Nucl. Phys. B 37 (1972) 253 – 312.
- [144] L. Maximon, Phys. Rev. C 39 (1989) 347–351.
- [145] N. Krupina, in: Proceedings, 52nd International Winter Meeting on Nuclear Physics, Bormio, Italy, January 27–31, 2014 [nucl-th/1405.1294].
- [146] S. R. Beane, M. Malheiro, J. A. McGovern, D. R. Phillips, U. van Kolck, Phys. Lett. B (2003) 200–206.
- [147] S. R. Beane, M. Malheiro, J. A. McGovern, D. R. Phillips, U. van Kolck, Nucl. Phys. A (2005) 311–361.
- [148] A. I. L’vov, Int. J. Mod. Phys. A (1993) 5267–5303.
- [149] B. Pasquini, M. Gorchtein, D. Drechsel, A. Metz, M. Vanderhaeghen, Eur. Phys. J. A 11 (2001) 185–208.
- [150] D. Shukla, A. Nogga, D. R. Phillips, Nucl. Phys. A 819 (2009) 98–134.
- [151] J. Beringer, et al., Phys. Rev. D 86 (2012) 010001.
- [152] J. McGeorge, J. Kellie, et al., Eur. Phys. J. A 37 (2008) 129–137.
- [153] K.-H. Kaiser, et al., Nucl. Instrum. Methods Phys. Res., Sect. A 593 (2008) 159–170.
- [154] D. Lohmann, et al., NIM A 343 (1994) 494–507.
- [155] A. Starostin, et al., Phys. Rev. C 64 (2001) 055205.
- [156] R. Novotny, IEEE Trans. Nucl. Sci. 38 (1991) 379–385.
- [157] C. M. Tarbert, et al., Phys. Rev. Lett. 100 (2008) 132301.
- [158] L. S. Myers, et al., Phys. Rev. C 86 (2012) 044614.
- [159] J. Annand, Proposal to the Mainz Microtron MAMI-A2 (2013).
- [160] V. Pascalutsa, D. R. Phillips, Phys. Rev. C 68 (2003) 055205.
- [161] C. Collicott, Ph.D. thesis, Dalhousie University, Halifax, NS, 2015.
- [162] R. Miskimen, Measuring the Spin Polarizabilities of the Proton in Double-Polarized Real Compton Scattering, 2009. Proposal to the High Intensity Gamma-Ray Source PAC-09.
- [163] A. Thomas, Eur. Phys. J. Special Topics 198 (2011) 171–180.
- [164] D. G. Crabb, W. Meyer, Annu. Rev. Nucl. Part. Sci. 47 (1997) 67–109.
- [165] POCOfoam, registered trademark of Poco Graphite, Inc., 2015.
- [166] T. R. Hemmert, B. R. Holstein, J. Kambor, G. Knöchlein, Phys. Rev. D 57 (1998) 5746–5754.



- [167] K. B. Vijaya Kumar, J. A. McGovern, M. C. Birse, Phys. Lett. B 479 (2000) 167–172.
- [168] G. C. Gellas, T. R. Hemmert, U.-G. Meißner, Phys. Rev. Lett. 85 (2001) 14.
- [169] B. Pasquini, P. Pedroni, D. Drechsel, Phys. Lett. B 687 (2010) 160–166.
- [170] P. A. M. Guichon, G. Q. Liu, A. W. Thomas, Nucl. Phys. A 591 (1995) 606–638.
- [171] M. Gorchtein, A. P. Szczepaniak, Phys. Rev. Lett. 101 (2008) 141601.
- [172] M. Gorchtein, Phys. Rev. C 81 (2010) 015206.
- [173] T. R. Hemmert, B. R. Holstein, G. Knochlein, S. Scherer, Phys. Rev. Lett. 79 (1997) 22–25.
- [174] T. R. Hemmert, B. R. Holstein, G. Knochlein, D. Drechsel, Phys. Rev. D 62 (2000) 014013.
- [175] D. Drechsel, O. Hanstein, S. S. Kamalov, L. Tiator, Nucl. Phys. A 645 (1999) 145–174.
- [176] H. Fonvieille, et al., Phys. Rev. C 86 (2012) 015210.
- [177] T. R. Hemmert, B. R. Holstein, G. Knochlein, S. Scherer, Phys. Rev. D 55 (1997) 2630–2643.
- [178] M. Gorchtein, C. Lorce, B. Pasquini, M. Vanderhaeghen, Phys. Rev. Lett. 104 (2010) 112001.
- [179] H. Fonvieille, private communication, 2015.
- [180] H. Alvensleben, U. Becker, P. Biggs, W. Busza, M. Chen, et al., Phys. Rev. Lett. 30 (1973) 328–332.
- [181] V. Pauk, M. Vanderhaeghen, Phys. Rev. Lett. 115 (2015) 221804.
- [182] J. Motz, H. Olsen, H. Koch, Rev. Mod. Phys. 41 (1969) 581–639.
- [183] M. Gell-Mann, M. Goldberger, W. E. Thirring, Phys. Rev. 95 (1954) 1612–1627.
- [184] H. Burkhardt, W. N. Cottingham, Annals Phys. 56 (1970) 453–463.
- [185] S. Gerasimov, Sov. J. Nucl. Phys. 2 (1966) 430–433.
- [186] S. Drell, A. C. Hearn, Phys. Rev. Lett. 16 (1966) 908–911.
- [187] M. Hosoda, K. Yamamoto, Progress of Theoretical Physics 36 (1966) 425–426.
- [188] S. Weinberg, Lectures on Elementary Particles and Quantum Field Theory, volume 1 of *Brandeis University Summer Institute 1970*, MIT Press, Cambridge, MA, 1970.
- [189] G. Altarelli, N. Cabibbo, L. Maiani, Phys. Lett. B 40 (1972) 415.
- [190] D. A. Dicus, R. Vega, Phys. Lett. B 501 (2001) 44–47.
- [191] V. Pascalutsa, B. R. Holstein, M. Vanderhaeghen, Phys. Lett. B 600 (2004) 239–247.
- [192] B. R. Holstein, V. Pascalutsa, M. Vanderhaeghen, Phys. Rev. D 72 (2005) 094014.
- [193] J. Sucher, Phys. Rev. D 6 (1972) 1798–1800.
- [194] J. Bernabeu, R. Tarrach, Phys. Lett. B 55 (1975) 183.
- [195] A. I. L'vov, Nucl. Phys. A 638 (1998) 756–764.
- [196] Y. Liang, M. Christy, R. Ent, C. Keppel, Phys. Rev. C 73 (2006) 065201.
- [197] D. Drechsel, G. Knochlein, A. Y. Korchin, A. Metz, S. Scherer, Phys. Rev. C 58 (1998) 1751–1757.
- [198] S. Wandzura, F. Wilczek, Phys. Lett. B 72 (1977) 195.
- [199] B. W. Filippone, X.-D. Ji, Adv. Nucl. Phys. 26 (2001) 1.
- [200] M. Damashek, F. J. Gilman, Phys. Rev. D 1 (1970) 1319–1332.

- [201] T. Armstrong, W. Hogg, G. Lewis, A. Robertson, G. Brookes, et al., Phys. Rev. D 5 (1972) 1640–1652.
- [202] O. Gryniuk, F. Hagelstein, N. Krupina, V. Pascalutsa (in preparation).
- [203] M. J. Creutz, S. Drell, E. A. Paschos, Phys. Rev. 178 (1969) 2300–2301.
- [204] S. J. Brodsky, F. E. Close, J. Gunion, Phys. Rev. D 5 (1972) 1384.
- [205] M. Gorchtein, T. Hobbs, J. T. Londergan, A. P. Szczepaniak, Phys. Rev. C 84 (2011) 065202.
- [206] U. Schröder, Nucl. Phys. B 166 (1980) 103.
- [207] D. Babusci, G. Giordano, G. Matone, Phys. Rev. C 57 (1998) 291–294.
- [208] M. I. Levchuk, A. I. L'vov, Nucl. Phys. A 674 (2000) 449–492.
- [209] D. Drechsel, S. Kamalov, L. Tiator, Eur. Phys. J. A (2007) 69–97 (MAID program: <http://www.kph.uni-mainz.de/MAID/>).
- [210] R. L. Workman, M. W. Paris, W. J. Briscoe, I. I. Strakovsky, Phys. Rev. C (2012) 015202 (SAID program: <http://gwdac.phys.gwu.edu>).
- [211] J. Ahrens, et al., Phys. Rev. Lett. 87 (2001) 022003.
- [212] L. Tiator, in: Proceedings, 2nd International Symposium on the Gerasimov-Drell-Hearn Sum Rule and the Spin Structure of the Nucleon (GDH 2002) pp. 27–36.
- [213] H. Dutz, et al., Phys. Rev. Lett. 91 (2003) 192001.
- [214] K. Helbing, Prog. Part. Nucl. Phys. 57 (2006) 405–469.
- [215] M. Schumacher, M. Levchuk, Nucl. Phys. A 858 (2011) 48–66.
- [216] J. Ahrens, et al., Phys. Rev. Lett. 84 (2000) 5950–5954.
- [217] H. Dutz, K. Helbing, J. Krimmer, T. Speckner, G. Zeitler, et al., Phys. Rev. Lett. 93 (2004) 032003.
- [218] N. Bianchi, E. Thomas, Phys. Lett. B 450 (1999) 439–447.
- [219] S. Simula, M. Osipenko, G. Ricco, M. Taiuti, Phys. Rev. D 65 (2002) 034017.
- [220] H. Arenhovel, in: Proceedings, Gerasimov-Drell-Hearn Sum Rule and the Nucleon Spin Structure in the Resonance Region (GDH 2000), Mainz, Germany, June 14–17 [nucl-th/0006083].
- [221] G. Laskaris, Q. Ye, B. Lalremruata, Q. Ye, M. Ahmed, et al., Phys. Rev. Lett. 110 (2013) 202501.
- [222] S. Costanza, J. Phys. Conf. Ser. 349 (2012) 012011.
- [223] P. J. Mohr, B. N. Taylor, D. B. Newell, Rev. Mod. Phys. 84 (2012) 1527–1605.
- [224] M. I. Eides, H. Grotch, V. A. Shelyuto, Phys. Rept. 342 (2001) 63–261.
- [225] A. Antognini, F. Kottmann, F. Biraben, P. Indelicato, F. Nez, et al., Annals Phys. 331 (2013) 127–145.
- [226] A. Martynenko, Phys. Atom. Nucl. 71 (2008) 125–135.
- [227] K. Pachucki, Phys. Rev. A 53 (1996) 2092–2100.
- [228] E. Borie, Annals Phys. 327 (2012) 733–763.
- [229] A. Martynenko, Phys. Rev. A 71 (2005) 022506.
- [230] R. Faustov, E. Cherednikova, A. Martynenko, Nucl. Phys. A 703 (2002) 365–377.
- [231] S. G. Karshenboim, Phys. Rev. D 90 (2014) 053012.
- [232] S. G. Karshenboim, Phys. Rev. D 90 (2014) 053013.

- [233] J. L. Friar, *Annals Phys.* 122 (1979) 151.
- [234] F. Hagelstein, V. Pascalutsa, *Phys. Rev. A* 91 (2015) 040502 (R).
- [235] J. Schwinger, *Phys. Rev.* 75 (1949) 651–679.
- [236] S. G. Karshenboim, V. G. Ivanov, E. Yu. Korzinin, *Phys. Rev. A* 85 (2012) 032509.
- [237] H. A. Bethe, E. E. Salpeter, *Quantum Mechanics of One- and Two-Electron Atoms*, Springer-Verlag, 1957.
- [238] A. De Rujula, *Phys. Lett. B* 693 (2010) 555–558.
- [239] I. Sick, *Few Body Syst.* 50 (2011) 367–369.
- [240] I. Sick, *Prog. Part. Nucl. Phys.* 67 (2012) 473–478.
- [241] I. Sick, D. Trautmann, *Phys. Rev. C* 89 (2014) 012201.
- [242] I. Sick, *Few Body Syst.* 55 (2014) 903–906.
- [243] C. K. Iddings, *Phys. Rev.* 138 (1965) B446–B458.
- [244] S. Drell, J. D. Sullivan, *Phys. Rev.* 154 (1967) 1477–1498.
- [245] V. Pascalutsa, J. A. Tjon, *Phys. Rev. C* 60 (1999) 034005.
- [246] K. Pachucki, *Phys. Rev. A* 60 (1999) 3593–3598.
- [247] A. Martynenko, *Phys. Atom. Nucl.* 69 (2006) 1309–1316.
- [248] C. E. Carlson, M. Vanderhaeghen, *Phys. Rev. A* 84 (2011) 020102.
- [249] M. C. Birse, J. A. McGovern, *Eur. Phys. J. A* 48 (2012) 120.
- [250] J. Bernabeu, T. E. O. Ericson, *Z. Phys. A* 309 (1983) 213.
- [251] J. Bernabeu, C. Jarlskog, *Nucl. Phys. B* 75 (1974) 59.
- [252] A. Veitia, K. Pachucki, *Phys. Rev. A* 69 (2004) 042501.
- [253] M. Gorchtein, F. J. Llanes-Estrada, A. P. Szczepaniak, *Phys. Rev. A* 87 (2013) 052501.
- [254] R. J. Hill, G. Paz, *Phys. Rev. Lett.* 107 (2011) 160402.
- [255] P. J. Mohr, J. Griffith, J. Sapirstein, *Phys. Rev. A* 87 (2013) 052511.
- [256] J. Tonnison, A. Sandorfi, S. Hoblit, A. Nathan, *Phys. Rev. Lett.* 80 (1998) 4382–4385.
- [257] S. Eidelman, et al., *Phys. Lett. B* 592 (2004) 1–1109.
- [258] F. Brasse, W. Flauger, J. Gayler, S. Goel, R. Haidan, et al., *Nucl. Phys. B* 110 (1976) 413.
- [259] H. Abramowicz, A. Levy, *hep-ph/9712415* (1997).
- [260] M. E. Christy, P. E. Bosted, *Phys. Rev. C* 81 (2010) 055213.
- [261] A. Capella, A. Kaidalov, C. Merino, J. Tran Thanh Van, *Phys. Lett. B* 337 (1994) 358–366.
- [262] M. Gorchtein, C. Horowitz, M. J. Ramsey-Musolf, *Phys. Rev. C* 84 (2011) 015502.
- [263] G. Simon, C. Schmitt, F. Borkowski, V. Walther, *Nucl. Phys. A* 333 (1980) 381–391.
- [264] J. J. Kelly, *Phys. Rev. C* 70 (2004) 068202.
- [265] J. Arrington, W. Melnitchouk, J. A. Tjon, *Phys. Rev. C* 76 (2007) 035205.
- [266] J. C. Bernauer, et al., *Phys. Rev. Lett.* 105 (2010) 242001.

- [267] M. Vanderhaeghen, T. Walcher, Nucl. Phys. News 21 (2011) 14–22.
- [268] C. E. Carlson, M. Vanderhaeghen, Ann. Rev. Nucl. Part. Sci. 57 (2007) 171–204.
- [269] C. E. Carlson, V. Nazaryan, K. Griffioen, Phys. Rev. A 83 (2011) 042509.
- [270] H. D. Abarbanel, S. Nussinov, Phys. Rev. 158 (1967) 1462–1466.
- [271] C. E. Carlson, in: Proceedings, Precision Physics of Simple Atomic Systems, Venice, Italy, June 12–17, 2006 [hep-ph/0611206].
- [272] C. E. Carlson, Can. J. Phys. 85 (2007) 429–439.
- [273] A. C. Zemach, Phys. Rev. 104 (1956) 1771–1781.
- [274] G. T. Bodwin, D. Yennie, Phys. Rev. D 37 (1988) 498.
- [275] C. E. Carlson, V. Nazaryan, K. Griffioen, Phys. Rev. A 78 (2008) 022517.
- [276] R. Faustov, I. Gorbacheva, A. Martynenko, Proc. SPIE Int. Soc. Opt. Eng. 6165 (2006) 0M.
- [277] S. G. Karshenboim, Phys. Lett. A 225 (1997) 97.
- [278] E. De Rafael, Phys. Lett. B 37 (1971) 201–203.
- [279] P. Gnädig, J. Kuti, Phys. Lett. B 42 (1972) 241–245.
- [280] R. Faustov, A. Martynenko, Phys. Atom. Nucl. 65 (2002) 265–270.
- [281] R. Faustov, A. Martynenko, Eur. Phys. J. C 24 (2002) 281–285.
- [282] V. Nazaryan, C. E. Carlson, K. A. Griffioen, Phys. Rev. Lett. 96 (2006) 163001.
- [283] A. Camsonne, et al., A Measurement of  $g_2^p$  and the Longitudinal-Transverse Spin Polarizability. E08-027 Proposal, <http://hallaweb.jlab.org/experiment/g2p/docs/PAC33/dlt.pdf>.
- [284] K. Dharmawardane, et al., Phys. Lett. B 641 (2006) 11–17.
- [285] D. Nevado, A. Pineda, Phys. Rev. C 77 (2008) 035202.
- [286] C. Peset, A. Pineda, Eur. Phys. J. A 51 (2015) 32.
- [287] F. Hagelstein, V. Pascalutsa, in: Proceedings, 8th International Workshop on Chiral Dynamics (CD 2015), Pisa, Italy, June 29 – July 3 [nucl-th/1511.04301].
- [288] H.-Q. Zhou, H.-R. Pang, Phys. Rev. A 92 (2015) 032512.
- [289] N. T. Huong, E. Kou, B. Moussallam, hep-ph/1511.06255 (2015).
- [290] S. Drell, Il Nuovo Cimento 11 (1959) 693–697.
- [291] K. Kossert, et al., Phys. Rev. Lett. 88 (2002) 162301.
- [292] K. Kossert, et al., Eur. Phys. J. A 16 (2003) 259–273.
- [293] H. Krebs, Talk at EINN15 Workshop, Paphos, Cyprus, November 1–7, 2015.
- [294] J. C. Bernauer, M. O. Distler, J. Friedrich, T. Walcher, Phys. Rev. C 90 (2014) 015206.
- [295] I. Lorenz, U.-G. Meißner, H.-W. Hammer, Y.-B. Dong, Phys. Rev. D 91 (2015) 014023.
- [296] D. Borisyuk, A. Kobushkin, Phys. Rev. C 75 (2007) 038202.
- [297] J. Arrington, P. Blunden, W. Melnitchouk, Prog. Part. Nucl. Phys. 66 (2011) 782–833.
- [298] P. G. Blunden, W. Melnitchouk, J. A. Tjon, Phys. Rev. C 72 (2005) 034612.
- [299] S. Dubnicka, A. Z. Dubnikova, P. Weisenpacher, J. Phys. G: Nucl. Part. Phys. 29 (2003) 405.

- [300] C. Adamuscin, S. Dubnicka, A. Z. Dubnickova, P. Weisenpacher, *Prog. Part. Nucl. Phys.* 55 (2005) 228–241.
- [301] A. Antognini, et al., in: *Proceedings, 21st International Conference on Few-Body Problems in Physics (FB21)*, 2015 [atom-ph/1509.03235].
- [302] U. Jentschura, *Annals Phys.* 326 (2011) 500–515.
- [303] A. Antognini, in: *Proceedings, 22nd International Conference on Laser Spectroscopy (ICOLS 2015)*, Singapore, June 28 – July 3 [atom-ph/1512.01765].